eman ta zabal zazu

Universidad del País Vasco
Euskal Herriko Unibertsitatea

Electronic and transport properties of 2D Dirac materials: graphene and topological insulators

Doctoral thesis

by Bernhard Kretz

Thesis supervisor:

Aran Garcia-Lekue

2018

This thesis has been carried out at DIPC

Acknowledgements

First of all, I would like to thank my supervisor Aran Garcia-Lekue for her support and guidance during all these years. She always took her time to help me with my problems and to discuss results and new ideas. I want to thank Aran especially for all the help with the paperwork and bureaucracy involved in doing a PhD.

I would like to thank my parents, Klaudia and Richard, for accepting and supporting my decision to do a PhD so far from home.

I would like to thank Mads Brandbyge from DTU for letting me stay and work in his group for a total fo three months during my thesis. Further, I would like to thank him and his pots-docs and students, Nick Papior, Daniele Stradi and Christian S. Pedersen, for the good collaboration, making my stays in Denmark a scientifically valuable experience.

I would like to thank all our experimental collaborators, especially M. Carmen Martínez-Velarte and David Serrate from the University of Zaragoza, and César Moreno and Aitor Mugarza from the Catalan Institute of Nanoscience and Nanotechnology.

I would like to thank all my colleagues, friends and all the great people I met here in Donostia. I hope they forgive me for not naming all of them explicitly, but that would take me another four years.

I would like to thank DIPC for financial support, and the DIPC computing center for providing and maintaining the computational infrastructure and for the technical support.

Abstract

This thesis presents a set of contributions to the field of 2D Dirac materials, which have emerged as promising candidates for future nanoelectronics. The electronic and transport properties of various graphene-based nanostructures and surfaces of topological insulators reported in this work, provide further insight into the functionalities of this class of materials. For the characterization of the materials reported in this thesis, we applied density functional theory and a non-equilibrium Green's function approach.

Most graphene-based electronic devices, require the formation of contacts between the 2D material and metal electrodes. Within this context, it is crucial to design graphene-metal interfaces with low contact resistances. In this work, we analyzed the structural evolution and transport properties of various metal-graphene contacts with and without functionalization or contamination of the graphene edge, with special focus on their influence on the contact resistance. For metal-graphene edge contacts, we found a strong metal dependence of the stability on graphene edge contaminants. In general, we found the contact resistance to increase upon graphene edge contamination, although the strength of the relative increment dependent significantly on the metal and edge contamination. Nevertheless, our study provides valuable insight into the mechanisms responsible for device-to-device variations of metal-graphene contacts in experiments.

Further, we studied the electronic and transport properties of a novel type of grahene nanoribbon (GNR) and the nanoporous graphene (NPG) derived from it. Our characterization of the electronic properties of the NPG revealed that, like the ribbon, it is a semiconductor. Furthermore, it inherits uniquely localized states from ribbon, which form a 1D band dispersing in the direction perpendicular to the ribbon's backbone. Moreover, we found states localized in the vacuum region

of the ribbon. Within the NPG, these states interact with each other, forming bonding and anti-bonding pore states. scanning tunneling microsopy (STM) experiments have confirmed the existence of these pore states and demonstrated the uniform growth of the NPG over a larger area. Due to its semiconducting behavior, this NPG offers high potential for many electronic applications (e.g., field-effect transistors (FETs)), as well as for molecular sensing and sieving applications.

Due to their extraordinary properties, topological insulator (TI) have been proposed for a wide range of applications, especially for spintronics. With the aim of spintronic applications, the challenge in this field is to find a TI with a surface state protected against magnetic perturbations. Within this context, we investigate the influence of chemical disorder on the structural and magnetic properties of a Co adsorbed on the surface of a given ternary TI surface. In combination with experiments, we could demonstrate that Co tends to adsorbed away from the high-symmetry position whenever it is surrounded by different species of the TI's surface atoms. This adsorption behavior leads to a reduced hybridization between Co and the TI's surface state and, consequently, the surface state is still protected by time-reversal symmetry. Similar results can be expected for other ternary TI's with chemical disorder in the surface layer.

Contents

List of publications

- *"Atomistic insight into the formation of metal-graphene 1D contacts"*
  B. Kretz, C. S. Pedersen, D. Stradi, M. Brandbyge, and A. Garcia-Lekue.
  under review (2018).

- *"Bottom-up synthesis of multifunctional nanoporous graphene"*
  C. Moreno, M. Vilas-Varela*, B. Kretz*, A. Garcia-Lekue, M. V. Costache, M. Paradinas, M. Panighel, G. Ceballos, S. O. Valenzuela, D. Peña, and A. Mugarza.
  Science, **360**, 199-203 (2018).
  (*these authors contributed equally to this work)

- *"Chemical Disorder in Topological Insulators: A Route to Magnetism Tolerant Topological Surface States"*
  M. C. Martínez-Velarte, B. Kretz, M. Moro-Lagares, M. H. Aguirre, T. M. Riedemann, T. A. Lograsso, L. Morellón, M. R. Ibarra, A. Garcia-Lekue, D. Serrate.
  Nano Lett., **17**, 4047 (2017).

Contributions by others

Nowadays, scientific research is almost always a collaborative effort. Of course, the same holds for research carried out and presented in the framework of this thesis.

Nick Papior from Mads Brandbyge's group at the Technical University of Denmark (DTU) provided some of the code for our implementation of a tool to analyze transmission eigenchannels presented in chapter 3.

For our extensive study of metal-graphene edge contacts in chapter 4, Christian S. Pedersen (also from Mads Brandbyge's group at DTU) provided the calculations for Ti and Au electrodes.

To the work about graphene nanoribbons and nanoporous graphene presented in chapter 5 the following contributions have been made: Manuel Vilas-Varela and Diego Peña (University of Santiago de Compostela) synthesized the monomer precursor. César Moreno, Mirko Panighel, Gustavo Ceballos, and Aitor Mugarza (Catalan Institute of Nanoscience and Nanotechnology, CIN2) performed and analyzed the STM measurements. Marius V. Costache and Sergio O. Valenzuela (CIN2) fabricated the devices and carried out the transport measurements.

Contributions to the research about the topological insulators presented in chapter 6 have been made by the following people: M. Carmen Martínez-Velarte, María Moro-Lagares and David Serrate (University of Zaragoza) have carried out and analyzed the STM measurements. Myriam H. Aguirre (University of Zaragoza) performed the STEM experiments. Trevor M. Riedemann and Thomas A. Lograsso (Ames Laboratory, USA) grew grew the single crystals.

Acronyms

1D	one-dimensional
2D	two-dimensional
3D	three-dimensional
AC	armchair
AGNR	armchair graphene nanoribbon
BTD	block-tri-diagonal
CB	conduction band
DFT	density functional theory
DOS	density of states
DZ	double-ζ
DZP	double-ζ-polarized
FET	field-effect transistor
GGA	generalized gradient approximation
GNR	grahene nanoribbon
IPS	image potential state
LCAO	linear combination of atomic orbitals

LDA local density approximation

LDOS local density of states

MM meta-meta

NEGF non-equilibrium Green's function

NFE nearly-free electrons

NPG nanoporous graphene

PAW projector augmented wave

PBE Perdew-Burke-Ernzerhof

PDOS projected density of states

PM para-meta

PP para-para

QL quintuple layer

QPI quasi-particle interference

QSHE quantum spin Hall effect

SAMO superatom molecular orbital

SFE spin-filtering efficiency

SIESTA Spanish Initiative for Electronic Simulations with Thousands of Atoms

SOC spin-orbit coupling

STEM scanning transmission electron microscopy

STM scanning tunneling microsopy

STS scanning tunneling spectroscopy

TI topological insulator

TRS time-reversal symmetry

TSS topological surface state

VASP Vienna Ab-inition Simulation Package

VB valence band

VBM valence band maximum

vdW van der Waals

ZZ zig-zag

Chapter 1

Introduction

The invention of the silicon based integrated circuit in the late 1950s started a revolution in electronics. Since then, thanks to ever more advanced production methods, integrated circuits have been miniaturized to a size where single transistors only measure a few nanometers. This miniaturization of devices allowed an increase in packing density, and, consequently, the performance of electronic devices grew exponentially, as predicted by Moore's law. However, physical effects at the nano-scale, like quantum tunneling, lead to increased leakage and off currents, thus restricting the potential for further miniaturization.

The limit of miniaturization of silicon based devices will most likely be reached within the next decade and, therefore, the search for alternative materials for high-performance electronics has gained a lot of momentum in recent years. A lot of research in this direction has been inspired by the discovery and development of novel materials belonging to the, equally novel, class of two-dimensional Dirac materials. These materials, with their most prominent representatives being graphene and topological insulators, posses some very unique and extraordinary properties making them ideal candidates for future application in electronics and related fields[1, 2].

The main characteristic of Dirac materials is the linear dispersion relation of the band structure around Fermi-level. As a result, the electrons in these bands behave like massless fermions which can be described by the Weyl equation, i.e., a version of the Dirac equation for massless spin-1/2 particles[2], or by a simplified

Dirac Hamiltonian[1],

$$H_D = v_F \boldsymbol{\sigma} \cdot \mathbf{p} + m v_F^2 \sigma_z, \tag{1.1}$$

where $\boldsymbol{\sigma} = (\sigma_x, \sigma_y)$ and σ_z are the Pauli matrices, and v_F, $\mathbf{p}$ and m are the Dirac fermion's Fermi velocity, momentum and mass, respectively. The mass term in this Hamiltonian is responsible for a gap in the spectrum of H_D[1]. If this term vanishes, i.e., $m \to 0$, then the quasi-particle dispersion is linear[1], as is the case for Dirac materials. For two-dimensional (2D) Dirac materials, these linear bands are a function of only two (out of three) components of the momentum, as can be seen from Equation 1.1. Thus, 2D Dirac materials are either truly 2D in real space, like **graphene**, or posses a 2D surface state exhibiting a linear dispersion relation, e.g., three-dimensional (3D) **topological insulators**. Another very important property of Dirac materials is the coupling of the momentum to a (pseudo-)spin. This coupling prevents back scattering in these materials and gives rise to spin-dependent transport properties[1, 3, 4].

As mentioned, the prevention of back scattering in the linearly dispersing bands leads to high electron transmission. Together with high mobilities of charge carriers, this protection against back scattering makes these materials very promising candidates for high performance electronics applications. For example, incorporation of these materials in field-effect transistor (FET) devices has been proposed and demonstrated[5–8]. Moreover, the spin-momentum coupling and other spin-related properties, like the spin polarization of graphene zig-zag (ZZ) edges, could be used for spin filtering and spintronics applications. Besides, some materials of this class exhibit remarkable optical properties, like high photon transmittance in the visible and infrared range[9–11]. In combination with a high mechanical flexibility, these materials have also been identified as promising candidates for transparent electrodes in flexible solar cells or other electronic devices[9–11]. Further potential applications of Dirac materials include, but are not limited to, energy storage[12–15], quantum computing[13] and sensing[16, 17].

Graphene and topological insulators: The carbon allotrope graphene had been object of theoretical studies[18–21] already long before it was experimentally isolated for the first time in 2004[22]. It has a honeycomb structure which arises from the sp^2-hybridization of the carbons s, p_x, and p_y orbitals. In graphene,

the hybridized orbitals of a given carbon atom form σ-bonds to its neighboring atoms. These bonds give graphene its extraordinary mechanical properties, while the p_z-orbitals, which are perpendicular to the graphene plane, form the π-bonds responsible for its outstanding electronic properties.

On the other hand, the existence of certain 3D materials exhibiting a topological phase was first predicted in the early 21st century[23, 24], based on earlier theoretical studies about topological order and the quantum spin Hall effect (QSHE)[25, 26]. Only a short time after these predictions, the first experimental realization of a 3D topological insulator (TI) was reported[27]. 3D TIs posses a linear dispersing 2D surface state protected by time-reversal symmetry and a 3D gapped bulk band structure[4, 28–30].

Materials characterization: Designing electronic devices based on novel materials requires a thorough understanding of their structural, chemical and electronic properties. Motivated by this demand, the theoretical and computational investigation of materials at the nanoscale has experienced tremendous activity in recent years[31]. To a great extent, this has been possible thanks to the advancement of methods based on first principles (*ab initio*). In particular, density functional theory (DFT)[32, 33] is currently the tool of choice[34, 35] for the simulation of ground-state structural and electronic properties of complex nanometer-scale systems of high technological interest, as graphene and topological insulators.

Moreover, in the context of nanoelectronics, the simulation of electronic transport properties across 2D materials connected to macroscopic conductors or electrodes is of particular relevance. As opposed to the standard DFT calculations, transport simulations involve open systems that are infinite, nonperiodic and out of equilibrium. Still, DFT based transport methods have been proven to be valid and helpful to describe a vast number of transport experiments. The most commonly employed method combines non-equilibrium Green's functions (NEGFs) with DFT electronic structure calculations[36–38].

Along with the above-mentioned computational methods, extraordinary experimental tools to measure and manipulate matter at the nanoscale are currently available. In particular, scanning tunneling microscopy (STM) has become a key technique to study and control matter at the atomic level[39, 40]. Interestingly,

many of the structures investigated experimentally can be modeled using first principles methods. In fact, because of the difficulty of experimentally investigating the influence of the detailed atomic structure on the electron transport properties, theoretical modeling is crucial for the interpretation of experimental observations. Beyond that, DFT based calculations can also guide experimental researchers in the selection of the most appropriate parameters to design their experiments.

This thesis focuses on the DFT study of electronic and transport properties of graphene based systems, and of the surface of a given family of topological insulators. Most of our work is reinforced with scanning tunneling microsopy (STM) experiments, which allow us to gain further insight into the physical and chemical characteristic of these nanostructures.

Outline

In **chapter 2** of this thesis, we introduce DFT for modeling materials. Starting from the many-body Hamiltonian and the Hohenberg-Kohn theorems, we will present the most important concepts and technical details in DFT.

Next, in **chapter 3** we will introduce an extension to DFT for transport calculations based on NEGF. Here, the fundamental concepts of NEGF methods and an efficient way to calculate Green's functions will be presented. Furthermore, our implementation of a tool for the calculation of multi-terminal eigenchannels will be discussed.

After the introduction of the methods applied in this thesis, we discuss the results we obtained for different Dirac-materials. We open this discussion of results with our work on metal-graphene contacts in **chapter 4**. By means of DFT based simulations, we study the structural and transport properties of two types of metal-graphene interfaces, namely side- and edge contacts. We consider different metal electrodes and investigate how the properties of these interfaces change upon passivation or contamination of the graphene edges.

In **chapter 5**, we present an extensive characterization of a new family of graphene nanoribbons (GNRs), the so-called 7-13 armchair GNR, and of the nanoporous graphene (NPG) which is obtained by fusing of these nanoribbons. By characterizing these materials computationally (DFT) and experimentally (STM), we demonstrate the existence of novel electronic states and how to influence these by morphological modifications or external perturbations.

Chapter 6 focuses on the influence of chemical disorder on the surface of a given family of topological insulators (TIs), with the aim of understanding the robustness of its topologically protected surface state against magnetic perturbations.

Chapter 7 summarizes the main results and conclusions presented in this thesis.

Chapter 2

Electronic structure methods

In computational physics and chemistry, different approaches can be followed to obtain the ground state properties of many-body systems. On one hand, Hartree-Fock or coupled cluster methods (and others) are based on the determination of the wave-function. These methods are usually computationally very expensive and, thus, can only be applied for smaller system (e.g., molecules). Alternatively, in density functional theory (DFT), the charge density is used to obtain the ground state properties of correlated quantum many-body systems[32, 33, 41]. This approach allows the treatment of realistic systems with hundreds and even thousands of atoms, and has proven to give reasonable results in a wide range of systems. For these reasons, over the last decades DFT has evolved to be the tool of choice for electronic structure calculations[34, 35].

2.1 The many-body problem

Calculating the properties of materials requires solving the Schrödinger equation for a system of interacting electrons and nuclei, i.e., diagonalizing the many-body Hamiltonian[42],

$$\hat{H} = -\frac{\hbar^2}{2m_e}\sum_i \nabla_i^2 - \sum_{i,I}\frac{Z_I e^2}{|\mathbf{r}_i - \mathbf{R}_i|} + \frac{1}{2}\sum_{i\neq j}\frac{e^2}{|\mathbf{r}_i - \mathbf{r}_j|} - \sum_I \frac{\hbar^2}{2M_I}\nabla_I^2 + \frac{1}{2}\sum_{I\neq J}\frac{Z_I Z_J e^2}{|\mathbf{R}_I - \mathbf{R}_J|} \tag{2.1}$$

with lower (upper) case subscripts denoting electrons (nuclei). In Equation 2.1, the first and fourth term are the kinetic energies of electrons and nuclei, respectively. The second and third term represent electron-nuclei and electron-electron interactions. Interactions between the nuclei are described by the last term.

In practice, solving the Schrödinger equation using the full many-body Hamiltonian, as shown in Equation 2.1, is not an easy task, and approximations are usually made. Commonly, the so-called Born-Oppenheimer or adiabatic approximation, as described in the following, is used. By fixing the positions of the nuclei the ionic kinetic energy term vanishes. Further, the ion-ion interaction term can be replaced by a constant energy term and electron-ion interactions by an external potential. This reduced Hamiltonian has then the following form,

$$\hat{H} = -\frac{\hbar^2}{2m_e}\sum_i \nabla_i^2 + \frac{1}{2}\sum_{i\neq j}\frac{e^2}{|\mathbf{r}_i - \mathbf{r}_j|} + V_{ext} + E_{II}, \tag{2.2}$$

with V_{ext} and E_{II} being the external potential and the ion-ion interaction energy, respectively. These simplifications are possible due the large ratio between the masses of nuclei and electrons. Hence, the motion of nuclei is very slow, and their positions quasi fixed, while electrons react almost instantaneously to changes in the external potential. Within this scenario, it is valid to neglect the kinetic energy terms for the nuclei[43].

2.2 Density Functional Theory

Hohenberg and Kohn used the simplified Hamiltonian from Equation 2.2 as the starting point for the development of DFT[32]. This theory is based on the observation that properties of a system of interacting particles can be described as a functional of the ground state density[42, 44]. In 1927, Thomas and Fermi proposed a density functional theory of quantum systems which neglected exchange and correlation between electrons[45, 46]. Later, Dirac extended Thomas-Fermi theory to include a local approximation for electronic exchange[44]. While the theory of Thomas and Fermi is just an approximation, Hohenberg and Kohn formulated DFT as an exact many-body theory[32, 41, 42]. Their formulation is

applicable to any system of interacting particles moving in an external potential.

Hohenberg-Kohn Theorems

Hohenberg and Kohn based their theory on two theorems[32, 41], which we will discuss shortly here. The first theorem states that the ground state density $n_0(\mathbf{r})$ of any system of interacting particles is sufficient to uniquely, except for a constant, determine the external potential $V_{ext}(\mathbf{r})$ acting on the particles. From this theorem follows that, since the Hamiltonian is fully determined up to a constant shift in energy, the electronic states of a system can be determined from the ground state density $n_0(\mathbf{r})$[42].

The second theorem describes the possibility to define a universal functional $E[n]$, valid for any external potential $V_{ext}(\mathbf{r})$, for determining the energy in terms of the density $n(\mathbf{r})$. Then, the exact ground state density $n_0(\mathbf{r})$ is the one which minimizes this energy functional. Therefore, knowing the functional $E[n]$ is sufficient to determine the ground state energy and density.

Within the Hohenberg-Kohn formulation of DFT, a functional for the energy can be written as follows[32, 42],

$$E_{HK}[n] = T[n] + E_{int}[n] + \int d^3r V_{ext}(\mathbf{r})n(\mathbf{r}) + E_{II}, \tag{2.3}$$

$T[n]$ being a functional of the kinetic energies of the interacting particles, $E_{int}[n]$ describing the interaction energy of the electrons and E_{II} the interaction energy of the nuclei. Using a functional of the form of Equation 2.3 to obtain the ground state density leaves one with the following problem: in principle, the ground state density is sufficient to determine properties of a material. But, no one has found a way to extract these properties, e.g., the density of states (DOS), directly from the density yet[42].

Kohn-Sham Equations

To circumvent the challenge of extracting material properties directly from the ground state density, in 1965 Kohn and Sham proposed a new approach. In their ansatz, they assumed that the ground state properties of a system of interacting

particles can be described by the ground state of some non-interacting system[33]. Based on this assumption, they introduced an auxiliary system of independent electrons with its density given by[33]

$$n(\mathbf{r}) = \sum_{i=1}^{N} |\phi_i^{KS}(\mathbf{r})|^2. \tag{2.4}$$

In Equation 2.4, $\phi_i^{KS}(\mathbf{r})$ denote the single particle wave-functions of the non-interacting auxiliary system, the so-called Kohn-Sham orbitals. Whether a precise physical meaning can be assigned to these Kohn-Sham orbitals is a widely debated issue[33, 42, 47, 48]. The only exception is the highest occupied orbital, which has been shown to correspond to the exact ionization energy of a system in exact Kohn-Sham DFT[49].

Within the Kohn-Sham formalism, the kinetic energy is not given in the form of a functional of the density of the interacting system but rather as a sum of independent particle energies in terms of the Kohn-Sham orbitals[42]:

$$T_s = \frac{1}{2} \sum_{i=1}^{N} \int d^3r |\nabla \phi_i^{KS}(\mathbf{r})|^2. \tag{2.5}$$

Additionally, the part of the Coulomb interaction energy which represents the energy of the electron density interacting with itself, i.e., the Hartree energy [32, 42],

$$E_{Hartree}[n] = \frac{1}{2} \int \int d^3r d^3r' \frac{n(\mathbf{r})n(\mathbf{r}')}{|\mathbf{r} - \mathbf{r}'|} \tag{2.6}$$

is separated from other classic Coulombic contributions. Now, the functional for the total energy can be written as[42]

$$E_{KS} = T_s[n] + \int d^3r V_{ext}(\mathbf{r})n(\mathbf{r}) + E_{Hartree}[n] + E_{II} + E_{xc}[n]. \tag{2.7}$$

Since the ground state densities of the interacting and non-interacting systems are required to be equal, by comparison of the Hohenberg-Kohn (Equation 2.3) and the Kohn-Sham (Equation 2.7) total energy functionals, a formal expression for the exchange-correlation energy can be derived[42]:

$$E_{xc}[n] = T[n] - T_s[n] + E_{int}[n] - E_{Hartree}[n]. \tag{2.8}$$

Equation 2.8 reveals that the exchange-correlation energy is just the difference of the kinetic and interaction energies between the interacting and the non-interacting systems. If the exact form of the functional defined in Equation 2.8 were known, the exact ground state energy and density of a system of interacting electrons could be found by solving the equations for the non-interacting system. While the form of the exact exchange-correlation functional is unknown, a wide variety of different approximations for $E_{xc}[n]$ have been developed in the last decades[50–57]. A few types of exchange-correlation approximations will be discussed briefly in the next subsection.

Exchange-Correlation Functionals

Local density approximation (LDA): The LDA is the simplest approximation for the exchange-correlation energy and was already proposed by Kohn und Sham in their original paper[33]. As the name suggests, in the LDA the exchange-correlation energy only depends on the local structure of the electron density[33, 42],

$$E_{xc}^{LDA}[n(\mathbf{r})] = \int d^3r n(\mathbf{r}) \epsilon_{xc}^{hom}[n(\mathbf{r})], \tag{2.9}$$

where $\epsilon_{xc}^{hom}[n(\mathbf{r})]$ denotes the exchange-correlation energy of the homogeneous electron gas with density $n(\mathbf{r})$. While the form of the exchange part of ϵ_{xc}^{hom} is known exactly[42],

$$\epsilon_x^{hom} = -\frac{3}{4}\left(\frac{3n(\mathbf{r})}{\pi}\right)^{1/3}, \tag{2.10}$$

the correlation part ϵ_c^{hom} needs to be calculated numerically, e.g., using Monte Carlo methods[57]. The results of such numeric calculations are often parametrized to obtain more general expressions for the correlation energy of the homogeneous electron gas in the form of a density functional[55, 56]. The LDA is a very useful approximation for solids with slowly varying electron density and calculations of

bulk and surface properties have been carried out, proving its accuracy for such systems[58].

Generalized gradient approximation (GGA): Inspired by the success of LDA, the so-called GGA functionals were developed, which not only depend on the density but also on its gradient. The general form of a GGA functional can be written as follows[42, 59],

$$E_{xc}^{GGA}[n(\mathbf{r})] = \int d^3r n(\mathbf{r}) \epsilon_{xc}[n(\mathbf{r}), |\nabla n(\mathbf{r})|]. \tag{2.11}$$

The term for the exchange-correlation energy ϵ_{xc} in Equation 2.11 can also be written as a product of the exchange energy of the homogeneous electron gas (ϵ_x^{hom}) and a dimensionless functional describing correlation and additional exchange effects[42, 59].

One of the most commonly used GGA flavors[35] was proposed by Perdew, Burke, and Ernzerhof in the year 1996[53, 54], and is now known as PBE exchange-correlation functional. The popularity of the PBE functional can be attributed to its wide range applicability, i.e., the fact that it performs well for a variety of properties of different systems, from molecules[53, 60–62] to bulk solids[63, 64].

Functionals including van der Waals (vdW) interactions: Within LDA and GGA functionals, the exchange-correlation energy only depends on the electron density and its gradient. Hence, the character of these exchange-correlation functionals is either *local* or *semi-local*. For an accurate description of the long range vdW interactions, *non-local* correlation terms have to be included in the functional. These terms represent the interactions between induced dipoles, which arise due to spontaneous fluctuations of the polarization of the charge density. Many vdW functionals are based on GGA and LDA, extending these approximations by including a non-local correlation energy functional.

Two approaches to include vdW interactions in a functional are very common. The first one is a semi-empirical approach and was developed by Grimme[65]. Here, the vdW parameters have to be specified by the user and can be obtained from high-quality *ab-initio* calculations separately for each element of the peri-

odic table[65]. In the second approach, the vdW parameters are calculated self-consistently within the formalism of the functional. Such a functional is, for example, the optB88 functional developed by Klimeš *et al*[50].

2.3 DFT implementation details

So far, the main concepts of DFT have been discussed on a general level. From here on, we will introduce more technical concepts that depend on the implementation of DFT and the type of system under investigation.

Periodic boundary conditions

Simulating infinite, periodic systems (e.g., crystal structures) is done by choosing a unit of repetition, called *unit cell*, and applying periodic boundary conditions. The choice of the unit cell is not unique and it is described by the so-called *lattice vectors* $\mathbf{a}_i$. One constraint in the choice of the unit cell is given by the periodic boundary conditions. These require physical quantities, like the electrostatic potential or the electron wave-functions, to be continuous at the cell boarders.

According to Bloch's theorem[66], each eigenfunction of any Hamiltonian describing electrons moving in a periodic electrostatic potential can be written as the product of a plane wave and a periodic function $u(\mathbf{r})$,

$$\psi(\mathbf{r}) = e^{i\mathbf{kr}}u(\mathbf{r}). \tag{2.12}$$

Hence, the wave-function of a system only has to be calculated within the unit cell and can then be extended to the wave-function of the infinite system by multiplication with plane waves.

Pseudopotentials

Chemical bonding is dominated by the valence electrons, i.e., electrons in the outer shell of an atom. On the other hand, the electrons of the inner closed shells, called core electrons, do not usually play a big role in chemical processes. Besides, the orthogonality of core and valence electrons leads to rapidly varying electron

wave-functions close to the atom's core, i.e., to wave-functions possessing nodes. Since the computational treatment of fast oscillations in the wave-functions is very expensive, approximations are required to simplify their description.

Within this context, the idea of pseudopotentials is to replace the original electrostatic potential of a nucleus by a potential leading to smoothly varying nodeless wave-functions in the core region. Additionally, a static description of the core electrons and their effects, like screening of the ionic potential, are included in a pseudopotential. As a result, the number of electrons that need to be fully treated in a self-consistent fashion is reduced, effectively alleviating the computational cost of *ab-initio* calculations.

Pseudopotentials have to obey a few constraints as given by Hamann, Schlüter and Chiang[67]. In an nutshell, beyond a given radius the wave-functions generated by a pseudopotential have to be the same as all-electron wave-functions, and, within this radius, the integrated charges of pseudo and all-electron wave-functions have to be equal. Different types of pseudopotentials fulfilling above constraints have been developed, like norm-conserving[67, 68] or ultrasoft pseudopotentials[69].

Basis Sets: Localized Orbitals or Plane Waves

The many-body Schrödinger equation represents a set of partial differential equations, which can be converted into a set of algebraic equations by a suitable choice of functions to describe the electronic wave-functions[70]. Subsequently, the algebraic equations can be solved efficiently using numerical methods. The choice of functions for the representation of the wave-function is called *basis set*. Accordingly, the accuracy of DFT calculations depends both on the selection of the exchange-correlation functional as well as on the basis set[71–75].

The two main types of basis sets are i) *plane waves*, as used in the Vienna Ab-inition Simulation Package (VASP)[76–79] and Quantum Espresso[80] codes, and ii) *linear combination of atomic orbitals (LCAO)*, as applied in methods like the Spanish Initiative for Electronic Simulations with Thousands of Atoms (SIESTA)[81] and its extension TranSIESTA[36, 37]. While plane wave basis sets lead to very accurate results and are easy to expand, using LCAO as basis allows

to perform faster calculations of larger systems. Since we used both types of basis sets in our work, we will shortly review them here.

Plane wave basis sets: The eigenfunctions of a Hamiltonian for independent particles within the Kohn-Sham formalism satisfy the following eigenvalue equation[42],

$$\hat{H}_{eff}(\mathbf{r})\psi_i^{KS}(\mathbf{r}) = \left[-\frac{1}{2}\nabla^2 + V_{eff}(\mathbf{r}) \right] \psi_i^{KS}(\mathbf{r}) = \epsilon_i \psi_i^{KS}(\mathbf{r}), \tag{2.13}$$

where, excluding the kinetic energy, V_{eff} represents the terms on the right hand side of Equation 2.7. Taking advantage of the fact that any periodic function can be expanded in a complete set of Fourier components[42], the eigenfunctions can be written based on plane waves,

$$\psi_i^{KS}(\mathbf{r}) = \frac{1}{\sqrt{\Omega}} \sum_{\mathbf{q}} c_{i,\mathbf{q}} \times e^{i\mathbf{qr}} \equiv \sum_{\mathbf{q}} c_{i,\mathbf{q}} \times |\mathbf{q}\rangle. \tag{2.14}$$

In this equation, Ω represents the volume of the cell for which the Hamiltonian in Equation 2.13 is defined, $c_{i,\mathbf{q}}$ are the wave-function coefficients, and $\mathbf{q}$ corresponds to points on a grid in reciprocal space. The plane waves have to be orthonormal, i.e., they have to satisfy the following condition[42],

$$\langle \mathbf{q}' | \mathbf{q} \rangle = \delta_{\mathbf{q}'\mathbf{q}}. \tag{2.15}$$

Now, one can plug Equation 2.14 into the eigenvalue equation (Equation 2.13) and multiply from the left by $\langle \mathbf{g}' |$. This way, one obtains the Schrödinger equation in Fourier space (i.e., the eigenvalue equation in a plane wave basis)[42],

$$\sum_{\mathbf{q}} \langle \mathbf{q}' | \hat{H}_{eff} | \mathbf{q} \rangle c_{i,\mathbf{q}} = \epsilon_i c_{i,\mathbf{q}'}. \tag{2.16}$$

The left side of this equation is only non-zero when $\mathbf{q}$ equals $\mathbf{q}'$ or if they differ by some reciprocal lattice vector. From the last equation one can see that, plane wave basis sets are variational and can be easily extended by increasing the number of plane waves.

LCAO basis set: In this approach, as the name suggests, the basis set is built up by a linear combination of orbitals centered on the positions of the ions. Due to the lowering of the total energy upon binding in molecules or solids, the amplitude of the electron wave-function is higher at the nucleus and its range is reduced as compared to the free atom electron wave-function[42, 70]. Therefore, free atom orbitals modified in this way are a good starting point for an orbital based basis set. By strictly confining the orbitals within a given cut-off radius, one can ensure sparsity of the Hamiltonian matrix[81]. Within this cut-off radius, the basis set orbitals of atom I, located at $\mathbf{R}_I$, can be written as the product of a radial function and a spherical harmonic[42, 81],

$$\phi_{Inlm}(\mathbf{r}) = \phi_{Inl}(r_I) * Y_{lm}(\mathbf{r}_I), \tag{2.17}$$

where $\mathbf{r}_I = \mathbf{r} - \mathbf{R}_I$. The labels n, l and m represent the principal, angular momentum and magnetic quantum numbers, respectively. Often, more than one orbital per atom with the same n and l, but varying radial dependence, is used. These basis sets are then called "multiple-ζ" (e.g., double-ζ or DZ for two orbitals) basis sets[42, 81]. Additionally, to improve the description of the non-spherical environments of atoms in molecules and solids, so-called *polarization orbitals* are often included. These orbitals possess angular momentum quantum numbers larger than the maximum l of the valence orbitals[42, 70, 81]. For calculations using the SIESTA method, double-ζ-polarized (DZP) basis sets have proven to be, in most cases, a good compromise between high accuracy and low computational cost[81].

Spin Orbit Coupling

In the formalism considered above, the spin degree of freedom has been neglected. To include it in DFT, two possible scenarios have to be taken into account, namely *collinear* and *non-collinear* spin configurations. For the more common case of collinear spins, the total charge density $n(\mathbf{r})$ can be expressed in terms of spin up $n^{\uparrow}(\mathbf{r})$ and spin down $n^{\downarrow}(\mathbf{r})$ densities. However, a more general description of magnetism requires a variable spin axis, also known as *non-collinear* spin polarization. This generalized description of the spin degree of freedom relies on the solution of

the Schrödinger equation in its covariant relativistic form as proposed by Dirac in 1928[82, 83],

$$i\hbar\frac{\partial}{\partial t}\psi = (c\sum_{i=1}^{3}\alpha_i p_i + \beta mc^2)\psi, \tag{2.18}$$

and allows for an accurate treatment of relativistic effects in DFT. In Equation 2.18, ψ is a four-component single-particle wave-function describing spin-$\frac{1}{2}$ particles, $p_i = -i\hbar\nabla_i$ are the components of the standard momentum operator, and α_i and β are 4×4 matrices of the following form[42, 82, 83],

$$\alpha_i = \begin{pmatrix} 0 & \sigma_i \\ \sigma_i & 0 \end{pmatrix}, \qquad \beta = \begin{pmatrix} \mathbb{1} & 0 \\ 0 & -\mathbb{1} \end{pmatrix}. \tag{2.19}$$

The unit entries $\mathbb{1}$ of β are 2×2 unit matrices and the σ_i represent the 2×2 Pauli spin matrices,

$$\sigma_x = \begin{pmatrix} 0 & 1 \\ 1 & 0 \end{pmatrix}, \qquad \sigma_y = \begin{pmatrix} 0 & -i \\ i & 0 \end{pmatrix}, \qquad \sigma_z = \begin{pmatrix} 1 & 0 \\ 0 & -1 \end{pmatrix}. \tag{2.20}$$

One of the relativistic effects which requires a *non-collinear* treatment of spin is the so-called spin-orbit coupling (SOC). The origin of this effect is the interaction between an electron's intrinsic magnetic moment, which is directly proportional to its spin angular momentum $\mathbf{S}$, and the apparent magnetic field of the nucleus that the electron experiences from its perspective.

From the Dirac equation (2.18) a spin-orbit term can be derived. This term has to be added to the Hamiltonian and has the following form[42],

$$\hat{H}_{SO} \propto \frac{1}{r}\frac{dV}{dr}\mathbf{L}\cdot\mathbf{S}. \tag{2.21}$$

Here, V is the nuclear electrostatic potential, r corresponds to the distance of the electron from the atom, $\mathbf{L} = \mathbf{r}\times\mathbf{p}$ denotes the electron's angular momentum and $\mathbf{S}$ its spin angular momentum. Often, the expression in Equation 2.21 can be treated as a small perturbation and, since it is large only close to the atom's nucleus, it is valid not only for free atoms but also for atoms in molecules and solids[42].

In the *non-collinear* formulation of DFT, a local spin density matrix is de-

fined[42, 84],

$$n^{\alpha\beta}(\mathbf{r}) = \sum_i \psi_i^{\alpha*}(\mathbf{r})\psi_i^{\beta}(\mathbf{r}), \tag{2.22}$$

where α and β represent the spin degrees of freedom and the sum runs over all the occupied states of the system. In this formalism, the local spin density matrix $n^{\alpha\beta}(\mathbf{r})$, and, therefore, also the Kohn-Sham Hamiltonian, is a 2×2 matrix[42].

DFT+U methods

An accurate determination of the electronic properties of systems with strongly correlated electrons, e.g. transition metals with highly localized 3d-orbitals, applying standard DFT has been proven to be difficult[42, 85, 86]. Therefore, based on the Hubbard model[87–89], extensions to DFT taking strong electron-electron correlations into account have been developed[85, 86, 90–94]. In these approaches, referred to as DFT+U, an on-site energy term is added to the Hamiltonian for highly localized orbitals.

The DFT+U method we applied in this work was developed by Dudarev et al.[90]. In their ansatz, the energy correction term E^U, which is added to the energy obtained by DFT, has the following form[90],

$$E^U = \frac{U-J}{2} \sum_\sigma \left[\left(\sum_{m1} n_{i,i}^\sigma \right) - \left(\sum_{i,j} n_{i,j}^\sigma n_{j,i}^\sigma \right) \right]. \tag{2.23}$$

In this equation, $n_{i,j}$ represents the density matrix of the localized orbitals for which the correction is applied, σ denotes the spin, and U and J are the averaged Coulomb and exchange parameters.

Chapter 3

Quantum transport simulations

In the previous chapter, we introduced the basics of DFT, a method for electronic structure calculations of periodic systems. To perform transport simulations, on the other hand, electronic structure methods have to be extended to include the effects of semi-infinite electron reservoirs (denoted as electrodes or terminals) and, consequently, open boundary conditions. Modern transport extensions to electronic structure methods rely on one of two very different approaches. The first one is based on scattering states, which are defined as wave-functions satisfying the Schrödinger equation and specific open boundary conditions[95]. More recent implementations of this approach allow solving the scattering states using existing DFT codes[95–97].

The more commonly used approach combines electronic structure from DFT with NEGFs[36–38, 98–100]. This formalism allows the treatment of open boundary conditions and ballistic transport. Recent developments of this NEGF approach allow for flexible transport geometries and the use of more than two electrodes[37, 38]. In this chapter, we will discuss the basic principles of the NEGF method and how to efficiently calculate the Green's function. Also, we introduce a new tool developed to visualize electron transmission channels for nanosystems coupled to more than two electrodes.

3.1 NEGF based transport

Here, we will introduce important concepts of the NEGF formalism, starting with the eigenvalue equation in a non-orthonormal basis,

$$\mathbf{H}\psi = \epsilon\mathbf{S}\psi, \tag{3.1}$$

with the Hamiltonian matrix $\mathbf{H}$ and the overlap matrix $\mathbf{S}$. The equilibrium Green's function is then defined by the following expression[101],

$$(\epsilon\mathbf{S} - \mathbf{H})\mathbf{G}(\epsilon) = \mathbf{I}. \tag{3.2}$$

The elements of the overlap matrix $\mathbf{S}$ can be defined in terms of the basis functions ϕ_i as follows,

$$S_{ij} = \int d\mathbf{r}\phi_i^*(\mathbf{r})\phi_j(\mathbf{r}). \tag{3.3}$$

To extend this formalism to non-equilibrium situations, it is necessary to introduce the concept of *self-energies*. Here, we will do this by looking at a representative system comprised of two semi-infinite electrodes (e1 and e2) and a device region (d), schematically depicted in Figure 3.1. In such a scenario, the total Hamiltonian can be split into the Hamiltonians of the electrodes and the device region[36],

$$\mathbf{H} = \begin{pmatrix} \mathbf{H}_{e1} + \mathbf{\Sigma}_{e1} & \mathbf{V}_{e1} & 0 \\ \mathbf{V}_{e1}^\dagger & \mathbf{H}_d & \mathbf{V}_{e2} \\ 0 & \mathbf{V}_{e2}^\dagger & \mathbf{H}_{e2} + \mathbf{\Sigma}_{e2} \end{pmatrix}. \tag{3.4}$$

Here, $\mathbf{H}_i$ denote the Hamiltonian matrices of the electrodes (e1, e2) and the device region (d), $\mathbf{\Sigma}_i$ denote the electrodes' self-energies and $\mathbf{V}_i$ are the terms describing

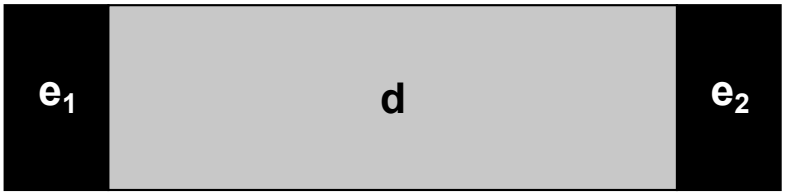

Figure 3.1: Schematic illustration of a system with two semi-infinite electrodes (e_1 and e_2) attached to a scattering or device region (d).

the coupling of the electrodes to the device region.

The Hamiltonians for the electrodes ($\mathbf{H}_{e1}$ and $\mathbf{H}_{e2}$) are obtained from electronic structure calculations with periodic boundary conditions for each electrode separately. Moreover, to model the effects of open boundary conditions, one needs to include the electrodes' self-energy terms ($\mathbf{\Sigma}_{e1}$ and $\mathbf{\Sigma}_{e2}$). For each electrode e, the self-energy can be defined in terms of the electrode's equilibrium Green's function $\mathbf{G}_e(\epsilon)$ (calculated according to the definition in Equation 3.2) and the coupling terms $\mathbf{V}_e$ connecting the electrodes and the device region (see Equation 3.4)[36, 101],

$$\mathbf{\Sigma}_e(\epsilon) = \mathbf{V}_e^\dagger \mathbf{G}_e(\epsilon) \mathbf{V}_e. \tag{3.5}$$

Now, using the Equations 3.2 and 3.5, we can calculate the non-equilibrium Green's function for our two electrode system as follows,

$$\mathbf{G}(\epsilon) = \Big(\epsilon\mathbf{S} - \mathbf{H} - \mathbf{\Sigma}_{e1}(\epsilon) - \mathbf{\Sigma}_{e2}(\epsilon)\Big)^{-1}. \tag{3.6}$$

Two useful quantities, that can be calculated from the Green's function, are the spectral function and the so-called broadening matrix. The density of states (DOS) and all solutions to the Schrödinger equation can be obtained via the spectral function of the Green's function. A proof of this statement can be found in Ref. [101] where the spectral function A is defined as,

$$A = i(G - G^\dagger). \tag{3.7}$$

A more efficient way to compute the spectral function of each electrode is derived by defining it in terms of the corresponding broadening matrix and the device region's Green's function[37],

$$\mathbf{A}_e(\epsilon) = \mathbf{G}(\epsilon) \mathbf{\Gamma}_e(\epsilon) \mathbf{G}^\dagger(\epsilon). \tag{3.8}$$

In this equation, $\mathbf{\Gamma}_e$ is the broadening matrix and can be expressed in terms of the electrodes' self-energies[37],

$$\mathbf{\Gamma}_e(\epsilon) = i\left[\mathbf{\Sigma}_e(\epsilon) - \mathbf{\Sigma}_e^\dagger(\epsilon)\right]. \tag{3.9}$$

Calculating the transmission from the Green's function

The electron transmission from electrode one (e_1) to electrode two (e_2) can be calculated using the non-equilibrium Green's function (Equation 3.6)and the broadening matrices (Equation 3.9) of the electrodes[36, 37],

$$T_{e1,e2}(\epsilon) = Tr\left[\mathbf{G}(\epsilon)\mathbf{\Gamma}_{e1}(\epsilon)\mathbf{G}^{\dagger}(\epsilon)\mathbf{\Gamma}_{e2}(\epsilon)\right]. \tag{3.10}$$

Alternatively, it can be expressed as the sum of the positive eigenvalues $T_{i,e1,e2}$ of the column matrix $\mathbf{G}(\epsilon)\mathbf{\Gamma}_{e1}(\epsilon)\mathbf{G}^{\dagger}(\epsilon)\mathbf{\Gamma}_{e2}(\epsilon)$[37, 101],

$$T_{e1,e2}(\epsilon) = \sum_i T_{i,e1,e2}(\epsilon). \tag{3.11}$$

From the transmission, the current flowing between the two electrodes can be calculated as follows[36, 37],

$$I_{e1,e2} = \frac{G_0}{2|e|}\int d\epsilon T_{e1,e2}(\epsilon)\left[n_{F,e2}(\epsilon) - n_{F,e1}(\epsilon)\right], \tag{3.12}$$

where G_0 is the conductance quantum and $n_{F,ei}$ is the Fermi-function of electrode e_i.

So far, we only considered a simplified system with two electrodes. However, the formalism discussed above can be generalized for systems with an arbitrary number n of electrodes by including the self-energies of all terminals in the Green's function[37],

$$\mathbf{G}(\epsilon) = \left(\epsilon\mathbf{S} - \mathbf{H} - \sum_{e=1}^{n}\mathbf{\Sigma}_e(\epsilon)\right)^{-1}. \tag{3.13}$$

Efficient calculation of the Green's function

The computationally most expensive part in transport calculations using NEGF methods is the inversion of the Hamiltonian matrix to obtain the Green's function. For a special type of matrices, namely the so-called *block-tri-diagonal (BTD)* matrices, very effective inversion algorithms have been developed[102–104] and

implemented in TranSIESTA[37]. BTD matrices have the following form,

$$\begin{pmatrix} \mathbf{A}_1 & \mathbf{C}_2 & 0 & \cdots & \cdots & 0 \\ \mathbf{B}_1 & \mathbf{A}_2 & \mathbf{C}_3 & 0 & \cdots & 0 \\ 0 & \mathbf{B}_2 & \mathbf{A}_3 & \mathbf{C}_4 & 0 & 0 \\ \vdots & 0 & \ddots & \ddots & \ddots & 0 \\ \vdots & \vdots & 0 & \mathbf{B}_{N-2} & \mathbf{A}_{N-1} & \mathbf{C}_N \\ 0 & 0 & 0 & 0 & \mathbf{B}_{N-1} & \mathbf{A}_N \end{pmatrix}. \tag{3.14}$$

Here, only the matrices along the main diagonal ($\mathbf{A}_i$) as well as the ones along the first upper ($\mathbf{B}_i$) and first lower ($\mathbf{C}_i$) diagonals have non-zero elements. A BTD matrix can be created from any sufficiently sparse matrix by swapping columns and rows, a process known as pivoting. For example, for the two electrode Hamiltonian defined in Equation 3.4 of the previous sub-section, $\mathbf{A}_1$ corresponds to the Hamiltonian plus self-energy for the first electrode ($\mathbf{H}_{e1} + \mathbf{\Sigma}_{e1}$), $\mathbf{B}_1$ and $\mathbf{C}_2$ are equal to $\mathbf{V}_{e1}^{\dagger}$ and $\mathbf{V}_{e1}$, the terms coupling electrode one to the device region, $\mathbf{A}_2$ represents the device region's Hamiltonian $\mathbf{H}_d$. Suitable pivoting may allow further division of the device region's Hamiltonian $\mathbf{H}_d$ into smaller blocks, then represented by a series of $\mathbf{A}_n$-blocks and connected by the corresponding $\mathbf{B}_{n-1}$- and $\mathbf{C}_n$-blocks. Further, $\mathbf{A}_3$, $\mathbf{B}_2$, and $\mathbf{C}_3$ correspond to the Hamiltonian (including the self-energy, $\mathbf{H}_{e2} + \mathbf{\Sigma}_{e2}$) and the coupling terms $\mathbf{V}_{e2}^{\dagger}$ and $\mathbf{V}_{e2}$ of the second electrode, respectively.

Once the inverse of the Green's function matrix defined in Equation 3.6 has been brought into the form of a BTD matrix (see Equation 3.14), the following auxiliary matrices can be defined[37],

$$\begin{aligned} \tilde{\mathbf{Y}}_n &= \left[\mathbf{A}_{n-1} - \mathbf{Y}_{n-1}\right]^{-1} \mathbf{C}_n, \qquad \mathbf{Y}_1 = 0, \qquad \mathbf{Y}_n = \mathbf{B}_{n-1}\tilde{\mathbf{Y}}_n, \\ \tilde{\mathbf{X}}_n &= \left[\mathbf{A}_{n+1} - \mathbf{X}_{n+1}\right]^{-1} \mathbf{B}_n, \qquad \mathbf{X}_p = 0, \qquad \mathbf{X}_n = \mathbf{C}_{n+1}\tilde{\mathbf{X}}_n. \end{aligned} \tag{3.15}$$

For the calculation of $\tilde{\mathbf{X}}_n$ and $\tilde{\mathbf{Y}}_n$ it is not necessary to carry out the matrix inversion. Instead, these matrices can be computed using a linear solution and subsequent matrix multiplication of the respective equations[37]. The $\mathbf{X}_n$ and $\mathbf{Y}_n$ matrices can be interpreted as self-energies connecting consecutive blocks. This

interpretation becomes more apparent when looking at the expressions for calculating the blocks of the Green's function matrix[37],

$$\begin{aligned} \mathbf{G}_{n,n} &= \left[\mathbf{A}_n - \mathbf{X}_n - \mathbf{Y}_n\right]^{-1}, \\ \mathbf{G}_{m-1,n} &= -\tilde{\mathbf{Y}}_m \mathbf{G}_{m,n} \qquad \text{for } m \leq n, \\ \mathbf{G}_{m+1,n} &= -\tilde{\mathbf{X}}_m \mathbf{G}_{m,n} \qquad \text{for } m \geq n. \end{aligned} \tag{3.16}$$

The last two lines define the backward and forward propagation of the Green's function along the columns of the matrix.

Implementation of multi-terminal eigenchannel tool

The formalism described above can be used to calculate the so-called transmission eigenchannels, which are very useful for a detailed analysis of the transport properties of a system[105]. These eigenchannels are linear combinations of scattering states, i.e., of wave-functions with a certain energy which satisfy the Schrödinger equation and open boundary conditions[95]. The eigenchannels, which have a well defined transmission, can be interpreted as wave-functions of electrons injected into the system from one terminal with a certain energy and momentum, and propagating to another electrode. From the spatial form of these wave-functions, areas of scattering within the device region can be identified. Hence, the transmission eigenchannels are very helpful in determining bottlenecks for the transmission of electrons in a given system.

Within this thesis, we implemented a tool for calculating multi-terminal eigenchannels, based on the BTD method and on the propagation of the spectral function eigenvectors. The *Python* script we developed for this purpose relies on the tight-binding library *Sisl*[106] developed by Nick Papior, which allows to read in Hamiltonian matrices and to perform linear algebra operations. Besides, our implementation uses methods from the *Inelastica* code[107] to set up the basis functions and to calculate the eigenchannels on a real space grid, as well as different capabilities of the *Python* libraries *SciPy*[108] and *NumPy*[109].

Our code first loads the Hamiltonian and overlap matrices for the electrodes and the whole system for a given energy and k-point. These matrices might have

been obtained with DFT or tight-binding and must be provided in a *Sisl*[106] compatible format. After calculating the self-energies for all the electrodes, the above described BTD method is used to calculate the Green's function block matrix corresponding to the electrode from which the eigenchannels should originate. Finally, we calculate the eigenchannels as outlined below and use basis functions extracted from SIESTA[81] calculations to compute the eigenchannel wave-functions.

In the following, this procedure for computing the eigenchannels will be described in detail. Taking into account that Green's functions are propagators, the eigenchannels can be obtained by propagating the eigenvectors of the spectral function of an electrode using the $\tilde{\mathbf{X}}$ and $\tilde{\mathbf{Y}}$ from Equation 3.15.

We begin by evaluating the spectral matrix of block n (containing the matrix elements of electrode e) following Equation 3.8,

$$\mathbf{A}^{e}_{n,n} = \mathbf{G}_{n,n}\mathbf{\Gamma}_{e}\mathbf{G}^{\dagger}_{n,n}. \tag{3.17}$$

Diagonalizing this matrix gives the eigenvectors $\mathbf{U}_n$ and eigenvalues λ_e of the spectral function of block n. The eigenvalues λ_e represent the magnitude of the DOS carried by the corresponding eigenvector. Now, similar to the propagation of the Green's function defined in the last two lines of Equation 3.16, the eigenvectors of the spectral function can be propagated forward and backward along the column,

$$\begin{aligned} \mathbf{U}_{n+1} &= -\tilde{\mathbf{X}}_n\mathbf{U}_n \qquad (forward), \\ \mathbf{U}_{n-1} &= -\tilde{\mathbf{Y}}_n\mathbf{U}_n \qquad (backward). \end{aligned} \tag{3.18}$$

The propagated eigenvectors span the full vector space of the eigenchannels originating from electrode e,

$$\mathbf{U} = \begin{pmatrix} \mathbf{U}_0 \\ \mathbf{U}_1 \\ \vdots \\ \mathbf{U}_N \end{pmatrix}. \tag{3.19}$$

In principle, the eigenvectors could be propagate far into the electrode to see how they decay in the bulk, provided that the Hamiltonian is extended correspondingly.

This vector of block matrices is used to define the norm,

$$||\mathbf{U}|| = \mathrm{diag}\left(\sum_i \mathbf{U}_{\mathbf{ij}}^{\dagger}\mathbf{U}_{\mathbf{ij}}\right) = \mathrm{diag}\left(\mathbf{u}_{\mathbf{j}}^{*}\mathbf{u}_{\mathbf{j}}\right), \tag{3.20}$$

where $\mathbf{u_j}$ is the the j-th column of $\mathbf{U}$. Then, the renormalization of the propagated eigenvectors and eigenvalues is done in the following way,

$$\begin{aligned} \lambda_e &= \lambda_e||\mathbf{U}||, \\ \mathbf{U} &= \frac{\mathbf{U}}{\sqrt{||\mathbf{U}||}}. \end{aligned} \tag{3.21}$$

Normalizing the eigenvalues might swap states, .i.e., the eigenvalues are not sorted from highest to lowest anymore. Therefore, eigenvalues and eigenvectors have to be resorted. Before calculating the eigenchannels originating in electrode e and propagating into electrode e', an orthogonal basis transformation has to be performed on the broadening matrix $\Gamma_{e'}$ of the target electrode,

$$\begin{aligned} \tilde{\mathbf{U}} &= \sqrt{\lambda_{e'}}\mathbf{U}, \\ \tilde{\mathbf{\Gamma}}_{e'} &= \tilde{\mathbf{U}}^{\dagger}\mathbf{\Gamma}_{e'}\mathbf{U}. \end{aligned} \tag{3.22}$$

Diagonalizing $\tilde{\mathbf{\Gamma}}_{e'}$ gives both the transmissions and the wave-function coefficients $\tilde{\mathbf{c}}$ of the eigenchannels. The coefficients $\tilde{\mathbf{c}}$ contain information about the contribution of each eigenvector $\mathbf{U}$ to a given eigenchannel. Finally, transforming the wave-function coefficients back to the non-orthogonal basis,

$$\mathbf{c} = \frac{\tilde{\mathbf{U}}\tilde{\mathbf{c}}}{\sqrt{2\pi}}, \tag{3.23}$$

one can use the basis functions to create real space representations of the eigenchannels.

Example

To illustrate the capabilities of the multi-terminal eigenchannels tool, we consider the model system depicted in Figure 3.2a, which consists of four carbon based

terminals with an asymmetrically placed pore in the central region. For simplicity, we used a tight-binding model including only nearest neighbor hopping to obtain the Hamiltonians. The green shaded areas indicate the electrodes used in this calculations. The hopping parameter in our tight-binding model was 2.7 eV. Figures b to d show eigenchannels originating in electrode **L** flowing towards the three other electrodes at an energy of −1.5 eV. At this energy, the system exhibits a relatively high total transmission. For the eigenchannel from **L** to **B** (Figure 3.2b) the main part is indeed transmitted to electrode **B**. Similarly, the main part of the eigenchannel calculated from **L** to **T** is transmitted to the latter electrode (Figure 3.2d). On the other hand, the transmission from **L** to **R** is rather low

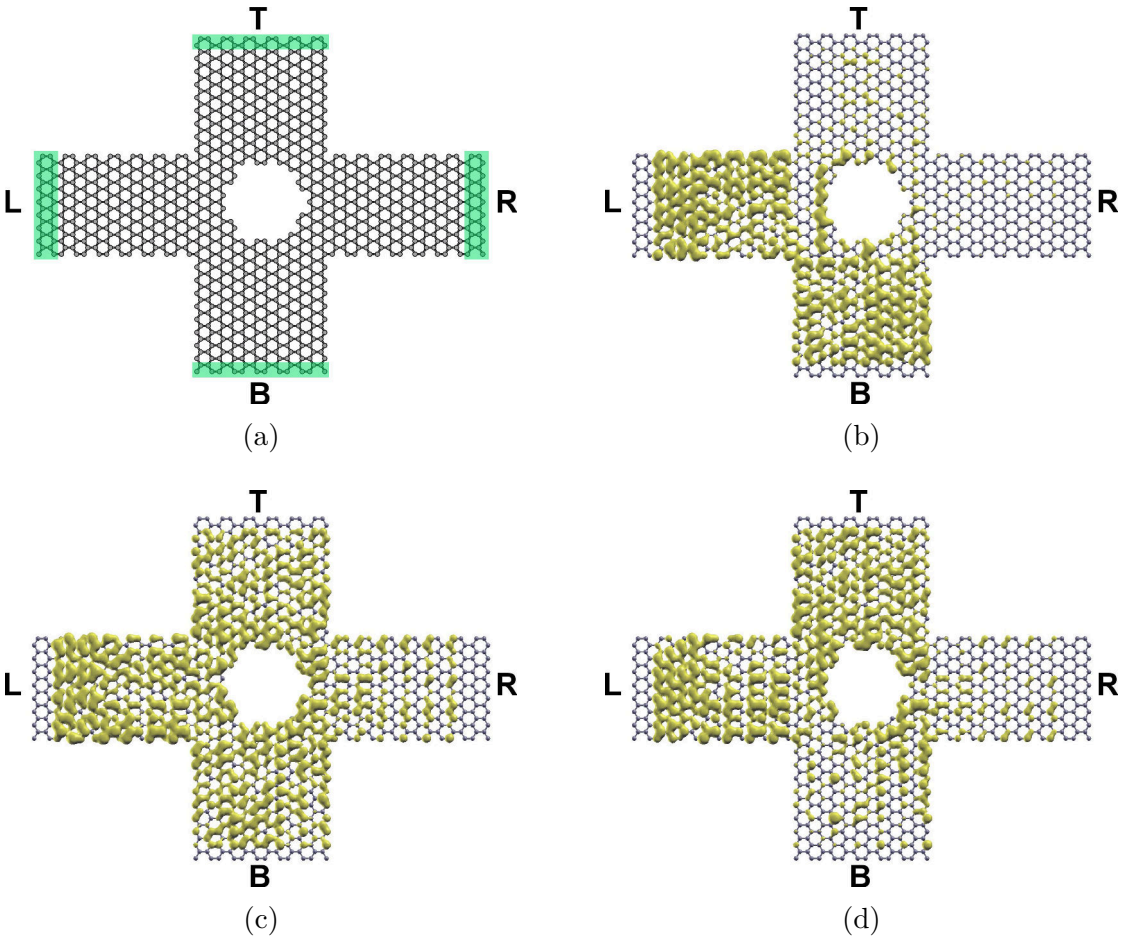

Figure 3.2: (a) Geometry of the test system. Eigenchannels originating from electrode **L** going to electrodes (b) **B**, (c) **R**, and (d) **T** at an energy of −1.5 eV.

at the chosen energy and, thus, most of the eigenchannel gets scattered to other electrodes. Note that, due to a slight asymmetry of the structure (see Figure 3.2a), the eigenchannels are not exactly symmetric.

Our preliminary results demonstrate the value of our multi-terminal eigenchannel tool, which allows to obtain useful and visually distinctive information about the transport properties of a given system. Moreover, it is valid for DFT and tight-binding based Hamiltonians, which opens the doors for investigations of larger systems of realistic sizes.

Chapter 4

Graphene-Metal contacts

Graphene's unique and excellent electronic properties, as well as its small volume, make it an ideal candidate for its use in electronic applications[110, 111]. However, building graphene-based devices often requires the formation of a contact between the carbon allotrope and bulk materials, such as metals[7, 112–115], which will necessarily alter graphene's properties in the interface region[5, 116, 117]. Such modifications might lead to high contact resistances, which are undesirable when envisioning graphene as an interconnect in electronic components. Subsequently, in recent years, huge efforts were put into minimizing the contact resistance of metal-graphene junctions[118–123].

Graphene, or any 2D material for that matter, can be connected to a 3D bulk material in two different ways. The conventional way is to put the 2D substance on top of the bulk material, establishing an area of contact between the two compounds. This interface conformation is called a 2D- or side-contact and is schematically illustrated in Figure 4.1a. On the electronic level, in this arrangement the graphene's π-orbitals overlap and hybridize with the metal's surface orbitals and states. Depending on the strength of the overlap and the hybridization, the modifications range from simple doping (i.e., a shift of the Dirac-point with respect to the metal's Fermi-level) to a complete reconstruction of the Dirac-cone and graphene's band structure around Fermi-level[124, 125]. Systems of this contact type have been studied extensively, but achieving high quality contacts with low resistivity has proven to be rather difficult[126–129].

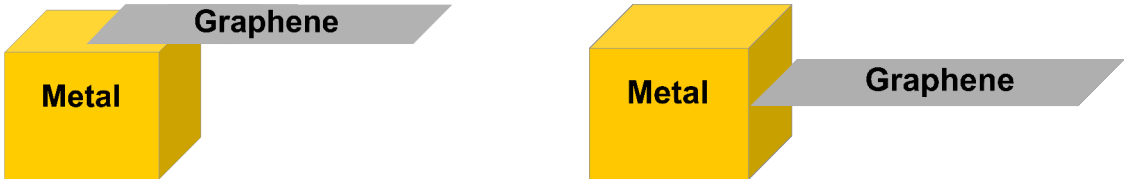

(a) (b)

Figure 4.1: Schematic illustration of side- (a) and edge-contacts (b) of graphene connected to metal.

More recently, an alternative way of contacting graphene to metals has been developed. In the so-called one-dimensional (1D)- or edge-contact geometry, the graphene edge is connected directly to the metallic electrodes, that way forming a 1D metal-graphene junction[130]. In this case, the dangling bonds of the graphene edge atoms can form a covalent bond with the metal atoms. Since the first realization of this type of contact[130], it has been confirmed that this interface geometry leads to substantially lower resistances as compared to the classical side-contact conformation[131–136].

Currently, a major issue of both contacting schemes is the difficulty of obtaining reproducible contact geometries, which leads to significant device-to-device variations in the conductive properties[122, 130, 134, 137, 138]. For example, the first experimental study of metal-graphene edge contacts found values for the contact resistance varying from a few hundred $\Omega\mu m$ for Cr-based contacts to a few $M\Omega\mu m$ for Ni-graphene junctions[130]. However, later experiments produced a contact resistance of Ni-Gr interfaces comparable to the resistance of Cr-Gr junctions[134]. Similar variations in the resistance have been found for side contacted graphene[126, 139, 140]. These variations are often ascribed to different fabrication strategies, which often involve reactive ion or plasma etching. While this treatment is very efficient in exposing graphene edges and removing residues[122, 130, 133, 138, 141], it is yet unclear whether or how the structural and chemical properties of the interface are altered.

Here, we address this issue by a systematic study of 2D and 1D contacts, with special focus on the influence of graphene edge functionalization or contamination.

4.1 Side contacts

Computational details

The setup for the transport calculations, shown in Figure 4.2, is composed of a device region enclosing the metal-graphene interface (red frame), attached to metallic (blue) and graphene (gray) electrodes. The structural relaxations were performed using the device region as indicated in Figure 4.2, with the leftmost metal atoms of each layer, the metal's bottom layer, and the two rightmost carbon rows fixed. For the Ni-based contacts, the structures for the transport calculations consisted of about 200 atoms and 2700 orbitals.

As metal electrodes, we selected Ni and Au. These are known to strongly (Ni) and weakly (Au) interact with graphene, at least in the on-top adsorption conformation[125, 142]. For both metals, we considered the (111) surface contacted to ZZ edged graphene. Besides, it has been demonstrated that graphene ZZ edges can spontaneously form a Stone-Wales reconstruction on Ni surfaces[143]. Thus, for the Ni we also performed calculations with Stone-Wales reconstructed graphene.

We performed the calculations in this section using SIESTA[81] and TranSIESTA[36, 37]. For the exchange-correlation functional we chose the vdW functional by Klimes et al[50]. As basis set we selected a DZP with a PAO.EnergyShift of 0.01 Ry. To efficiently sample the Brillouin zone, we applied a Monkhorst-

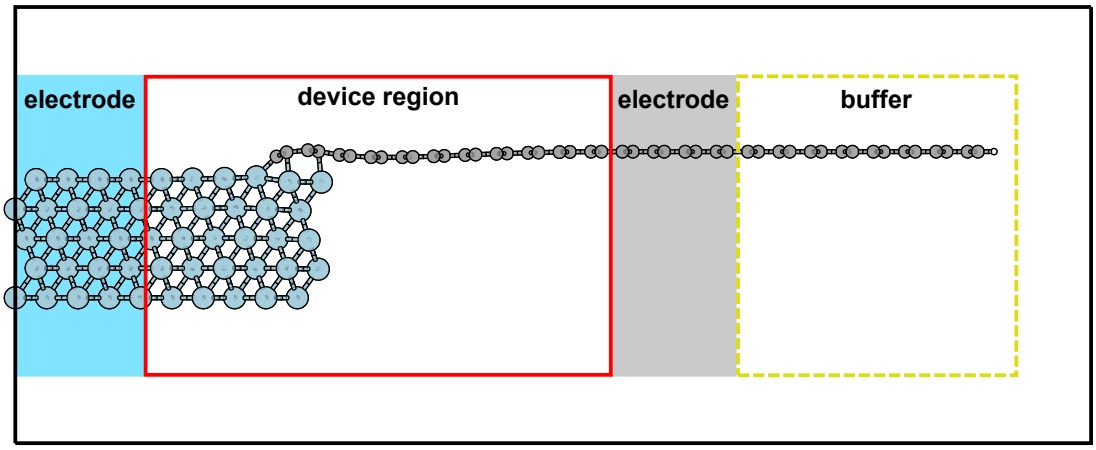

Figure 4.2: Setup for the transport calculations. The black frame indicates the unit cell.

Pack[144] grid of 15x1x1 k-points. For the sampling of the transmission we used 3023x1x1 k-points. We set the convergence criterion for the forces to 0.01 eV/Å for the structural optimizations. As convergence criterion for the self-consistent electronic optimization we used the difference in the Kohn-Sham energy and converged it run until the maximum difference between two consecutive steps was less than 0.0001 eV. We performed all calculations for the 2D contacts spin polarized.

Unpassivated graphene edge

The relaxed structures of the clean Ni and Au based 2D graphene contacts are shown in Figure 4.3. The situation here is different as compared to the above mentioned metal-graphene on-top conformation, in which the metal surfaces only interact with graphene via its π orbitals. In contrast, in the contacts studied here, the dangling bonds of the unpassivated ZZ edge atoms can form a strong covalent connections with both metals. In the case of the Au contact, this leads

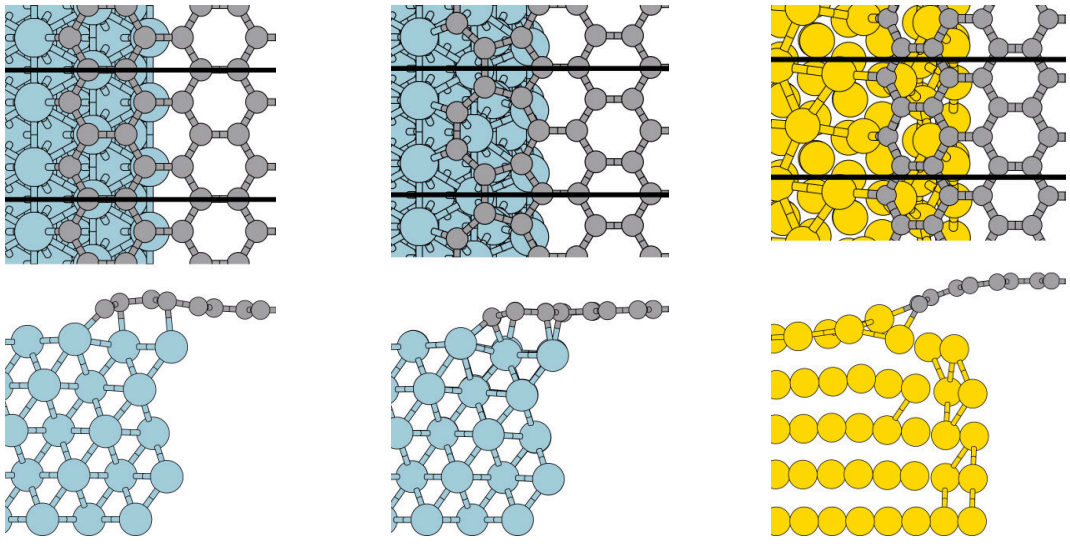

(a) (b) (c)

Figure 4.3: Top and side views of the relaxed structures of the clean 2D metal graphene contacts. (a) Ni(111) in contact with graphene ZZ edge, (b) Ni(111) in contact with Stone-Wales reconstructed edge, and (c) Au(111) in contact with graphene ZZ edge. The black horizontal lines in the top views indicate the unit cell in periodic direction.

to significant structural modifications of the metal slab close to the interface. For the Ni 2D contacts, instead, the structural modifications of the metal slab are significantly weaker.

For these relaxed contacts, we calculated the transmission function and summed up the contributions of both spin channels, yielding the total transmission function $T(E)$. We then obtained the contact resistance R_C from $T(E)$ using the following equation[134],

$$\frac{1}{R_C} = \frac{G_0}{L} \int T(E) \frac{e^{(E-(E_F+eV_G))/k_BT}}{(1+e^{(E-(E_F+eV_G))/k_BT})^2} \frac{dE}{k_BT}, \tag{4.1}$$

where G_0 is the conductance quantum, L is the size of the unit cell in the periodic direction parallel to the interface, E_F is the Fermi-level, T is the temperature and k_B is the Boltzmann constant. The second term in the integral is the derivative of the Fermi-function with respect to the energy and is responsible for thermally broadening the transmission. To include the effect of a gate voltage, the term eV_G is added to the Fermi-level in the exponent of the Fermi-function, with e being the elementary charge and V_G the gate voltage. Thus, the effects of applying a gate voltage are simulated by a rigid shift of the Fermi-level, which is valid only for small values of V_G.

For the non-passivated 2D contacts, the resistance as a function of gate voltage is shown in Figure 4.4a. Albeit the Au 2D contact has the highest contact resistance, all three contacts display values of the same order of magnitude for the whole range of gate voltages. This demonstrates that the unpassivated graphene edge can establish good contacts to both metals. Interestingly, the Stone-Wales reconstructed edge leads to significantly lower contact resistances for negative gate voltages as compared to the unreconstructed ZZ edge. In fact, in this range of gate voltages the unreconstructed egde produces a contact resistance as high as the one for the Au contact. To gain further insight into this matter, we plotted the spin-resolved transmission as a function of energy and k-point in the periodic direction (k_x) for the Ni contacts with ZZ and Stone-Wales reconstructed edges, as shown in Figure 4.4b (similar plots for all the other contacts considered in this section can be found in Appendix A). For both edge types, the transmissions are slightly spin polarized. The 2D contact to the ZZ edge has a higher spin up transmission

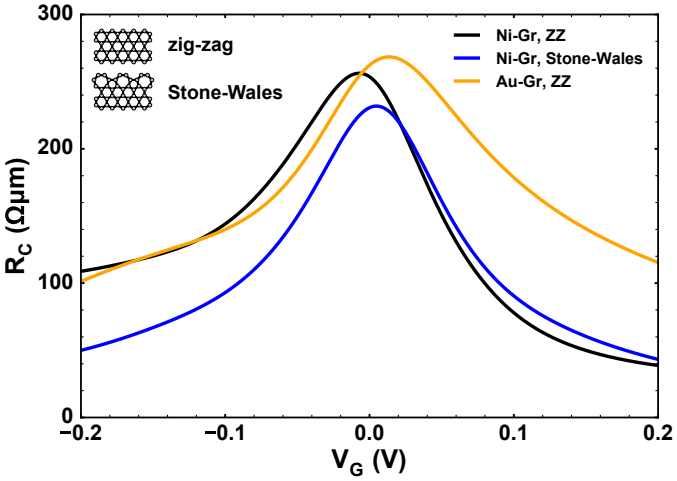

(a)

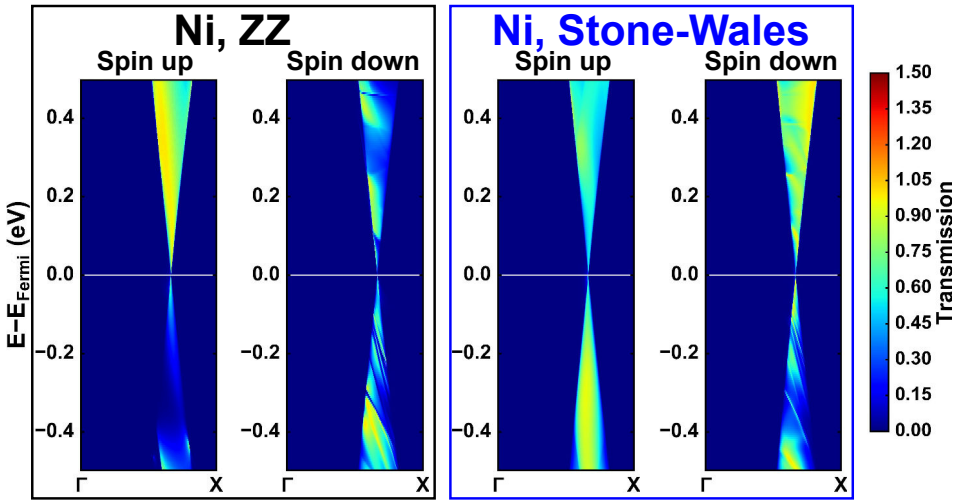

(b)

Figure 4.4: (a) Contact resistance as a function of the gate voltage for the clean contacts. (b) Spin-resolved transmission as function of energy and k_x for the Ni contacts with unreconstructed graphene edge (left, black frame) and Stone-Wales reconstructed edge (right, blue frame).

for positive energies and lower spin up transmission for negative energies, while for the contact to the Stone-Wales reconstructed graphene the opposite is true. Still, the degree of spin-polarization is smaller in the case of the reconstructed edge. Furthermore, for the ZZ terminated graphene contact the transmission of the spin up channel is very low for negative energies, almost vanishing for some

values of k_x. Thus, in this type of contact the spin up channel is effectively blocked for energies below the Fermi-level. This explains the higher contact resistance for negative gate voltages as compared to the contact with the reconstructed edge.

Influence of edge passivation on side contacts

Next, we studied how the passivation of the ZZ graphene edge influences the structural and transport properties of the Ni and Au 2D contacts. We chose three different edge terminations, namely H, NH_2, and OH. The first one is the most common termination of graphene edges, and is used as reference in many theoretical studies of graphene nanostructures (e.g., in Refs. [145–147]), while the latter two have been shown to significantly modify their electronic properties[148].

The relaxed structures of the Ni and Au contacts with the passivated graphene edges are given in Figure 4.5. From the top views in this figure one can see that for the H and OH passivations both graphene edge atoms in the unit cell are functionalized, while the size of NH_2 only allows to passivate one edge atom per unit cell. For the Ni 2D contacts (Figure 4.5a-c), no significant metal surface reconstructions occur and the graphene is only slightly bent. The strongest bending of graphene emerges in the OH terminated contact, where we observe that the OH groups are pushed away from the Ni substrate. The metal graphene separations for all three Ni contacts are very similar (∼1.8 Å), as can be seen from Table 4.1.

The situation is quite different for the passivated Au based 2D contacts (see Figure 4.5d-f). For the functionalized Au contacts, the structural differences with respect to the unpassivated interface (see Figure 4.3c) are quite significant. While

Table 4.1: Metal graphene distances (d_{M-Gr}) for the passivated contacts. This distance was calculated by subtracting the average z-coordinates of the first 6 C rows and of the topmost metal layer. The positions of the passivation atoms are not considered in the distance calculation.

	Passivation		
M	H	NH_2	OH
	d_{M-Gr} (Å)	d_{M-Gr} (Å)	d_{M-Gr} (Å)
Ni	1.77	1.80	1.82
Au	2.59	2.73	2.77

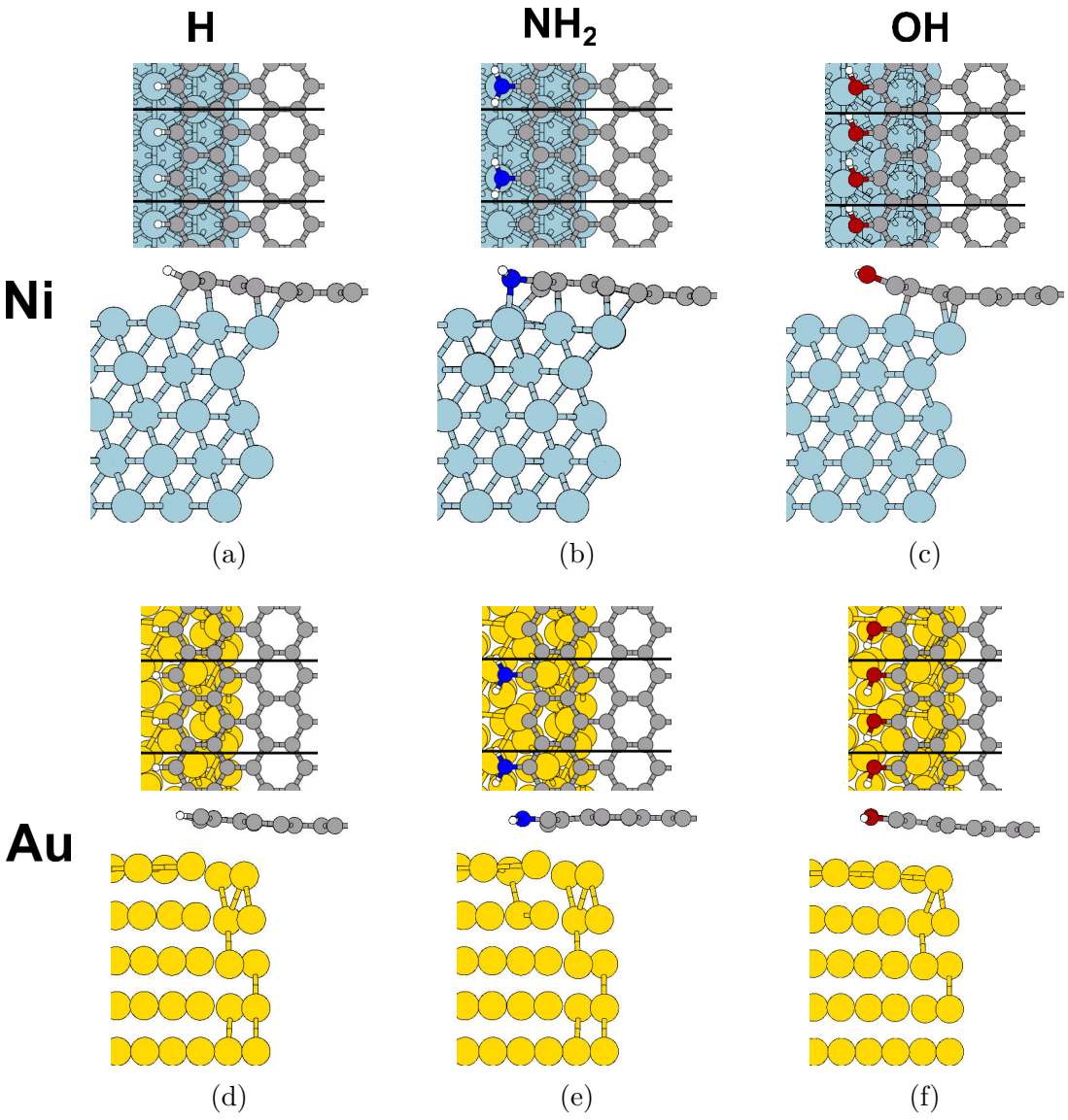

Figure 4.5: Top and side views of the relaxed geometries of edge functionalized 2D metal-graphene contacts. (a)-(c) H, NH_2, and OH passivated Ni contacts. (d)-(f) H, NH_2, and OH passivated Au contacts.

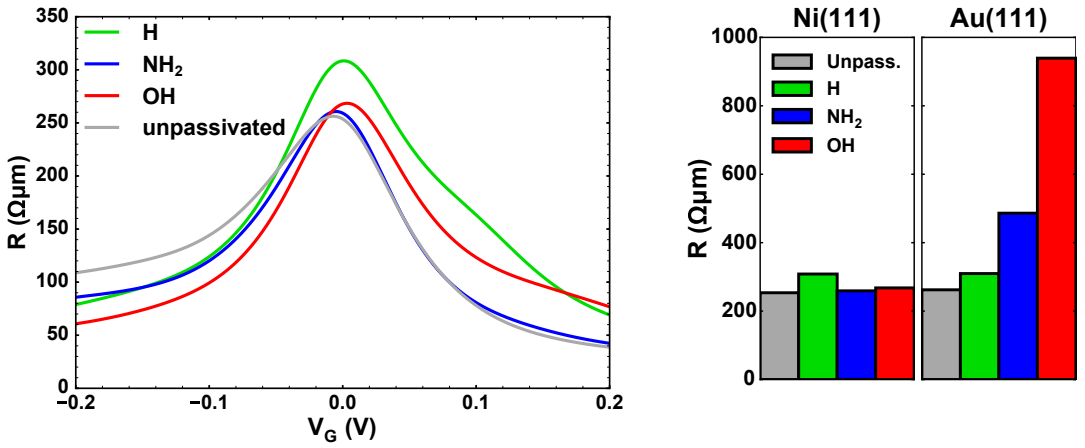

(a) (b)

Figure 4.6: (a) Contact resistance as a function of gate voltage for the passivated Ni-graphene 2D contacts. (b) Contact resistances at zero gate voltage for the Ni and Au contacts.

the unpassivated graphene edge can establish a covalent bond to the Au, edge termination prevents this kind of bonding. Thus, the functionalized graphene only forms vdW bonds to the Au slab. Here, the metal underneath the graphene gets slightly deformed and, besides, the metal graphene distance is lower (∼0.2 Å) for the H terminated contact as compared to the other two (see Table 4.1). Interestingly, even though one of the edge atoms of the NH_2 terminated contacts is unpassivated and could establish a covalent bond to the surface, the metal graphene distance is so large (∼2.73 Å) that no direct C-Au contact is formed. Note that, the average distance between graphene and metal is much larger for the Au contacts than for the Ni graphene interfaces. This indicates that the graphene edge passivated interfaces resemble the on-top conformation scenario, in which Ni interacts stronger with graphene as compared to Au.

Based on these relaxed interfaces, we investigated the influence of the passivation on their transport properties. Figure 4.6a shows the contact resistance as a function of gate voltage for the graphene edge functionalized Ni contacts. The contact resistance is of the same order of magnitude over the whole gate voltage range for all Ni contacts. Interestingly, for negative gate voltages the resistance is slightly smaller for the functionalized contacts than for the unpassivated one,

Table 4.2: spin-filtering efficiency (SFE) as defined in Equation 4.2 for the 2D Ni and Au contacts with edge passivated graphene. The values were obtained for zero gate-voltage.

	Passivation				
Metal	None	H	NH_2	OH	Stone-Wales
	SFE (%)	SFE (%)	SFE (%)	SFE (%)	SFE (%)
Ni	18.4	−44.5	28.9	13.5	−9.0
Au	0.1	0.3	−0.6	−17.1	-

which, at least partially, might be ascribed to spin effects (see Appendix A).

The resistance values at zero gate voltage for the Ni and Au contacts are shown in Figure 4.6b. For the Au contacts, passivation of the graphene edge increases the resistance in all cases. This increase is strongest for the OH passivated contact, and also for the contact with the NH_2 functionalized graphene edge it is quite significant. Passivating the graphene edge with H, on the other hand, does only lead to a slight increase in resistance. The clean and H passivated Au contacts assume values for the resistances which are very close to the values of their Ni counterparts.

In order to quantify the spin-filtering character of the different contacts, we estimated the spin-filtering efficiency (SFE) according to the following equation,

$$SFE = \frac{(G\uparrow - G\downarrow)}{(G\uparrow + G\downarrow)}, \tag{4.2}$$

where $G\uparrow$ and $G\downarrow$ represent the conductances for the spin-up and spin-down channels at a temperature of 300 K, respectively. With this definition the SFE assumes positive (negative) values if the spin-up channel conductance is higher (lower) than the conductance through the spin-down channel.

Table 4.2 lists the values for the SFE of the different Ni and Au 2D contacts to graphene. The Ni contacts offer a wide spread of SFE values, with the Stone-Wales reconstructed edge offering the lowest and the H functionalized graphene the highest SFE magnitude. In the case of the Au contacts, only functionalization of the graphene edge with OH leads to a non-negligible SFE. All in all, we can conclude that spin-filtering is rather low in these metal-graphene side contacts.

In summary, our preliminary results show how the contact resistances of 2D metal-graphene contacts depends on the metal and the graphene edge functionalization. These results indicate that the differences between the metals are rather small when the graphene edge is unpassivated, but that edge termination can have a significant influence on the conduction properties of such interfaces.

4.2 Edge contacts

Calculation details

The setup for our transport calculations of the metal graphene edge contacts is illustrated in Figure 4.7. The device region consists of 5 metal layers and 40 C rows of graphene. Except for the two bottom layers of the metals, all of the atoms in the device region were relaxed.

Since the metal electrodes used in the fabrication of metal-graphene edge contacts are not perfectly crystalline and, hence, are hard to simulate, we have chosen to consider only a single crystalline orientation per metal. This approach allows us to focus on trends and permits the comparison between different systems. We chose the surface planes for the metals to be 111 for Ni and Au, 110 for Cr, and 0001 for Ti, some of which were already used in previous theoretical studies (e.g., in Refs. [130, 134, 149, 150]).

Our strategy to find contact geometries involved calculating the interaction energy curves, and then relaxing the atoms of the device region (except the two

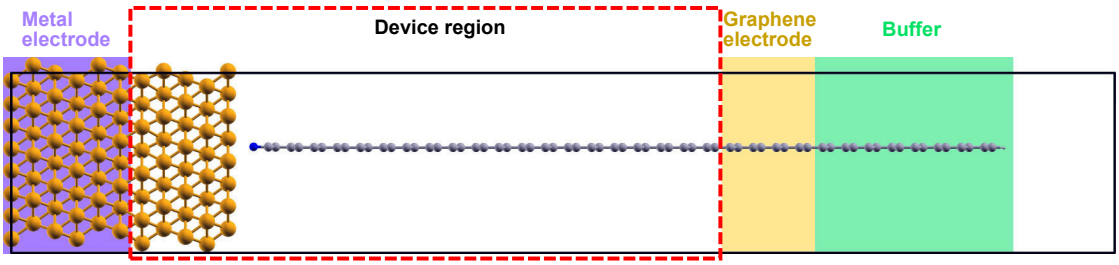

Figure 4.7: Setup for transport calculations of metal-graphene edge contacts with metal electrode (blueish) and graphene electrode (yellow) attached to the device region. The black frame indicates the unit cell used in the calculations.

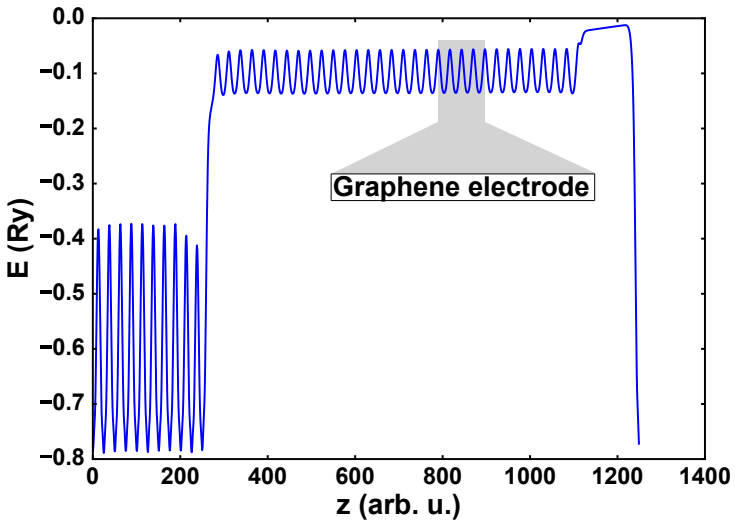

Figure 4.8: Electrostatic potential of clean NiGr contact. The shaded gray area indicates the position of the graphene electrode.

bottom metal layers), as it will be described in more detail below. More realistic structures might be obtained by applying modern stochastic approaches[151, 152]. However, these methods are rather new and only have been applied to interfaces between systems having the same dimensionality (e.g., 2D interfaces between two 3D materials). Using stochastic approaches to obtain contact conformations of metal-graphene edge contacts would first require to verify that they also work for interfaces between metals with mixed dimensionality and, additionally, implementing and testing such an algorithm is a huge task and lies outside of the scope of this work.

For the transport calculations we added a 6 metal layer electrode on the one side and a 8 C row long graphene electrode on the other side, as can be seen from Figure 4.7. Additionally, we used 16 C rows of graphene as buffer atoms. We chose this asymmetric setup in order to avoid spurious effects emerging from the decay of the electrostatic potential of the electrode, as studied in Ref. [117]. To check that our setup is indeed free of such effects, in Figure 4.8 we have plotted the average electrostatic potential in the transport direction (z) for one representative case, namely the clean Ni-Gr contact. Here, the gray shaded area corresponds to the potential at the position of the graphene electrode. Clearly, the potential is sufficiently flat, and, hence, well converged in the region of the graphene electrode.

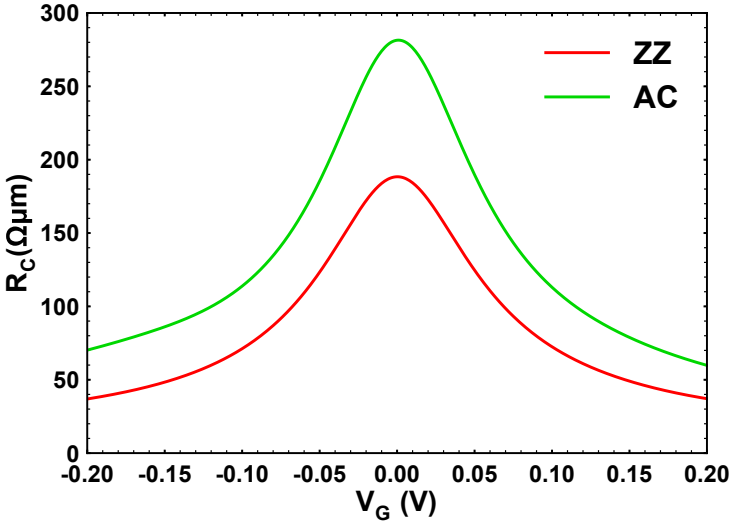

Figure 4.9: Contact resistance as a function of gate voltage for clean Ni-Gr contacts with ZZ or AC graphene edge.

We performed all the calculations described in this section using the PBE[53] flavor of the GGA for the approximation of the exchange-correlation functional. For the SIESTA[81] and TranSIESTA[36, 37] calculations we used a DZP basis set and a mesh cut-off of 400 Ry. To efficiently sample the Brillouin zone, we applied a Monkhorst-Pack[144] grid of 23x3x1 k-points. For the sampling of the transmission we used 765x5x1 k-points. For the structural optimizations, we set the convergence criterion for the forces to 0.01 eV/Å. As convergence criterion for the self-consistent electronic optimization we used the difference in the elements of the Hamiltonian matrix and converged it until the maximum difference between two consecutive steps was less than 0.0001 Ry. We carried out all the calculations for the 1D contacts spin polarized.

With the aim of elucidating the influence of the graphene edge morphology on the transport properties, we compare the ZZ and AC edge conformations for the clean Ni-Gr contact. For the AC terminated graphene, we applied the same procedure as for the ZZ edge conformation to obtain the corresponding relaxed structure. This procedure includes relaxation of the metal and graphene at a large separation, calculating interaction energy curve, and, finally, relaxing the system to its equilibrium configuration. The corresponding resistance of these two edge contacts as a function of gate voltage (calculated according to Equation 4.1) is

given in Figure 4.9. The contact resistance is slightly larger for the AC than for the ZZ edge, but it is of the same order of magnitude over the whole range of gate voltages. Although the situation might be different in the case of contaminated graphene edges, considering only ZZ graphene for uncontaminated and chemically modified contacts allows us to directly compare different contacts to the same metal. For this reason, we have chosen to consider only zig-zag edge graphene both for uncontaminated and chemically modified cases.

Edge contamination of zig-zag graphene nanoribbons

Before performing transport calculations for metal-graphene edge contacts, we carried out a detailed energetics analysis of the possible graphene edge contaminations. With this aim, we calculated the stability of different graphene edge contaminations using a 10-atom wide ZZ nanoribbon, functionalized with F, F_2, O, and O_2. These contaminants were chosen because fluorine and oxygen are often contained in the reactive compounds used to etch the graphene prior to contact formation (for a detailed description of the production of graphene-metal edge contacts see Ref. [130]).

We performed the calculations of the binding energies of different contaminants at the graphene ZZ edge with VASP[76–79]. Here, we used a plane wave cut-off energy of 300 eV and an energy convergence criterion of 1×10^{-6} eV. We performed the stabillity calculations using a plane wave based method to avoid basis set superposition errors known to occur in electronic structure methods based on the use of localized basis sets (e.g., in SIESTA[81]).

The formation energy E_F for the different edge terminations was obtained using the following formula,

$$E_F = E_{X-Gr-X} - (E_{Gr} + n_X \frac{E_{F2/O2}}{2}) \quad with \quad X \in \{F, F_2, O, O_2\}. \tag{4.3}$$

In this equation, E_{X-Gr-X} is the energy of the passivated ribbon, E_{Gr} denotes the energy of the unpassivated ribbon, and $E_{F2/O2}$ represents the energy of F_2 and O_2, respectively. n_X is the number of contaminant atoms per edge, i.e., 1 for F and O, and 2 for F_2 or O_2 passivated systems. The corresponding results are summarized

Table 4.3: Formation energies for different graphene edge contaminations.

Contaminant	E_F (eV)
F	−8.7
F_2	−12.3
O	−7.2
O_2	−4.1

in Table 4.3. Clearly, passivation with F_2 (E_F=−12.3 eV) is more stable than passivation with a single fluorine atom (E_F=−8.7 eV), in good agreement with previously reported values (see Ref. [153]). In the case of oxygen, on the other hand, we find that single atom passivation (E_F=−7.2 eV) is more stable than attaching two O atoms to the edge (E_F=−4.1 eV). Based on these results, we decided to consider the most stable contamination, F_2, as well as F and O, which also exhibit rather large formation energies.

Structural optimizations

Energetics of metal-graphene contacts

In order to get insight into the energetics and stability of the metal-graphene edge contacts, we calculated the interaction energy as a function of the separation distance between the metal slab and the graphene sheet. First, we relaxed the graphene and the metal slab at a large distance where the interaction energy is close to zero. Then, we calculated the change in the total energy of the systems as a function of the metal-graphene separation, keeping the geometries of both subsystems (metal and graphene) frozen. From the resulting interaction energy curves, we determined the distance of minimum energy (d_{Emin}), which corresponds to the minimum of the interaction energy curve, and the distance of maximum force (d_{Fmax}), i.e., the distance at which the second derivative of the interaction energy curve vanishes.

As an example, Figure 4.10 shows the interaction energy curve for the Cr-Gr contacts. In this plot, the green and red lines indicate the distances of minimum energy (d_{Emin}) and maximum attraction (d_{Fmax}), respectively, between the metal and graphene. From this figure, we conclude that the distances of minimum energy

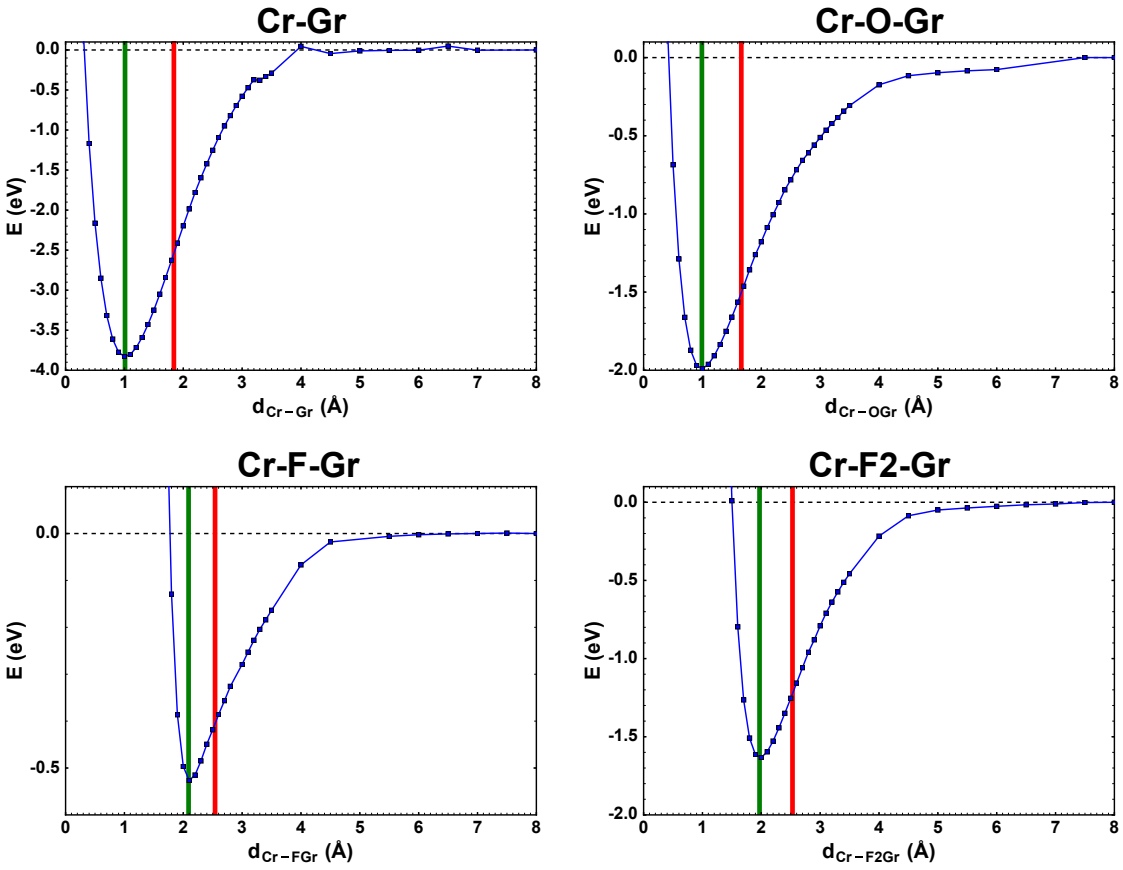

Figure 4.10: Energy versus distance curves for the clean (top-left), O (top-right), F (bottom-left), and F_2 (bottom-right) contaminated Cr-Gr contacts. The green and red lines indicate the distances of minimum energy and maximum force, respectively.

and maximum force for the clean and O passivated contacts are almost the same. Similarly, the contamination with F or F_2 leads to comparable distances.

Likewise, we have calculated d_{Emin} and d_{Fmax} for the other three metals (Ni, Ti, Au) considered in this work. The results are given in Table 4.4, where we clearly observe that, for the transition metals (Cr, Ni, Ti), oxygen contamination yields d_{Emin} and d_{Fmax} values close to the corresponding distance of the clean contacts. Both fluorine based contaminations result in a significantly increased separation of the metal and graphene compared to the clean and O passivated contacts. This can be attributed to the fact that, the edge atoms of the clean and O contaminated edges can form strong covalent bonds to the metal, while F is

Table 4.4: Distances between metal (M) and graphene (clean contacts), or between metal and contaminant atom(s) as estimated from the interaction energy curves shown in Figure 4.10 for Cr-based contacts. For clarity, the schemes indicate how the distances are measured for the clean (left) and contaminated (right) contacts.

	Contamination							
M	Clean		F		F2		O	
	d_{Emin} (Å)	d_{Fmax} (Å)	d_{Emin} (Å)	d_{Fmax} (Å)	d_{Emin} (Å)	d_{Fmax} (Å)	d_{Emin} (Å)	d_{Fmax} (Å)
Cr	1.02	1.84	2.09	2.54	1.97	2.53	0.99	1.66
Ni	1.48	2.08	2.41	3.33	2.21	2.72	1.53	2.02
Ti	1.79	2.44	2.25	3.74	2.17	2.84	1.67	2.40
Au	1.98	2.90	2.47	2.93	2.43	2.84		

only able to form one bond (in this case to graphene) and, thus, the connection of F contaminated edges to the metal is rather weak. Besides, in the case of Au, the distances of minimum energy increase significantly upon fluorination, while the distance of maximum attraction remains almost unchanged.

Forces on interface atoms

With the aim of addressing the atomic scale reactivity of the metal-graphene 1D contacts, we examined the forces induced by the metal at the graphene edge at the distance of maximum attraction. First, we focus on Cr, which is the experimentally most frequently employed metallic electrode. For this metal, we investigated the changes in the interface forces depending on the termination of the graphene sheet. We focused on the force component perpendicular to the surface (z-component).

The forces in z-direction (F_z) induced by the Cr(111) surface onto the interface carbon and contaminant atoms are shown in Figure 4.11. For comparison purposes, the forces (and the arrows indicating the force on the first graphene or contaminant atom) are normalized with respect to the values of the clean contact (Figure 4.11a). Blue and red shades indicate forces pointing towards (negative forces) and away

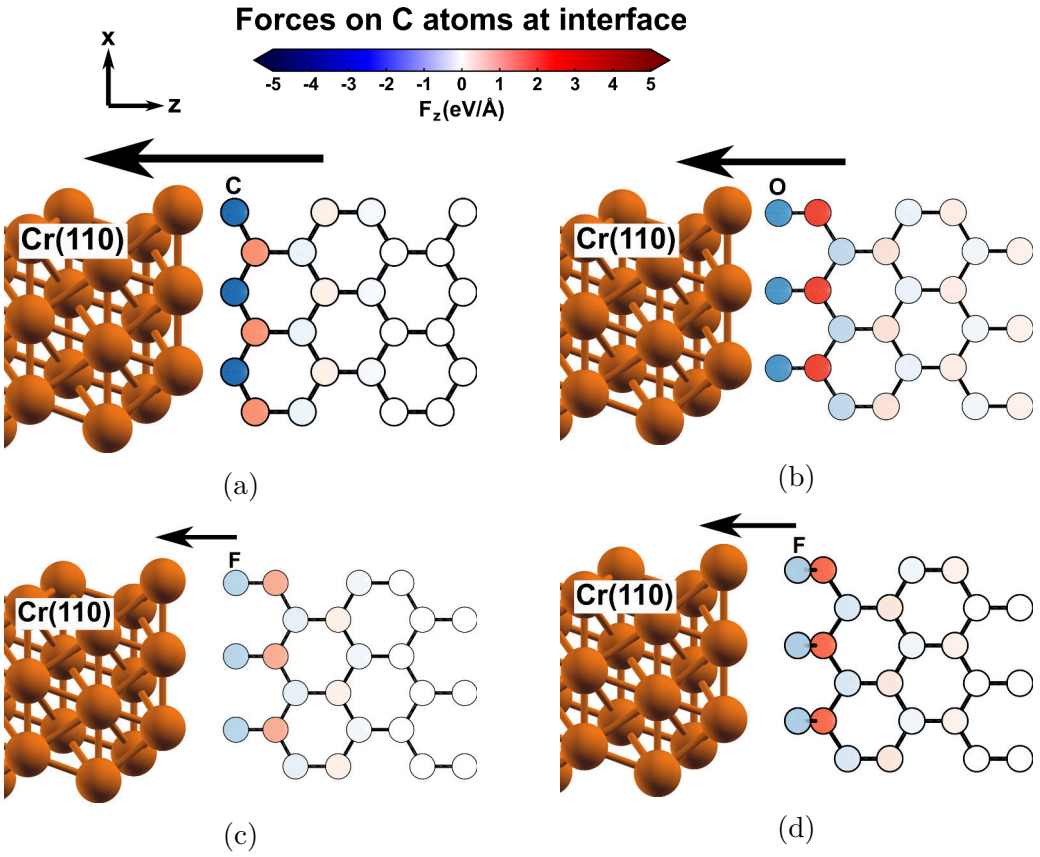

Figure 4.11: Forces on the interface atoms for (a) clean, (b) O, (c) F, and (d) F_2 contaminated Cr-Gr contatcs in the maximum force conformation.

(positive forces) from the surface, respectively. We find that the net forces on the edge atoms of the clean and O contaminated contacts are high and pointing towards the surface. The forces on the F atoms of both fluorinated contacts, despite also pointing towards the metal, are much smaller as for the clean contact. This is a consequence of the larger metal-graphene separation for the fluorinated contacts, which in turn is a result of their bonding chemistry. That is, since F can only establish one bond, it is well bonded to the graphene edge, but lacks the possibility of connecting to the metal.

Next, in order to inspect the impact of using different metals, we have looked at the forces on the interface atoms for three Ni based contacts, namely the clean, O and F contaminated contacts (shown in Figure 4.12). For comparison, also the forces on the fluorine passivated Cr-based contact is depicted. As for the Cr-Gr

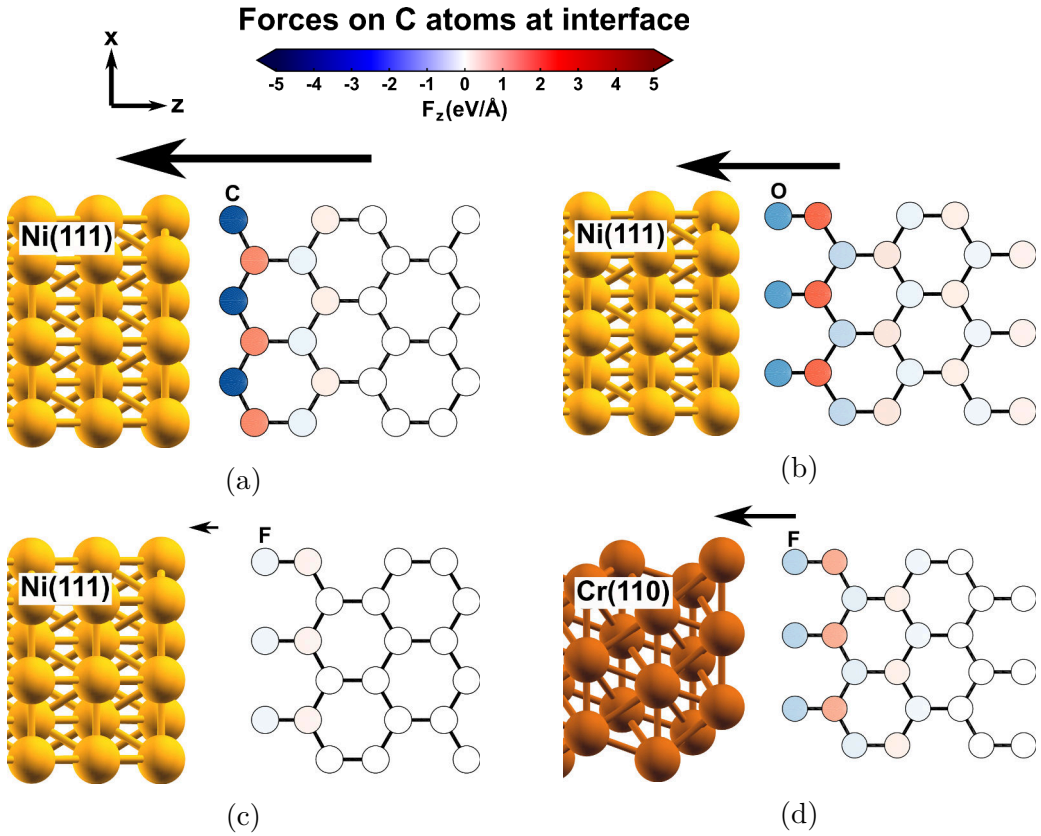

Figure 4.12: Forces on the interface atoms for (a) clean, (b) O, and (c) F contaminated Ni-Gr contatcs as well as the F passivated Cr-Gr contact (d) in the maximum force conformation.

interfaces, the forces on the clean and O passivated edges are quite high. For both metals, one can see that the forces for the O contaminated contact decay slower than for the other contacts, i.e., even carbon atoms further away from the interface contribute to the net force. On the contrary, for the mono-fluorinated Ni-Gr junction, the forces on the edge atoms are almost vanishing. Thus, for this type of contamination, the Cr exerts a much higher attractive force on the interface compared to Ni.

Therefore, our calculations reveal a complex scenario that might be at the origin of the experimental differences. For example, the significantly different forces on the edge atoms between Cr and Ni based mono-fluorinated contacts, in combination with different graphene-metal separations (see previous subsection),

indicate that the metal might be the main factor for the dynamics of these particular contacts. On the other hand, the influence of the metal on the forces in the O contaminated interfaces extends further towards the graphene layer, as compared to all other passivations, which suggests that oxygen might increase the reactivity at graphene metal interfaces. From these results, we can conclude that the reactivity at the interfaces depends, in an intricate way, both on the metal and the graphene edge contamination.

Evolution of contacts upon formation

In the following, the structural evolution of the interfaces upon contact formation is investigated. For this purpose, we relaxed the systems starting from the E_{min} and F_{max} conformations, as previously obtained (above). The final graphene-metal separations obtained from these relaxations are given in Table 4.5. For almost all contacts, the final metal-graphene distances are virtually the same, independent of whether the relaxation was started at distance of minimum energy (d_{Emin}) or at distance of maximum force (d_{Fmax}). The exceptions are the fluorinated Ni-Gr and Ti-Gr contacts. As shown above, the force on the graphene edge of the monofluorinated Ni-Gr contact at d_{Fmax} is very small and the metal-graphene separation rather large. As a consequence, the Ni is not able to pull the graphene sheet much

Table 4.5: Distances between metal (M) and graphene (clean contacts), or between metal and adsorption atom(s) (contaminated contacts) after performing structural optimizations starting at the distances of minimum energy (d_{Emin}) and maximum force (d_{Fmax}) For clarity, for systems with significantly different d_{Emin} and d_{Fmax} the distances are written in bold characters.

	Contamination							
M	Clean		F		F2		O	
	d_{Emin} (Å)	d_{Fmax} (Å)	d_{Emin} (Å)	d_{Fmax} (Å)	d_{Emin} (Å)	d_{Fmax} (Å)	d_{Emin} (Å)	d_{Fmax} (Å)
Ni	1.47	1.48	**2.39**	**2.92**	2.22	2.31	1.47	1.47
Cr	0.87	0.86	2.15	2.14	2.01	2.02	0.90	0.90
Ti	1.29	1.25	**2.36**	**3.76**	**3.60**	**2.16**	1.25	1.25
Au	1.87	1.89	2.52	2.51	2.33	2.40		

closer to it when relaxing the structure starting from the distance of maximum force. Hence, relaxing this contact from d_{Fmax} leads to a metal-graphene distance significantly larger than when the structural optimization starts from d_{Emin}. The same is true for the mono-fluorinated Ti-Gr contact.

In the case of the initially di-fluorinated Ni-Gr contact, the contacts relaxed at d_{Emin} and d_{Fmax} end up basically in the same conformation: one of the F atoms gets stripped away from the graphene edge and bonds to the metal. Thus, the initially di-fluorinated graphene edge ends up being mono-fluorinated after the relaxation. In fact, the same is true for the initially di-fluorinated Cr-Gr contact. Here, as well, the metal is able to strip away one of the F atoms of the graphene-edge. In section 4.2, we have shown in accordance with literature[153], that for a free-standing graphene ZZ edge the di-fluorinated passivation is more stable than the mono-fluorinated one. Clearly, the presence of the metals drastically decreases the stability of di-fluorinated edge contamination and, consequently, leads solely to relaxed geometries with mono-fluorinated graphene edge contaminations.

Remarkably, the situation is quite different for the initially di-fluorinated Ti-Gr contact, as can be seen in Figure 4.13. When this system is relaxed starting from d_{Emin}, the metal is able to strip away both fluorine atoms. The two F atoms then

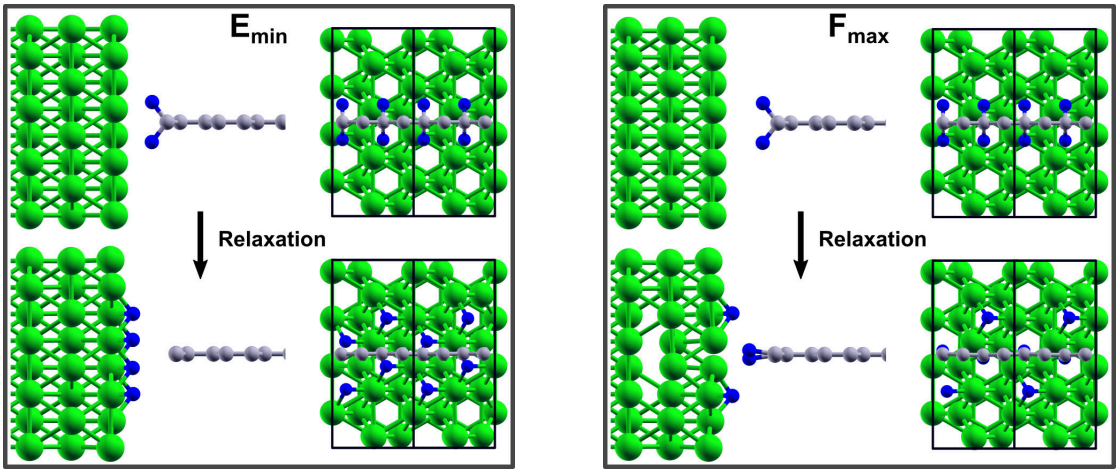

(a) (b)

Figure 4.13: Initial and final structures of the Ti-F_2-Gr contact at (a) d_{Emin} and (b) d_{Fmax}.

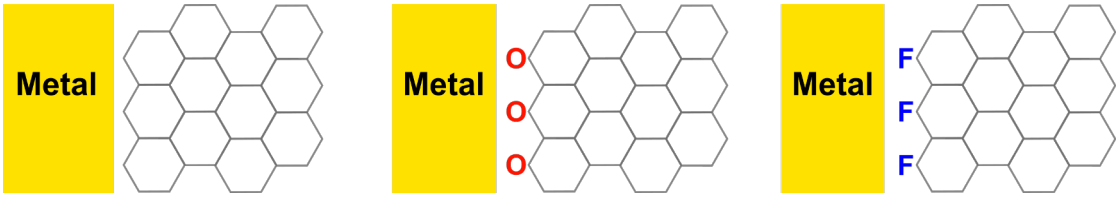

Figure 4.14: Scheme of final contaminations after structural optimizations.

bond to the metal and form a layer on the surface, thus, effectively increasing the distance between graphene and metal, and preventing the formation of covalent bonding between the graphene edge and Ti. On the other hand, when starting the relaxation of this contact is started at d_{Fmax}, Ti can only strip away one of the F atoms. These results for the Ti-F_2-Gr contacts point towards a very complex energy landscape with multiple conformational states.

All in all, regardless of the metallic electrode, the final graphene edge conformation always falls into one of three categories, namely clean, mono-fluorinated, or mono-oxidized, as schematically illustrated in Figure 4.14.

Resistance of clean and contaminated contacts

After having determined the structure and chemical conformation of the 1D contacts, we now turn our attention to their conductance properties. For this purpose, the resistances of the different graphene based 1D contacts have been calculated (Equation 4.1) and analyzed .

The contact resistance as a function of gate voltage for the clean contacts is shown in Figure 4.15a. Over the whole gate voltage range, the contact resistances are of the same order of magnitude for all clean contacts. The Ni-Gr interface exhibits a slightly lower contact resistance than the other contacts. In fact, comparison to the intrinsic resistance of graphene shows that the contact resistance of the Ni-Gr junction is close to the theoretical lower limit. Interestingly, the Ti-Gr junction exhibits the largest contact resistance, its performance being even worse than for the more inert Au electrode. The poor electronic transmission across the Ti-Gr interface might be ascribed to a mismatch between the Fermi-level states of the metal and those of the graphene, as it has been reported to occur for epitaxial graphene on Ti[154].

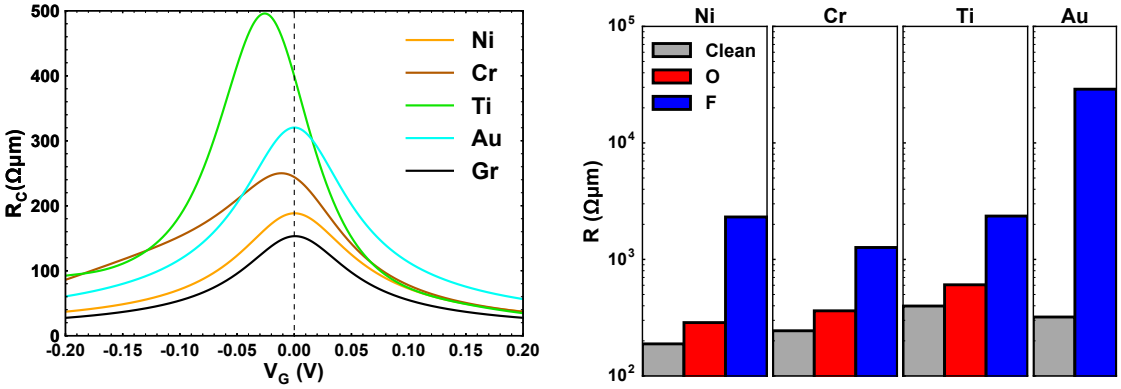

(a) (b)

Figure 4.15: (a) Contact resistance as a function of gate voltage for the clean Ni-Gr, Cr-Gr, Ti-Gr, and Au-Gr junctions. As reference the intrinsic graphene resistance is plotted as well (black line). (b) Contact resistances at V_G=0 V for clean (grey), O (red) and F (blue) contaminated Ni-Gr, Cr-Gr, Ti-Gr, and Au-Gr contacts.

Therefore, our calculations for clean metal-graphene edge-contacts cannot explain the device-to-device variations observed in experiments. Motivated by this, we also calculated the contact resistance at zero gate voltage for the relaxed clean, F, and O contaminated contacts. The results of these calculations are shown in the form of histograms in Figure 4.15b. Clearly, the increase of the contact resistance is rather small for the O contaminated junctions, independently of the metal. Passivating the graphene edge with F, on the other hand, significantly increases the contact resistance for all metals. It is worth emphasizing that the relative increase is substantially smaller for the Cr-based contact.

From these results we can infer that contamination of the graphene edge can have a significant influence on the quality of metal-graphene edge contacts. Still, quantitative comparison with experiments is difficult, because the exact conformation of the fabricated contacts is unknown. While the contacts in our calculations are highly idealized (e.g., crystalline metal, straight graphene edges), experimental contacts will deviate from these ideal interfaces in various ways, for example, contamination will most likely not be uniform and structural defects are expected.

A schematic illustration of a non-ideal contact conformation is shown in Figure 4.16. In this model, we define three different distances. Namely, equilibrium distance (d^1), distance at maximum force (d^2), and distance of maximum force plus 1 Å (d^3). Using this model as a reference, and taking Cr and Ni as representative metals, we carried out transport calculations at each distance and for the different graphene contaminations (clean, oxidized, mono or di-fluorinated). The realistic contact conformation can be viewed as a combination of the different simulated scenarios. Thus, from the calculations reported in the following, we can extract a range of values for the resistance of the model contact.

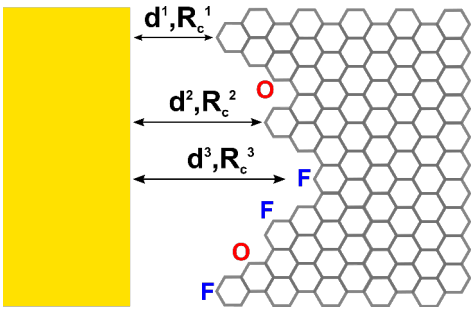

Figure 4.16: Schematic illustration of a possible, non-ideal, contact conformation.

The contact resistances at different distances for the Ni-based interfaces are shown in Figure 4.17a. Comparing the contact resistance at the distance of maximum force d^2 to the values obtained at d^1, we observe only a small increase for the clean and O passivated Ni-Gr contacts, with R_C values within the same or-

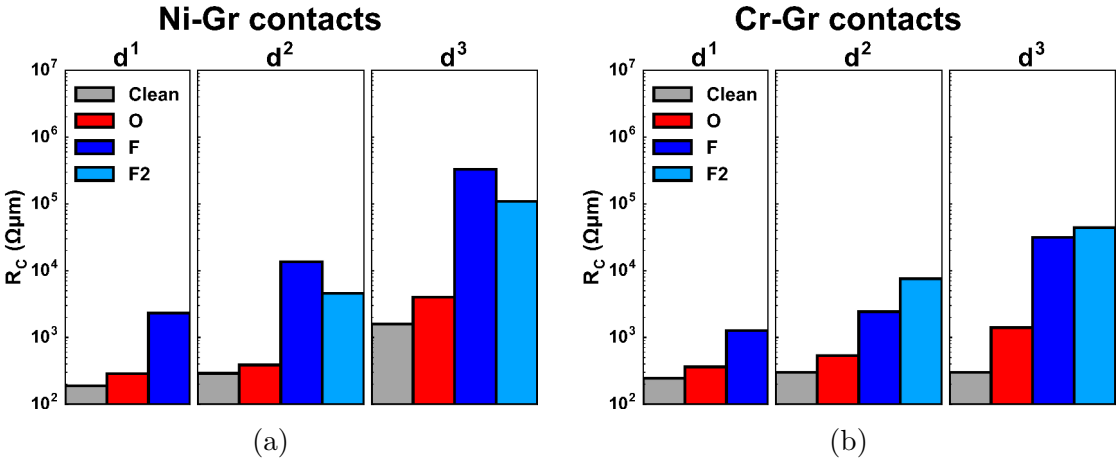

(a) (b)

Figure 4.17: Contact resistances at V_G=0 V for clean (grey), O (red) and F (blue) contaminated Ni-Gr (a), and Cr-Gr (b) contacts at equilibrium distance (d^1), at distance of maximum force (d^2), and at distance of maximum force+1 Å (d^3).

der of magnitude. At distance d^3, instead, the contact resistance of the clean and oxygen contaminated Ni-Gr junctions increases by an order of magnitude. For the mono-fluorinated case, the contact resistances are elevated by an order of magnitude already when going from d^1 to d^2, and by another order of magnitude when extending the distance from d^2 to d^3. Interestingly, while showing the same trend as the mono-fluorinated contacts, the contact resistance of the di-fluorinated junctions is always smaller than for the mono-fluorinated contacts in the case of Ni-based interfaces at all distances.

For the Cr-based contacts the situation is rather different (see Figure 4.17b): for the clean Cr-Gr interface, the resistance is very similar regardless of the separation distance. We ascribe this behavior to the relatively short bond distance between Cr and graphene at all distances. For the O contaminated Cr-Gr junction, the resistance increases upon moving the graphene further away; yet, the relative increment is smaller than in the corresponding Ni-based interface. On the other hand, for the Cr-F-Gr contacts, the change in resistance is only of one order of magnitude when going from d^1 to d^3, with only a small upshift at d^2 as compared to d^1. The contact resistance of the Cr-F_2-Gr contacts is at all distances only slightly larger compared to the Cr-F-Gr interface.

Summarizing, the relative increase in the contact resistance upon contamination is lower for Cr than for Ni based 1D interfaces. This means that the quality of the Cr based contacts is less dampened by contamination. As a result, Cr is a better candidate to obtain 1D contacts with lower resistance, which agrees with experimental observations[130]. In any case, as already mentioned above, a quantitative comparison to experiments is difficult due to a lack of atomic-scale information about the fabricated contacts (e.g., edge reconstructions, distribution of contaminants, etc.). Nevertheless, our qualitative study of the influence of contamination on the contact resistance of metal graphene edge contacts provides valuable insight into the mechanisms responsible for device-to-device variations. Moreover, it can guide the future design of metal-graphene contacts of better quality.

Spin filtering properties

Finally, we turn our attention to possible spin effects in the 1D contacts. As it is known, graphene ZZ edges posses a spin-polarized edge state[155–158]. Therefore, to shed light on the possible spin-filtering effects, we investigate how the proximity of the metal electrode affects the spin-polarization of the graphene edges in our contacts.

For this purpose, we first take a look at the spin-resolved projected density of states (PDOS) of the graphene edge atoms of the mono-fluorinated Cr an Ni contacts. Figure 4.18a depicts the DOS at distances d^1, d^2, and d^3 projected onto the first C row (grey) and on the F adatom (blue) for the Cr-F-Gr contact. Corresponding plots for the Ni-F-Gr contact are shown in Figure 4.18b. For comparison, the DOS projected onto the edge C atoms of a free-standing ZZ graphene edge (black) is shown in the lower panels. For the Cr-based junction at the equilibrium distance (d^1), the spin up and spin down PDOS corresponding to the C edge atoms are essentially equal (in energy position and intensity). The situation is qualitatively the same for the DOS projected onto the F atom. This clearly indicates quenching of the spin-polarization at the ZZ edge. Apart from slight shifts of the peaks compared to the free-standing ZZ edge, moving the graphene sheet further away from the metal (d^2 and d^3) gradually restores the spin-polarization. In contrast, despite small energy shifts, the ZZ edge in the Ni-F-Gr junction remains spin-polarized even at d^1. In fact, already at distance of maximum force (d^2) the spin-polarization is almost completely restored.

In the attempt to quantify these spin effects, we calculated the spin-filtering efficiency (SFE) as defined in Equation 4.2. The values for the SFE of different edge contacts are listed in Table 4.6 on page 64. In the case of Cr, at equilibrium distance (d^1) both, clean and contaminated, contacts display a very low spin-filtering capacity. Moving the graphene further away from the metal increases the corresponding SFE, although the magnitude of the increase depends very delicately on the contamination of the graphene edge. The rather small increment of the SFE for the clean interface can be attributed to the low distance, and thus, good contact, between the Cr and graphene even at d^2 and d^3 (see Table 4.4). In case of the mono-fluorinated and O passivated Cr-Gr contacts, instead, the SFE significantly

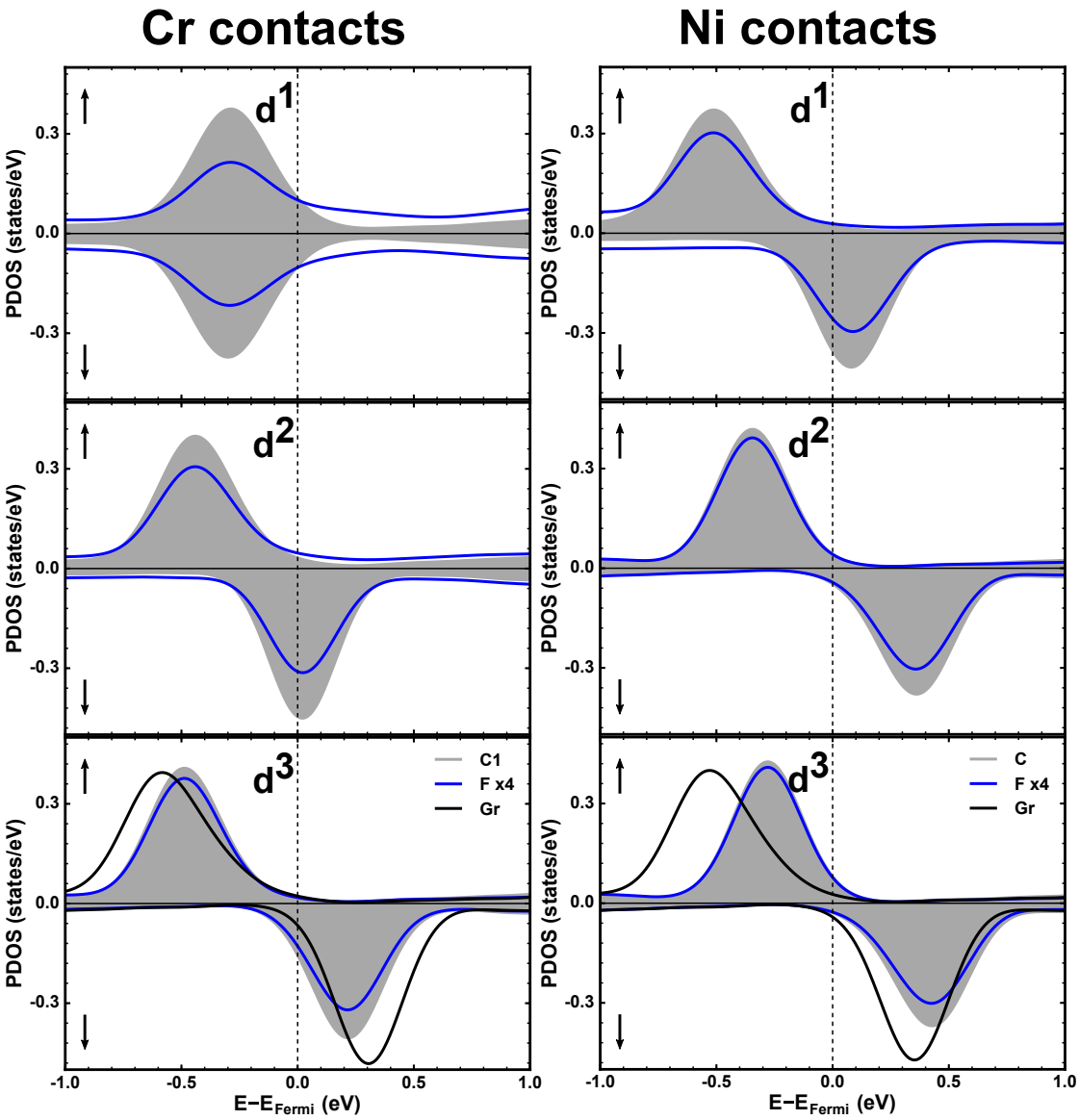

(a) (b)

Figure 4.18: PDOS of the interface atoms of a Cr-F-Gr (a) and a Ni-F-Gr (b) contact calculated for spin-up (↑) and spin-down (↓) channels, at distance d^1 (top panel), d^2 (middle panel), and d^3 (bottom panel). For comparison, in the bottom panel the corresponding PDOS of a graphene ZZ edge is shown. The PDOS of F has been multiplied by 4.

Table 4.6: Spin-filtering efficiency (as defined in Equation 4.2), at zero gate-voltage and different separation distances.

	Spin-filtering efficiency (%)		
	d^1	d^2	d^3
Ni-Gr	-10.1	-51.4	-36.9
Cr-Gr	-0.5	-11.5	-11.6
Ni-O-Gr	-60.6	-66.0	-62.2
Cr-O-Gr	-1.5	-12.3	-45.8
Ni-F-Gr	-74.4	-89.0	-92.8
Cr-F-Gr	-0.4	-32.5	-86.1

increases with larger separation between Cr and graphene.

For the clean Ni-graphene interface, the SFE is small at equilibrium distance, while contamination of the graphene edge leads to much higher values. Upon extending the separation between Ni and graphene, the SFE generally increases. However, only in the case of F contamination full spin polarization is recovered, at least at the distances considered in this investigation.

In the light of these results, we can conclude that Ni-Gr contacts with passivated graphene edges could be a well suited candidate for spintronic applications. Especially, the passivation with oxygen leads to high spin-filtering efficiency at equilibrium distance while still providing a rather good contact quality, i.e., low contact resistance.

4.3 Comparison between 1D and 2D contacts

In the following, we compare our results for the edge and side contacts. In the introduction to this chapter, we mentioned that conventional metal-graphene side contacts were found to offer larger contact resistance as compared to metal-graphene edge contacts[130–136]. However, the results we obtained for Ni and Au for both contacting schemes seem to somewhat contradict these observations. Particularly, the unpassivated and H passivated Au-based side contacts have contact resistances of the same order of magnitude as the clean Au-based edge contact. The reason

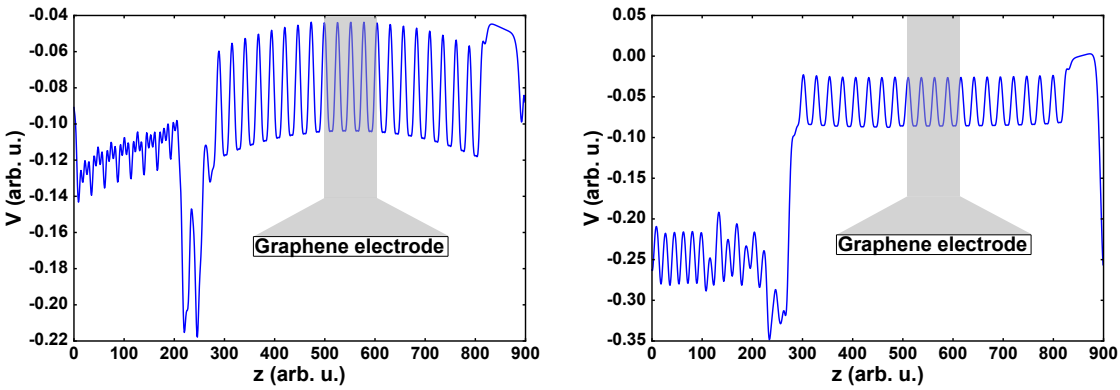

(a) (b)

Figure 4.19: Averaged electrostatic potentials for (a) Ni-Gr and (b) Au-Gr 2D contacts.

for this apparently contradictory result is that the side contacts we studied all have a small contact area between the graphene and the metals. Hence, the side contacts we consider here closely resemble the properties of edge contacts. Moreover, it has been previously shown that, while the influence of the contact area on the resistance of Ni-graphene side contacts is small[127], the resistance of Au-based side contacts strongly depends on the structural overlap between metal and graphene[129].

Furthermore, slight differences in the setups for the transport calculations might also play a role. For example, in the calculations for the edge contacts, we used 40 C rows of graphene in the device region, while for the side contacts we only used 22 C rows. Computational studies of side contacts with varying graphene channel length and symmetric transport setup, i.e., with electrodes attached at both sides of graphene, demonstrated that the length of the graphene channel can influence the contact resistance[137]. This is due to the decay of the electrostatic potential, which might not be well converged with respect to the channel length[117, 137]. Figure 4.19 shows the averaged electrostatic potentials of our 2D Ni and Au contacts with unpassivated graphene. The potential is flat in the graphene electrode region for both contacts. Interestingly, the potential is not flat within the metal and outside the graphene electrode for the Ni contact, while it is reasonably converged in the Au side contact. Still, further convergence

tests with respect to the graphene channel length need to be done, and, for now, our results obtained for the side contacts should be considered preliminary.

Chapter 5

Graphene nanoribbons and nanoporous graphene

Graphene nanoribbons (GNRs) are one dimensional stripes of graphene, whose electronic and magnetic properties depend on their width and edge structure[155–160]. In particular, armchair graphene nanoribbons (AGNRs) have a width dependent electronic gap[159], which makes them suitable for applications in carbon based nanoelectronics[161–163].

Atomically precise GNRs can be grown by the on-surface reaction of suitable designed molecular precursors[164]. During the last years, this route has been successfully used to tailor the dimension and the edges of GNRs with atomic control[164–169]. On-surface synthesis involves several steps[164, 170], as schematically depicted in Figure 5.1. First, molecular precursors with halogenic linker atoms are deposited on a metallic surface. Heating of the sample removes the linker groups from the precursors. This process is called *thermal activation* and leaves the precursors in a radical state. In this state, the precursor molecules can covalently link to each other, thus forming polymer structures. Further thermal annealing of the polymer structures initiates a procedure called *cyclodehydrogenation*. That is, the removal of hydrogen atoms at certain bond sites which, depending on the molecular precursor, leads to the formation of organic covalent frameworks[170] or GNRs[164].

Inspired by the above mentioned successful synthesis and characterization of

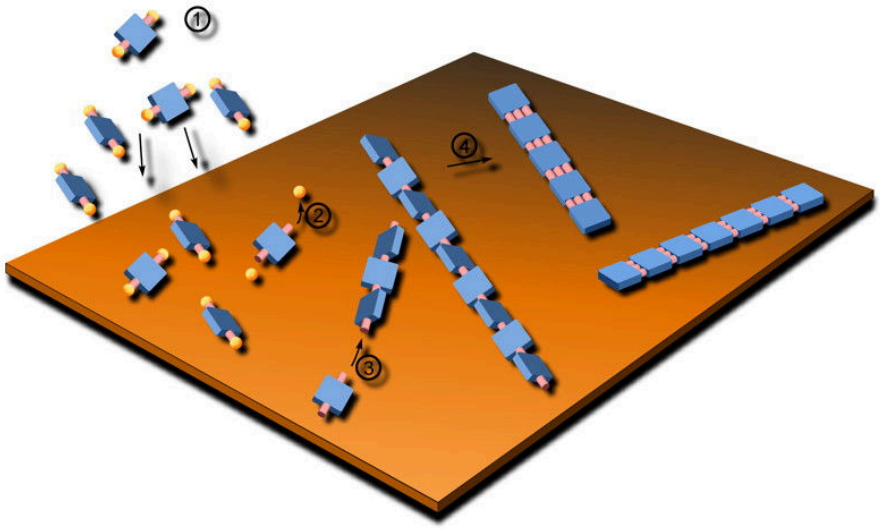

Figure 5.1: Scheme of on-surface synthesis concept for graphene nanoribbons. From: http://www.sps.ch/en/articles/progresses/molecular-lego-bottom-up-fabrication-of-atomically-precise-graphene-nanostructures-37/, accessed 21 May 2018.

covalently bonded carbon nanostructures, a strategy that leads to formation of nanoporous graphene (NPG) has recently been reported[169]. This new 2D material exhibits both semiconducting and nanosieving functionalities, which opens up new possibilities for graphene-based applications.

The use of a specific precursor, shown in panel A of Figure 5.2, allowed us to synthesize armchair graphene nanoribbons (AGNRs) with a periodic modulation of the width (panel C). We denote these ribbons 7-13-AGNR, as they exhibit alternating segments of 7 and 13 carbon atoms width. Even more interestingly, further annealing removes hydrogen atoms from the edges of the 13-segment of these 7-13-AGNRs, inducing inter-ribbon connections and giving rise to nanoporous graphene[169]. This way, the pores of the NPG can be manufactured with atomic precision, their shape and size being uniform over a large area. The whole pathway of our synthesis process from precursor to nanoporous graphene (NPG) is outlined in Figure 5.2.

Along with the experimental advances, a rapid progress has been made towards the theoretical understanding and prediction of the electronic and transport properties of carbon based nanostructures, including GNRs. In particular, in this

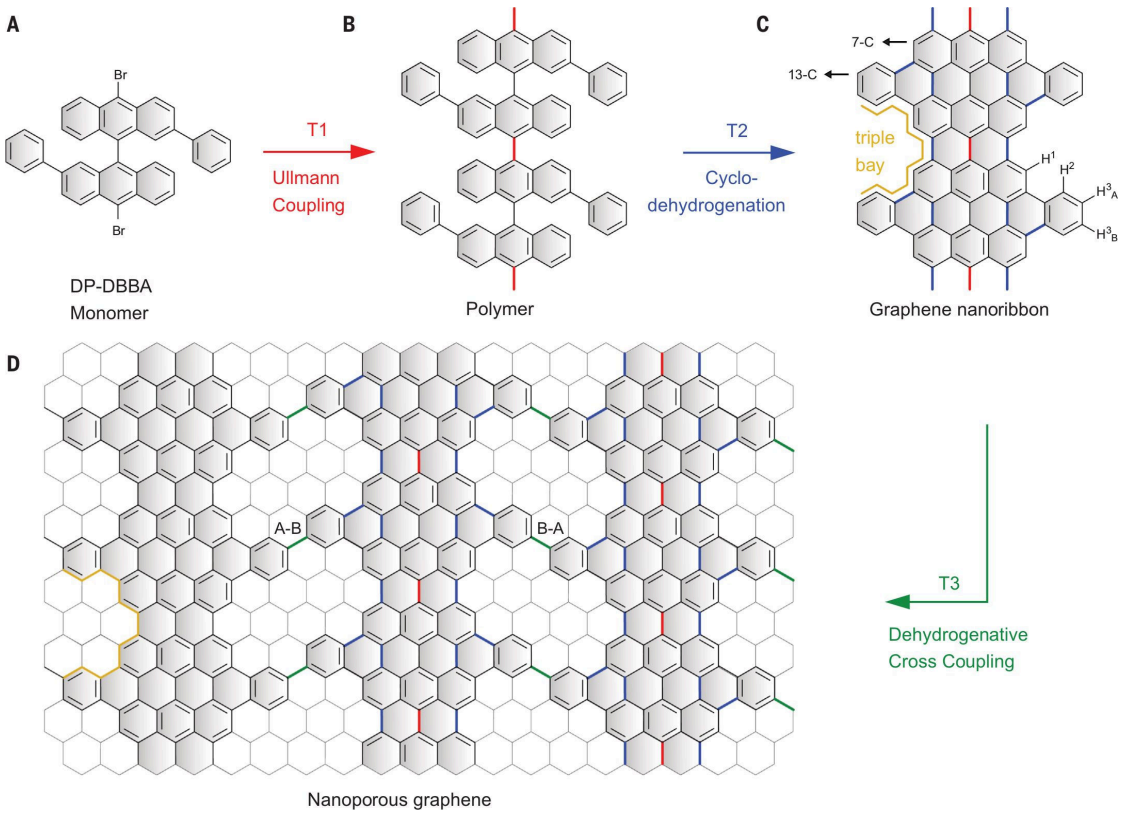

Figure 5.2: Schematic illustration of the synthesis pathway from the molecular precursor (A) via a polymer (B) and a width-modulated ribbon (C) to nanoporous graphene (D). From C. Moreno et al., *Science*, 360, 199-203 (2018). Reprinted with permission from AAAS.

chapter we present an extensive theoretical characterization of the electronic and transport properties of the above mentioned 7-13-AGNR and NPG. We will compare our computational predictions with the STM experiments performed by our collaborators. A short description of this experimental technique can be found in Appendix B.

5.1 Computational details

The setups used for the DFT calculations of the 7-13-AGNR and the NPG are shown in Figure 5.3. All atoms in these two structures were allowed to relax in the geometry optimization. Additionally, for the nanoribbon, the unit cell vector

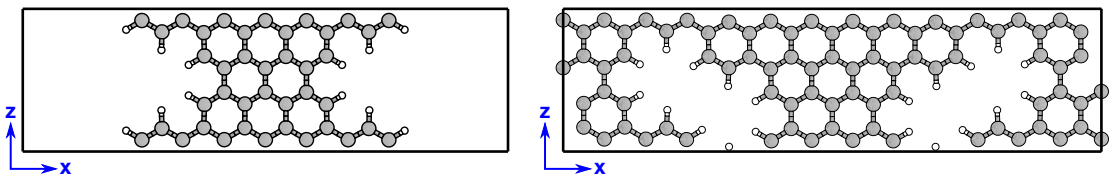

(a) (b)

Figure 5.3: DFT structures of (a) the 7-13-AGNR and (b) the NPG. The black lines indicate the unit cell. For the ribbon (a) the vacuum region at the edges was cut for the purpose of plotting.

in the periodic direction (z-direction) was also optimized.

All the calculations reported in this chapter were performed using SIESTA[81] and TranSIESTA[36, 37]. For the exchange-correlation functional we used the PBE[53] flavor of the GGA. We sampled the Brillouin zone applying a Monkhorst-Pack[144] grid of 1x1x51 k-points for the ribbons and 15x1x51 for the NPG. Transmission functions were sampled using 1x1x511 k-points for transport in z-direction and 151x1x1 k-points for transport in x-direction. For the self-consistent electronic optimization, we used the difference in the elements of the Hamiltonian matrix as convergence criterion and converged it until the maximum difference between two consecutive steps was less than 1×10^{-4} eV. We set the force convergence criterion for the structural optimizations to 0.01 eV/Å. Unless states otherwise, we used 25 Å of vacuum on either side of the ribbons and NPG in the non-periodic directions (i.e., 50 Å in total) and a mesh cut-off value of 400 Ry.

Regarding the basis set, we employed DZP orbitals with a PAO.EnergyShift of 0.01 Ry for the relaxations. Based on the relaxed geometries, the electronic structure was calculated using an extended DZP basis set, which includes carbon 3s and 3p orbitals. The use of this basis set provides a more accurate description of the unoccupied bands. Details on how to define the extended basis set in the SIESTA[81] input files can be found in Appendix C. We verified the impact of the new basis set with some test calculations. Figure 5.4 shows the DOS and band structure calculated for pristine graphene using the default (black) and modified DZP basis sets (yellow). Up to an energy of about 3.5 eV above Fermi-level, DOS and band structure are exactly the same for both basis sets. For higher energies, the additional orbitals in the extended basis set cause a down shift of the bands.

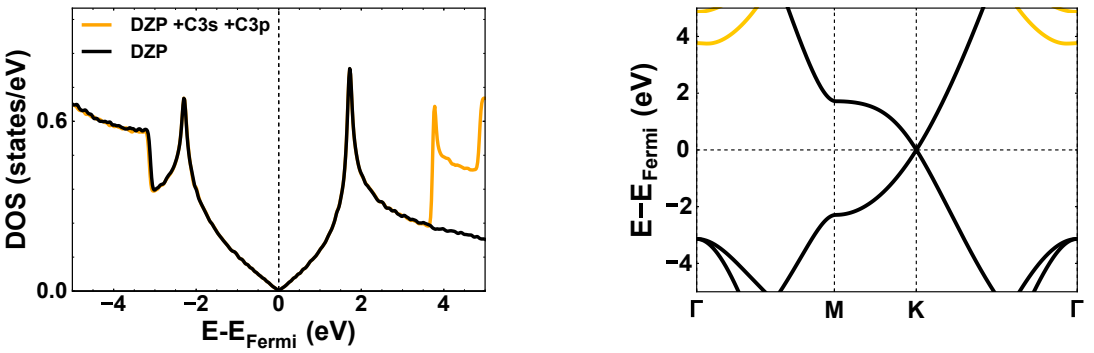

(a) (b)

Figure 5.4: Comparison of graphene (a) DOS and (b) band structure calculated with the SIESTA default DZP basis set (black) and a DZP which includes 3s and 3p states for the C atoms (yellow).

Furthermore, Figure 5.5 depicts the band structures of the 7-13-AGNR (see Figure 5.3a) calculated using SIESTA[81] with the extended basis set, and, using VASP[76–79] with a plane wave basis set. The band structures agree fairly well and the energies of the vacuum states (green lines) differ only by about 0.2 eV. For the VASP[76–79] calculations we used an energy cut-off of 400 eV, Gaussian smearing with a σ-value of 0.01 eV, an energy convergence criterion of 1×10^{-6} eV, and 1x1x51 k-points.

With respect to the band gap, it is well known that DFT significantly underestimates its value[171]. Currently, the tool of choice for obtaining more accurate band gaps is the GW[172–174] approximation. So, we performed GW[172–174] calculations as implemented in VASP[76–79, 175–178] to verify the semiconducting behavior of the 7-13-AGNR, as predicted by our DFT simulations. For that purpose, we relaxed the ribbon and obtained converged DFT wave-functions using VASP[76–79], applying the parameters mentioned above, except for a smaller k-point sampling of 1x1x25. Based on these simulations, we computed the quasiparticle corrections within the G0W0[172] approximation. In these calculations, we adopted a cut off energy of 60 eV for the response function, and included 576 bands and 50 frequency points. To verify the validity of our GW calculations for the novel 7-13-AGNR, we computed the band gaps for the more conventional 7- and 13-AGNRs. For these ribbons we obtained band gaps of 3.20 eV (7-AGNR)

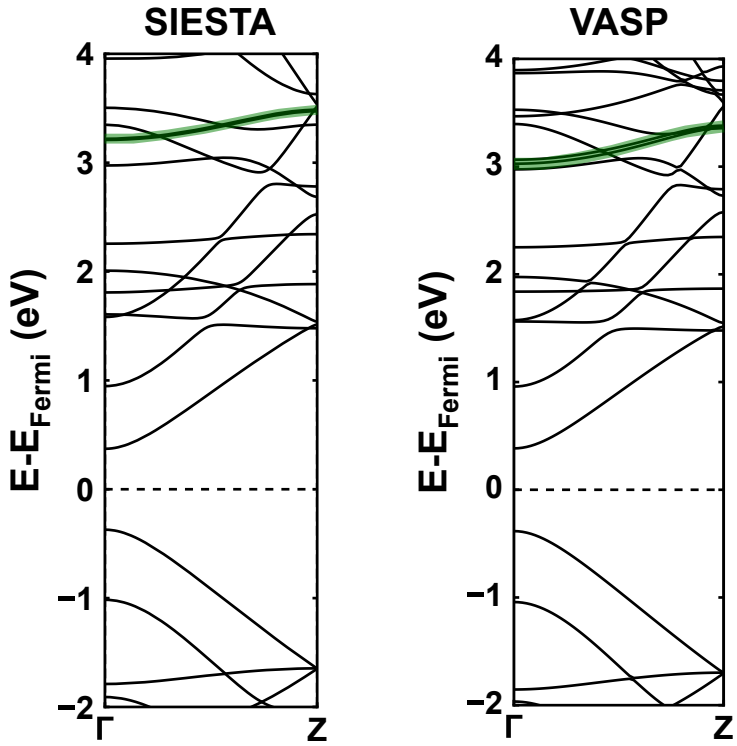

Figure 5.5: Band structures of the 7-13-AGNR calculated with the modified SIESTA basis set and in plane wave basis with VASP. The green lines indicate the vacuum state.

and 1.58 eV (13-AGNR), respectively. Here, our values are in fairly good agreement with those reported in literature, and, moreover, yield similar ratios between the DFT and GW band gaps[179, 180]. Small differences in the absolute band gap values between our calculations and literature might be attributed to possible deviations in the computational details (e.g., choice of exchange-correlation functional, k-sampling or pseudopotential). We did not perform GW calculations for the NPG, since this would require an extension of the k-point grid to two dimensions and, hence, would increase computational cost to an excessively high level. Nevertheless, we expect GW band gaps to follow similar trends as DFT gaps, which are slightly lower for the NPG compared to the ribbon.

5.2 7-13 armchair graphene nanoribbon (7-13-AGNR)

In this section, we focus on the 7-13-AGNR and compare its properties to the more common straight edge ribbons. Figure 5.6a shows a constant height STM image of the 7-13-AGNR, from which the successful fabrication of a GNR with periodically varying width is evident. The dI/dV spectra for the 7-13-AGNR is shown in Figure 5.6b, where the onsets for the valence band (VB) and conduction band (CB) are identified. From there, the experimental band gap is found to be $\sim$1.0 eV. The spectra in Figure 5.6b also reveals that the VB onset is close to -0.1 V. As we will show later, the same behavior can be observed for the NPG. This indicates pinning of the nanoribbon's VB to the Fermi-level of the Au substrate[181, 182]. Based on these observations, all gas phase calculations will be aligned with respect to this value.

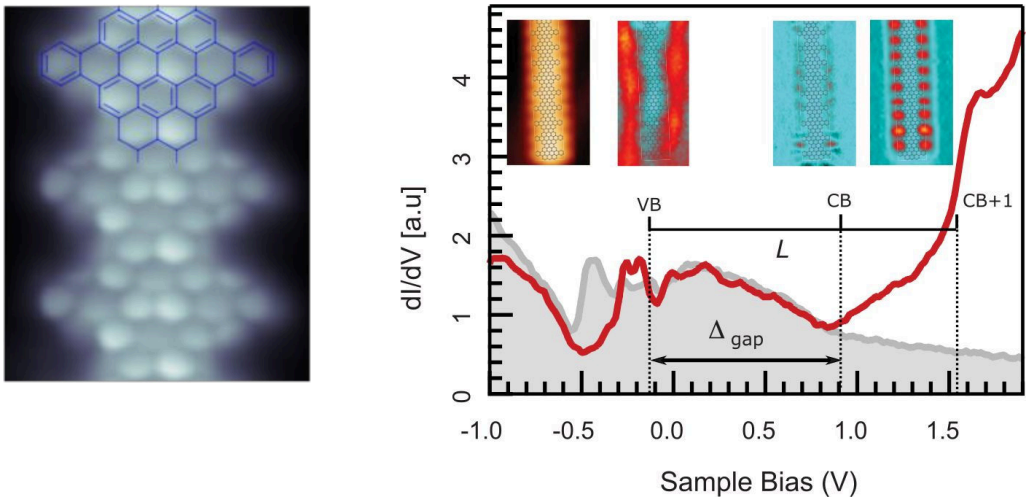

(a) (b)

Figure 5.6: (a) High-resolution constant height STM image of the structure of the 7-13-AGNR. (b) dI/dV spectra of the 7-13-AGNR. VB, CB, and CB+1 denote the onsets of valence band, conduction band, and conduction band+1, respectively. Grey color indicates the reference spectra of Au(111). The insets show a constant height image (left) and dI/dV maps for the VB, CB and CB+1. Details about the experimental setup are reported in [169]. From C. Moreno et al., *Science*, 360, 199-203 (2018). Reprinted with permission from AAAS.

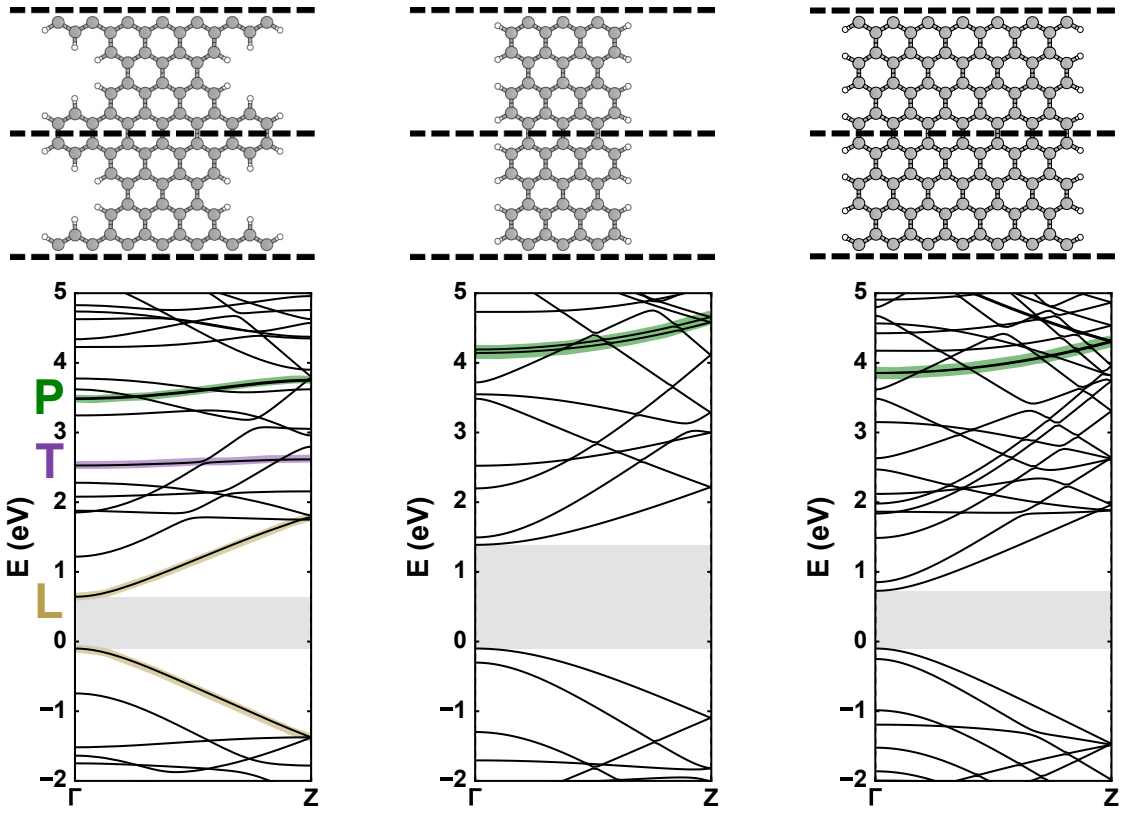

Figure 5.7: Geometries (upper panels) and band structures (lower panels) for (a) 7-13-AGNR, (b) 7-AGNR, and (c) 13-AGNR. The black dashed lines in the structure plots indicate the unit cell size in the periodic direction. L and T indicate longitudinal and transversal bands in the 7-13-AGNR. P (or green stripes) mark the vacuum states. The gray shaded area indicated the band gap opening at Γ-point.

In order to characterize the electronic properties of the 7-13-AGNR, we compare the width-modulated ribbon with related straight edge ribbons, namely the 7 and 13 C atoms wide ribbons (referred to as 7-AGNR and 13-AGNR, respectively). The geometries and band structures of the three ribbons are shown in Figure 5.7, where the shaded areas in the lower panels represent the corresponding band gaps. We obtain band gaps of 0.74 eV, 0.82 eV, and 1.49 eV, for the 7-13-AGNR, the 13-AGNR, and the 7-AGNR, respectively. The values for the two straight edge ribbons are in good agreement with literature[159]. Regarding the band gap of

the 7-13-AGNR, it is smaller than the band gap of the 13-AGNR, highlighting the role of edge topology in determining band gaps. As mentioned above, the experimental band gap of the ribbon was estimated to be ∼1.0 eV. This discrepancy between experiment and DFT is not surprising, because of the above mentioned underestimation of DFT gaps[171]. Performing GW calculations, we obtain a band gap of 1.36 eV for the 7-13-AGNR. Note that the experimental value (∼1.0 eV) is slightly lower than the GW band gap, as expected from the screening effect in the underlying substrate.

To gain further understanding on the character of the frontier orbitals that define the band gap, we analyze the wave-functions of the VBs and CBs at Γ-point for the three ribbons, shown in Figure 5.8. Clearly, the character of the VB is the same for the three ribbons, and the same holds for the CBs. It is not surprising to find these similarities for the 7-AGNR and the 13-AGNR, since they belong to the same family of AGNRs. Interestingly, in the case of the 7-13-AGNR these bands are confined on the 7 carbon atoms wide backbone of the ribbon.

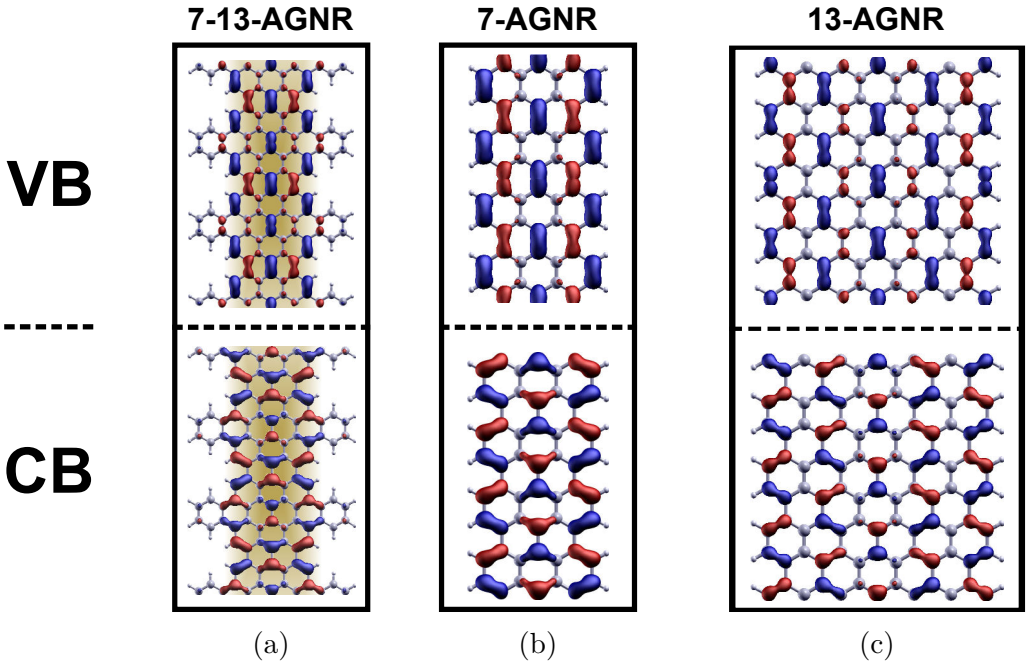

Figure 5.8: Iso-surface plots of wave-functions at Γ-point for the valence bands (upper panels) and conduction bands (lower panels) of the 7-13-AGNR (a), the 7-AGNR (b), and the 13-AGNR (c). The iso-value in these plots is 0.09 $Å^{-3}$.

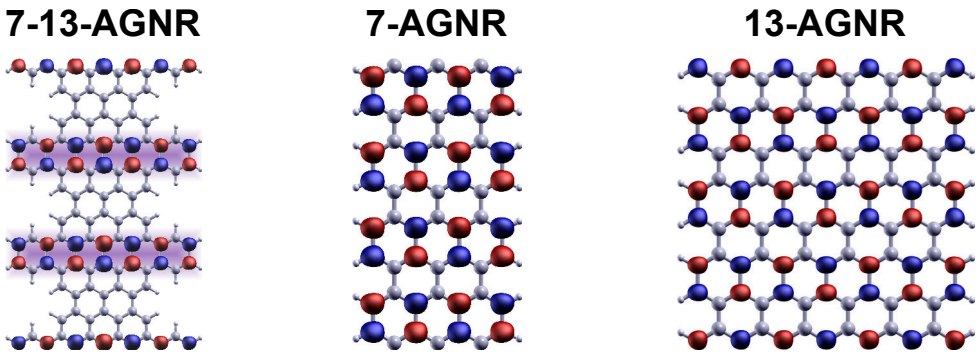

(a) E-E$_{VB}$ = 2.62 eV (b) E-E$_{VB}$ = 3.65 eV (c) E-E$_{VB}$ = 3.25 eV

Figure 5.9: Iso-surface plot of the wave-function of (a) a transversally dispersing band in the 7-13-AGNR and (b,c) bands of same character in the 7-AGNR and 13 AGNR, respectively. The iso-value in these plots is 0.09 Å^{-3}. Energies of the bands are given in the captions of the subfigures.

Since these bands disperse along the backbones of the ribbons, in ΓZ-direction, we denote this family of bands as *longitudinal (L)* bands. Bands belonging to this family can also be found at energies higher than the CB energy.

More interestingly, in the band structure of the 7-13-AGNR we also identify significantly flat bands (as the one indicated by violet color in Figure 5.7a on page 74), whose wave-function is shown in Figure 5.9a. For this family of bands, termed *transversal (T)* bands, the wave-functions are localized on the periodically repeated 13 C wide segment. The origin of the localization of these bands is the superlattice periodicity introduced by the width modulation of the 7-13-AGNR[169]. Indeed, bands of the same character as the transversal band in the 7-13-AGNR also exist in the 7- and 13-AGNRs (see Figure 5.9b,c) but, due to the absence of periodic variations in the lattice potential along the ribbon, they are not localized in the straight edge ribbons. The origin of the L and T bands described here are the s and p orbitals of the carbon atoms.

A third family of bands can be found in these ribbons, whose origin is not directly related to the valence orbitals of the carbon atoms (2s and 2p). For bands of this family, indicated by green color in the band structure plots of the three ribbons (Figure 5.7, page 74), the wave-functions reach far into the vacuum. We demonstrate this by analyzing the local density of states (LDOS) as a function of energy and position in the direction transversal to the ribbon (x-direction). For

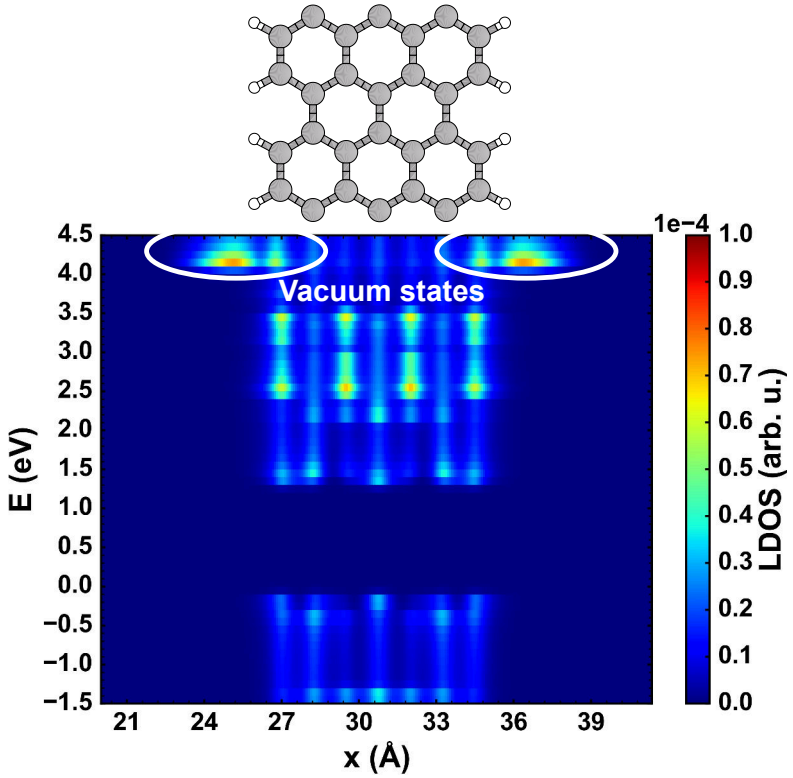

Figure 5.10: Averaged LDOS map for the 7-AGNR. The structure above indicates the position of the ribbon's atoms in x-direction. The white ellipses pinpoint the vacuum states. The energies are aligned to the energy of the valence band maximum.

this purpose, we calculated the LDOS in energy intervals of 0.1 eV, averaged it for each interval in the y- and z-directions, and plotted it as contour map. Since the 7- and 13-AGNRs belong to the same family of GNRs, we will only consider the first one in the following analysis. The LDOS map for the 7-AGNR is shown in Figure 5.10. The bright spots at energies around 4 eV to 4.5 eV above the valence band maximum (VBM) indicate vacuum states localized at the edges outside the ribbon.

For the 7-13-AGNR, the width modulation makes the identification of states localized in the vacuum region from the LDOS a bit more intricate. Therefore, we plotted the LDOS maps for the 7- and 13-parts of the ribbon separately. The areas used for computing the LDOS of these two parts are shown in green (7-segment) and brown (13-segment) in the 7-13-AGNR atomic structure above the LDOS

maps in Figure 5.11. The background colors of the LDOS maps in Figure 5.11 are chosen accordingly. In the LDOS map of the 7-segment (green) we can identify sates located outside the ribbon's backbone at energies between 3.5 eV and 4.0 eV, which is about 0.5 eV lower than for the corresponding states in the 7-AGNR. Since their main contributions are located within the cove of the 7-13-AGNR, we call them *cove states* (for reasons that become clear later on they are also denoted as P states in the band structure plots). Within the energy range for which a cove state can be seen in the LDOS of the 7-segment, the map of the 13-segment (brown) shows only a low contribution in the vacuum region outside the ribbon.

The rightmost inset of Figure 5.6 (page 73) shows the dI/dV map of the CB+1 of the 7-13-AGNR, which shows a state localized in the vacuum region between the 13-segments of the 7-13-AGNR occurring at a voltage of 1.6 V. This state is the experimental equivalent to the cove states we have found in our DFT calculations. These states do not originate from atomic orbitals or their hybridizations, instead, they arise from free electron-like image potential states (IPS) which are confined in the vacuum region at the edges of GNRs. The origin of IPS is related to the so-called *image charge effect*, which is the induction of a charge underneath a surface by a charge of opposite sign in the vacuum region above the interface. A consequence of this effect is the trapping of electrons above a surface at energies higher than the vacuum level[183–188].

Particularly, for graphene this means that while solutions of the Schrödinger equation with the lowest principle quantum numbers ($n<3$) originate from the carbon atoms, states with $n\geq3$ originate from IPS and, thus, do not follow the lattice modulation[189, 190]. As a consequence, electrons in these states behave as nearly-free electrons (NFE). Upon rolling up graphene into nanotubes or fullerenes, the IPS interacts with itself, leading to the emergence of 1D NFE bands or superatom molecular orbitals (SAMOs)[191–194]. In the case of GNRs, the potential at the edges and in the plane of the ribbons differ, which is predicted to give rise to a 1D NFE along the edges[195]. Hence, we can infer that the vacuum state we have observed in the LDOS of the 7-AGNR corresponds to such a NFE state. For the 7-13-AGNR, NFE states are localized within the cove region of the ribbon and resemble the SAMOs described above.

At this point we should clarify the qualitative character of our analysis of

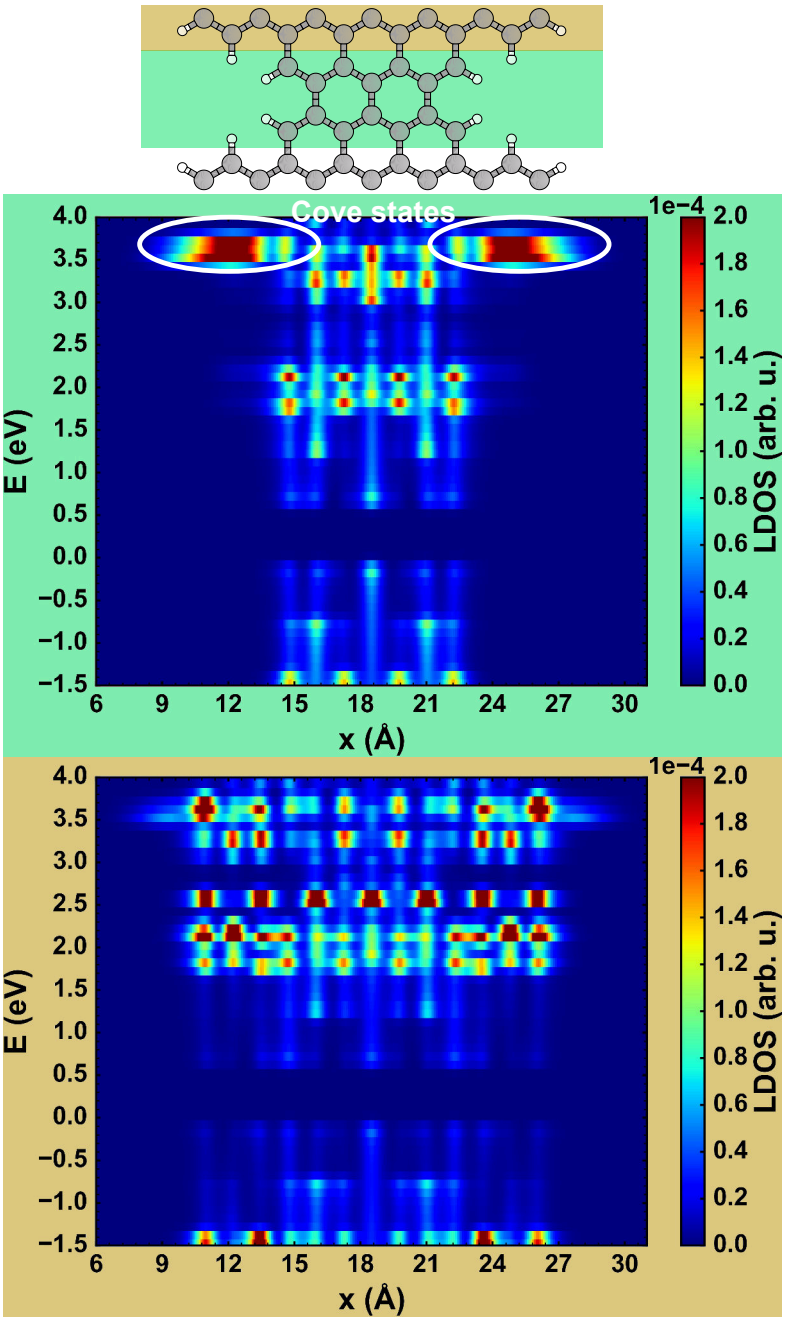

Figure 5.11: Averaged LDOS maps of 7-, and 13-segments of the 7-13-AGNR. The structure above indicates the position of the ribbon's atoms in x-direction with the green and brown areas indicating the parts of the ribbon for which the LDOS was averaged. The white ellipses pinpoint the vacuum states. The energies are aligned to the energy of the valence band maximum.

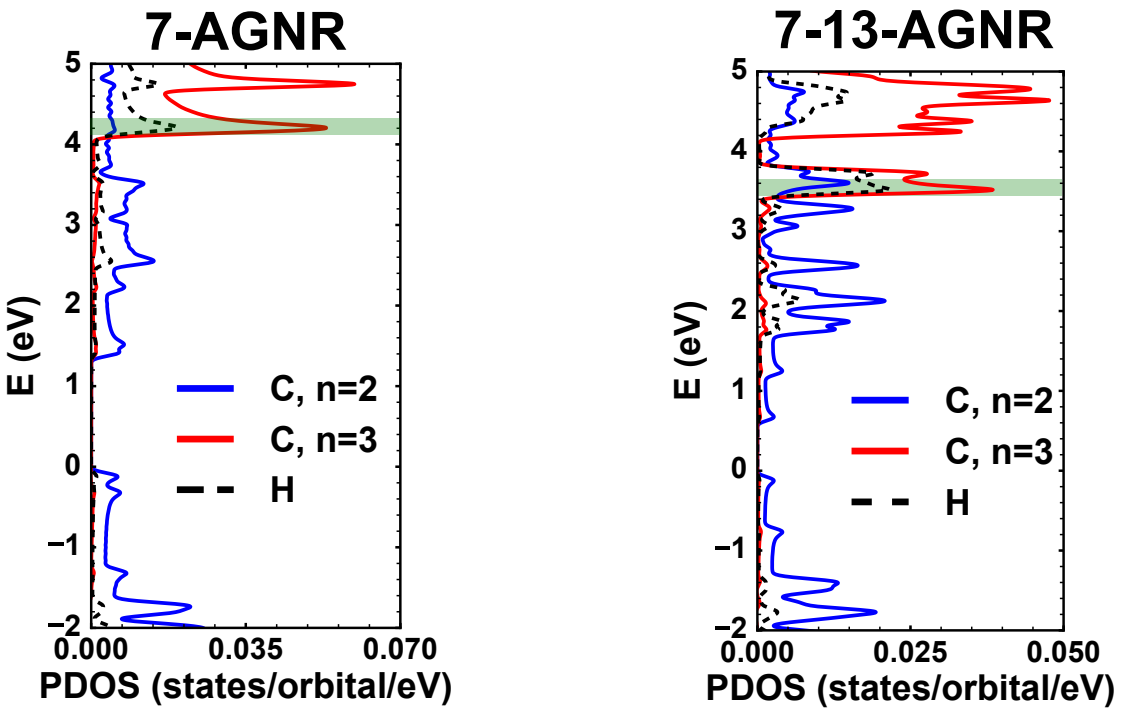

(a) (b)

Figure 5.12: Projected DOS for the (a) 7-AGNR and (b) 7-13-AGNR, respectively. The green shaded areas in the PDOS denote the lowest lying vacuum and cove states

vacuum states. In the vacuum region above a surface, the image potential decays with $1/(4z)$, z being the distance from the surface. Contrarily, in the Perdew-Burke-Ernzerhof (PBE) approximation to the exchange-correlation potential we applied in our DFT calculations, the potential decays exponentially. Thus, our calculations do not represent IPS directly, but rather give a qualitative description of the lowest lying vacuum states.

The results above clearly indicate the usefulness of LDOS maps for finding the energy range in which vacuum states could appear. Nevertheless, further insight into the origin of these states can be obtained by looking at the PDOS of the 7- and 7-13-AGNRs. Figure 5.12 shows DOS projected onto the carbon orbitals with n=2, and n=3, as well as onto the hydrogen orbitals for the 7-AGNR and 7-13-AGNR. The green shaded area in the PDOS plots indicates the position of the lowest lying vacuum state. Clearly, for both ribbons, the PDOS is dominated

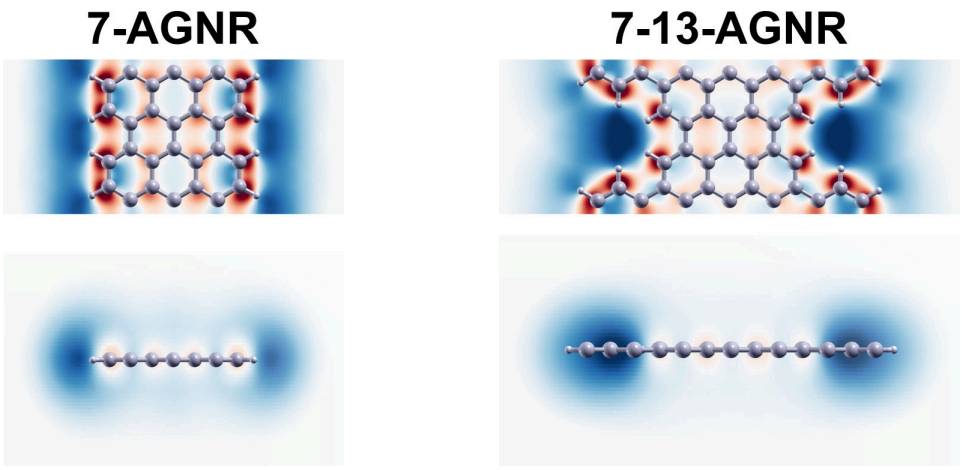

(a) E-E$_{VB}$=4.24 eV (b) E-E$_{VB}$=3.58 eV

Figure 5.13: Wave-functions of the lowest lying vacuum states for the (a) 7-AGNR and (b) 7-13-AGNR, respectively. Wave-function plots correspond to cuts through a plane of the real space grid.

by carbon states at this energy, with the main contribution coming from the n=3 orbitals as is expected for these NFE-like states. Besides, also hydrogen states have a significant intensity in this energy range.

While the LDOS and PDOS indicate the energy range and origin of vacuum states, a better picture of their character can be obtained from the wave-functions. Figure 5.13a depicts the wave-functions for the 7-AGNR, from which it is clearly visible that a great part of it is localized in the vacuum region along the edge and at the carbon edge atoms. The side view of the wave-function reveals that it is not only localized in the plane of the ribbon, but also has relevant contributions out-of-plane. The situation is qualitatively similar for the width-modulated 7-13-AGNR (see Figure 5.13b). From the band structures shown in Figure 5.7 on page 74, we can estimate the energy of the vacuum states of the 7-AGNR and 7-13-AGNR. Interestingly, the width modulation of the ribbon causes a localization of the vacuum state in the cove region of the 7-13-AGNR. For both ribbons, the wave-function also has a significant intensity at the edge atoms, explaining the contributions of carbon n=2 orbitals in the PDOS (see Figure 5.12).

The evolution of cove state localization and energy as a function of the cove size is shown in Figure 5.14. Starting from the delocalized vacuum state of the

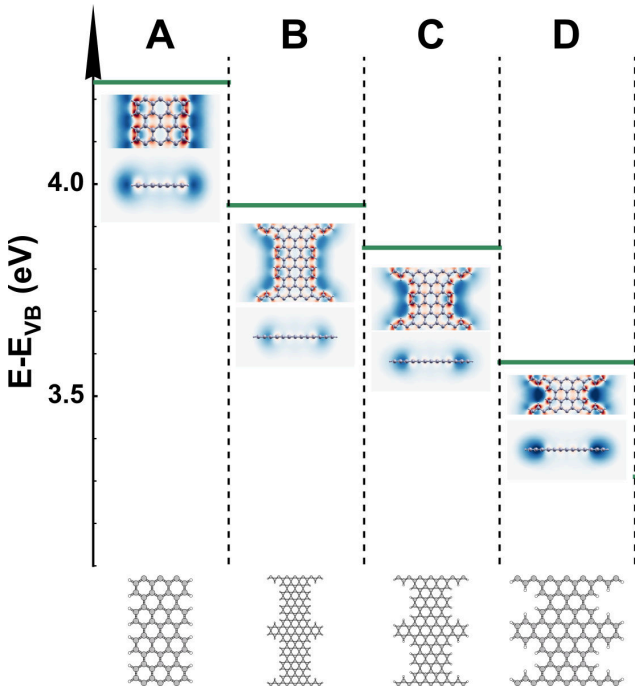

Figure 5.14: Evolution of the cove state energy and localization with respect to the cove size.

7-AGNR (panel A), introducing a 13-segment leads to a localization of the vacuum state in the cove (panels B to D). This localization gets stronger with decreasing cove size. Moreover, the energy of the vacuum states with respect to the VBM decreases with smaller cove sizes, similarly to the way the energy of the SAMO of a C60 molecule decreases in comparison to the 2D image potential state it is derived from[192].

5.3 Nanoporous graphene (NPG)

As previously described, the lateral interconnection of 7-13-AGNRs leads to the formation of NPG comprising an ordered array of pores separated by the backbones of the ribbons. In this section, we report the characterization of the electronic and transport properties of the resulting 2D material.

First, we investigated whether the 7-13-AGNRs are indeed covalently linked to each other. Figure 5.15 shows a STM topography and high-resolution STM image of two connected 7-13-AGNRs. By fitting a structural model to the high-resolution STM image, the distance between the two ribbons was estimated to be similar to C-C bonds, which points towards covalent bonding between the ribbons. To confirm the forming of a covalent bond between the ribbons, we calculated the bond distances for hydrogen bond and covalently linked ribbons. By just placing two ribbons side-by-side, with a slight offset in the periodic direction, they get connected via a hydrogen bond. The structure for this hydrogen bonded double ribbon is shown in Figure 5.16a, with the hydrogen atoms colored red indicating those that participate in the H-H bond. Due to the relative weakness of H-H bonds in general, the two ribbons are not very strongly connected and, accordingly, the calculated distance between the H atoms involved in the linking is 2.40 Å. An alternative scenario is to remove the hydrogen atoms depicted in red in Figure 5.16a and create a covalent bond between the corresponding C atoms. This results in

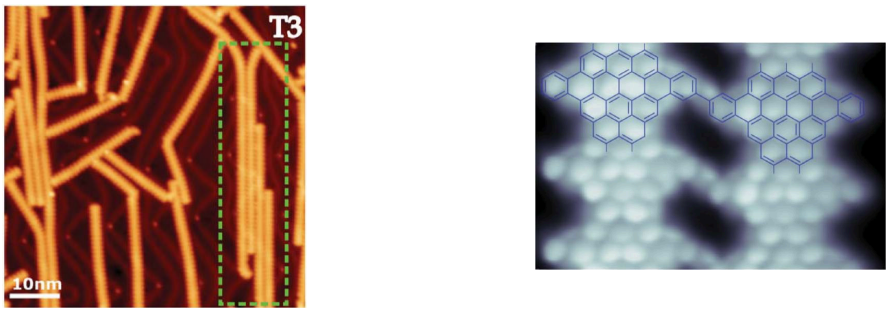

(a) (b)

Figure 5.15: (a) STM topography and (b) high-resolution STM image of two connected 7-13-AGNRs. From C. Moreno et al., *Science*, 360, 199-203 (2018). Reprinted with permission from AAAS.

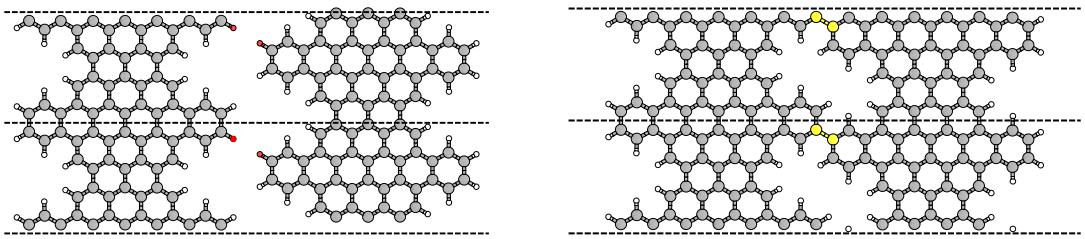

(a) (b)

Figure 5.16: Two 7-13-AGNRs connected by (a) a hydrogen bond between the atoms colored red and (b) a covalent C-C bond formed between the C atoms colored yellow. The black dashed lines indicate the unit cell in the periodic direction.

a slightly more compact structure, illustrated in Figure 5.16b, with the C atoms forming the covalent bond depicted in yellow. The distance between the C atoms participating in this bond is about 1.50 Å, which is a bit larger than the C-C bonds within the backbone of the ribbons (∼1.45 Å). In both bonding configurations, the structures stay entirely planar upon relaxation. From these calculations and the approximate distances inferred from the experiment, we can conclude that the ribbons indeed form covalent bonds to each other during the on-surface synthesis process.

The NPG can be grown almost free of defects over a large area, as can be seen from the STM topography in Figure 5.17a. The black square in this image indicated the region for which a close-up (Figure 5.17b) of the STM topography

(a) (b)

Figure 5.17: (a) STM topography of a surface covered with up to 50 nm by 70 nm large NPG domains. (b) Close-up STM topography of NPG. From C. Moreno et al., *Science*, 360, 199-203 (2018). Reprinted with permission from AAAS.

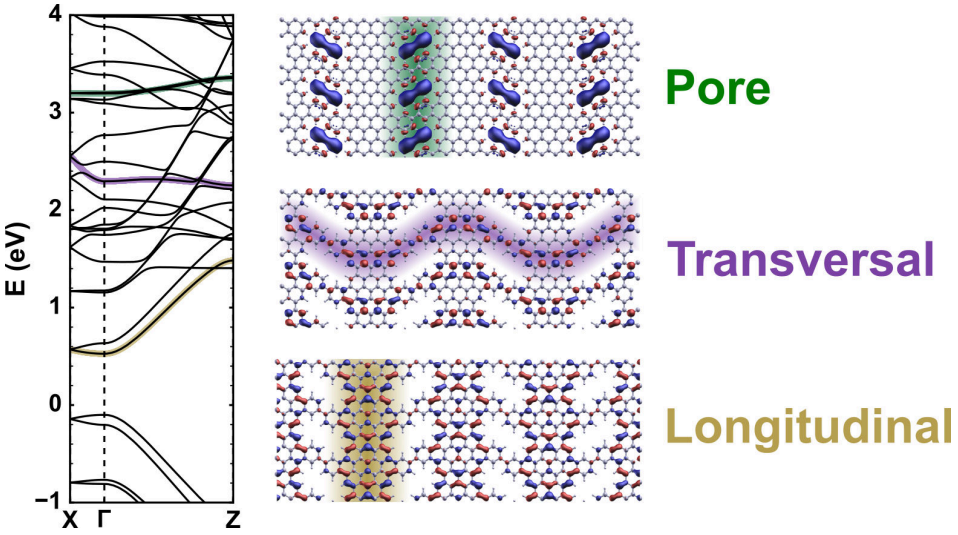

Figure 5.18: Band structure and iso-surface wave-function plots at Γ-point of selected bands for the NPG. The iso-value for wave-function plots is 0.065 $Å^{-3}$.

was recorded. From this close-up STM image, the pore orientation can be seen. Neighboring rows of pores in the NPG can have parallel or anti-parallel orientation. As can be seen from the STM topology in Figure 5.17b, the orientation of the pores is rather random in the experiments.

We started our DFT characterization of the electronic properties of the NPG with the anti-parallel pore orientation, because it allows usage of an orthogonal unit cell. As can be seen from the band structure of the NPG in Figure 5.18, its band gap has a value of 0.62 eV, which is 0.12 eV smaller than for the 7-13-AGNR. Remarkably, we found the same types of bands in the band structure of the NPG as in the 7-13-AGNR. Like for the ribbon, the VB and CB of the NPG disperse in longitudinal direction (ΓZ), as can be seen from the wave-function of the CB in Figure 5.18. These bands are protected within the backbone and remain unperturbed upon formation of the NPG, that is, they do not exhibit any dispersion in the transversal direction (ΓX). In contrast, the transversal bands, which are localized in the 13-segment of the 7-13-AGNR, allow for a substantial interribbon coupling. Hence, in the case of the NPG, these bands form a 1D dispersing state. The resulting wave-function, shown in the middle-right panel of Figure 5.18, displays wave-like stripes running along the NPG in ΓX-direction, which do not interact with each other.

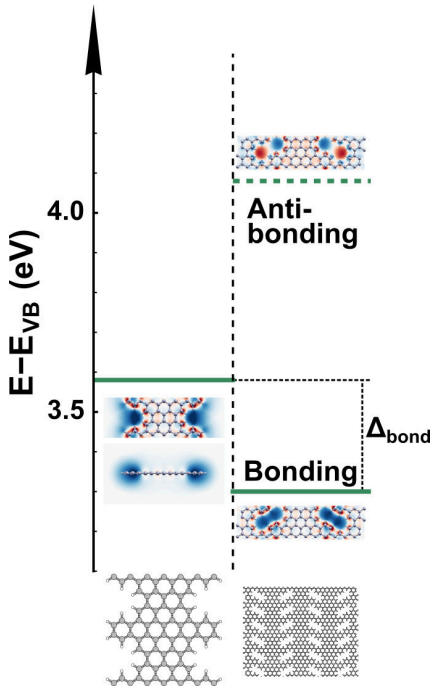

Figure 5.19: Energies of cove state of the ribbon (left) and of the bonding and antibonding pore states of the NPG.

As for the states localized in the cove regions, when NPG is formed, the interaction of the two merging cove states gives rise to two localized states in the newly formed pore region (P states). One of these two states, denoted as bonding state, has a lower energy than the original cove states, and its wave-function is shown in the top-right panel of Figure 5.18. The other pore state has a higher energy and is termed anti-bonding state. Figure 5.19 shows the energies of the bonding and antibonding pore states of the NPG in comparison with the cove states of the 7-13-AGNR. Here, Δ_{bond} indicates the difference in energy between the 7-13-AGNR cove state and the bonding pore state of the NPG, and assumes a value of 0.28 eV. From these results, it is clear that the NPG inherits its outstanding electronic properties from the properties of its building blocks, the 7-13-AGNR.

To verify the impact of the pore orientation on the electronic properties of the NPG, we calculated the band structure and wave-functions also for the NPG with parallel pores, as shown in Figure 5.20. Basically, everything we mentioned above for the anti-parallel pore orientation also holds for the NPG with parallel pores.

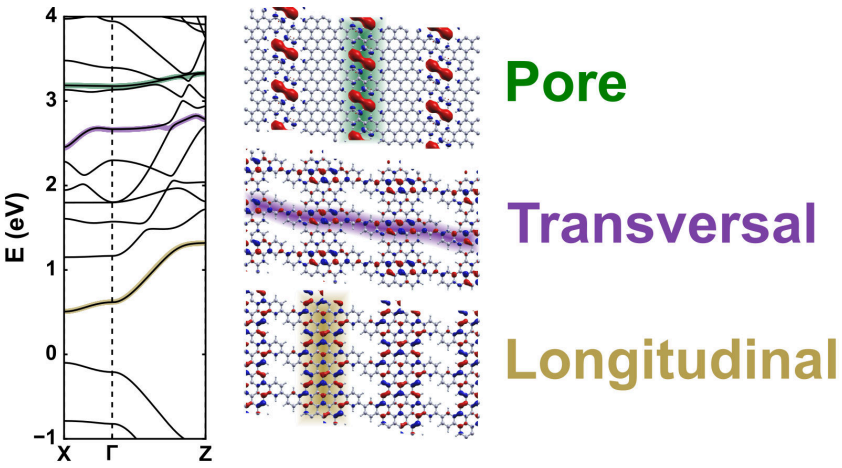

Figure 5.20: Band structure and wave-functions for the NPG with parallel pore orientation. The iso-value for wave-function plots is 0.1 $Å^{-3}$

VB and CB are still localized on the 7-segment and disperse longitudinally. Also, the transversally dispersing 1D state exists in this pore orientation as well. And, the pore states can be found at nearly the same energies for both pore orientations, with their difference being ∼0.05 eV. Therefore, we focused in our calculations on the anti-parallel orientation, which allows us to use an orthogonal unit cell.

Figure 5.21a shows dI/dV spectra for the NPG. Here, the red and blue curves were acquired at the peripheral cove and pore regions, respectively, and the gray shaded curve indicates the dI/dV spectra of the Au(111) surface. The difference between the red and blue curves indicated by the dashed vertical lines corresponds to the formation to the energy shift of the bonding pore state upon interaction of the cove states of two ribbons. This shift was determined experimentally to be 0.3 eV and, thus, agrees very well with the value we obtained with DFT. Figure 5.21b shows a dI/dV map of the pore state, from which the nature of the pore state is apparent. As predicted by our DFT calculations (see Figure 5.18), the pore state's double-lobed structure is clearly visible.

To demonstrate that the anisotropic dispersion behavior of the bands of the NPG is reflected in its conductance properties, we performed transport calculations for the NPG with anti-parallel pore orientation. Connecting graphene electrodes to NPG allows us to study the transport properties along the ribbon backbone and in transversal direction. Figure 5.22 on page 89 shows the transport setup for

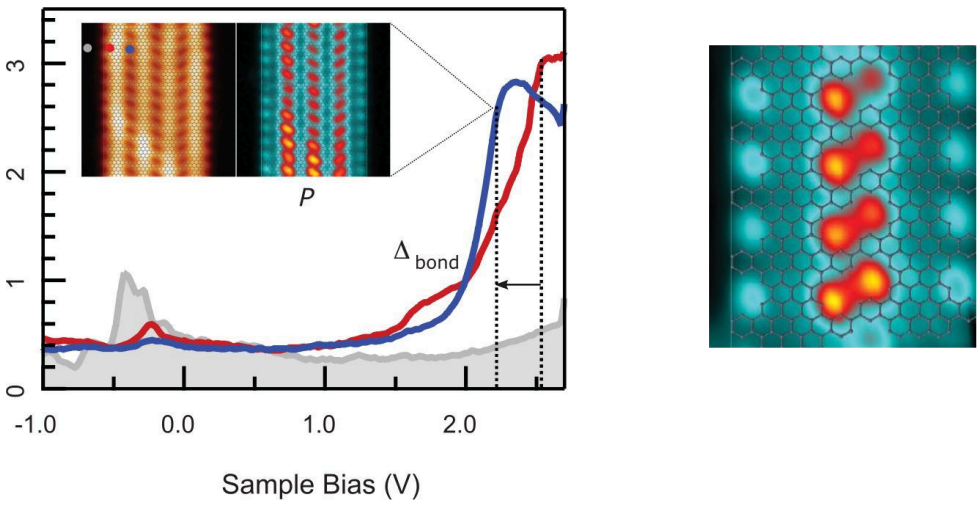

(a) (b)

Figure 5.21: (a) dI/dV spectra of the NPG recorded at the peripheral cove (red) and pore (blue) regions. Gray indicates the spectra of the Au(111) substrate. Insets show a STM topography (left) and dI/dV map of the pore state (right). (b) Larger image of the dI/dV map of the pore state. From C. Moreno et al., *Science*, 360, 199-203 (2018). Reprinted with permission from AAAS.

the transport simulations. Thermally broadened conductances for both transport directions as well as for pure graphene are depicted in Figure 5.23a. We can identify three regimes of different transport properties in the NPG[169]. Around the Fermi-level there is a region where conductance is suppressed (white background), corresponding to the NPG band gap. Going further away from Fermi-level, transport along the backbone of the ribbon sets in (yellowish area) while the conductance in transverse direction is still extremely low. At energies of $\pm 1.2\,\mathrm{eV}$ with respect to Fermi-level, states conducting in transversal direction start to appear, leading to a regime with transport in longitudinal and transversal directions (violet). Independently of the transport direction, the conductance of the NPG is always significantly lower than the intrinsic graphene conductance (black line in Figure 5.23). These results clearly demonstrate the anisotropic transport properties of the NPG, a behavior that is rather unique and distinguishes this 2D material from others. This anisotropic transport properties might be of great value for the design of novel electronic or sensing applications.

To address the semiconducting behavior of the NPG experimentally, its trans-

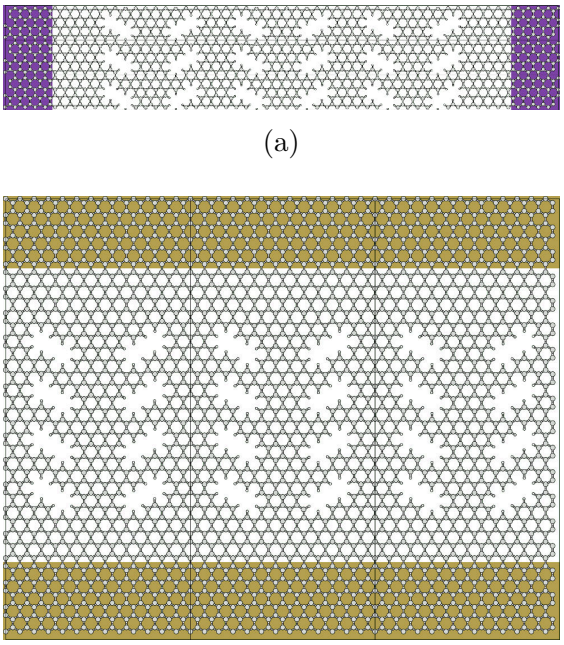

(a) (b)

Figure 5.22: Setup for transport calculations (a) in transversal direction and (b) in longitudinal direction along the ribbon backbone. Violet and brown shaded areas indicate the graphene electrodes. Black lines indicate the supercell used in the simulations. Both structures are repeated 3 times in the periodic direction.

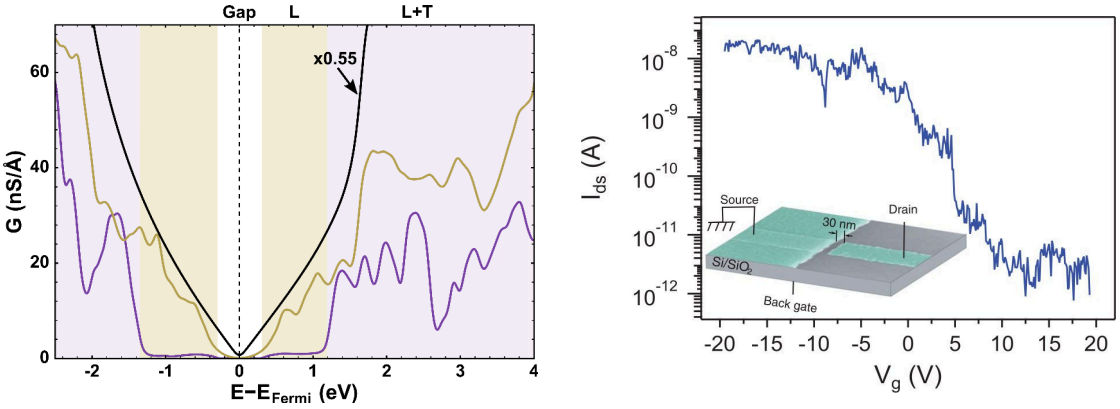

(a) (b)

Figure 5.23: (a) Thermally broadened conductances in transversal (violet) and longitudinal (brown) directions. The black line indicates intrinsic graphene conductance for comparison, multiplied by a factor of 0.55. (b) Drain-source current (I_{ds}) as a function of applied gate voltage (V_g) for a NPG device with a channel length of 30 nm.

port response was probed using FET structures. For this purpose, the NPG was transfered to a Si/SiO_2 substrate and connected to Pd electrodes. Figure 5.23b shows the drain-source current (I_{ds}) as a function of applied gate voltage (V_g), with a drain-source voltage (V_{ds}) of $-1\,V$, for a NPG device with a channel length of 30 nm. The current through this device decreases sharply upon increasing the gate voltage, indicating that transport is dominated by holes. The on-off ratio of this NPG based device is, with approximately 10^4, comparable to one of GNRs[196]. Furthermore, the bias response suggests limitation of transport in our devices due to Schottky junction contacts.

In conclusion, in this section, we have demonstrated the outstanding electronic properties of the NPG and that it inherits them from the 7-13-AGNR, which acts as the basic building block for the NPG. We proved the semiconducting behavior of this novel 2D material computationally and experimentally, thus, showing its potential for electronic applications. Finally, through our transport calculations, we showed the anisotropic conductance properties of the NPG, which could be important, for example, for sensing applications.

5.4 Influence of structural modifications

The properties of the NPG can be tuned by modifying the size, density, morphology, and chemical composition of the pores. Particularly, modifications leading to lower pore state energies and, thus, making them accessible in transport experiments are desirable. In this section, we will focus on the edge morphology of the 7-13-AGNR. As an illustrative example, we will consider the attachment of phenyl-rings to each side of the 13-segment of the 7-13-AGNR. Especially, when connecting ribbons and building larger structures this will provide a way to engineer pores for a specific purpose.

The structure of the phenylated 7-13-AGNR we studied in this work is shown in Figure 5.24a. Here, the blue stripes indicate the additional phenyl-rings attached to the 13-segment of the ribbon and the black dashed lines show the unit cell in the periodic direction. As can be seen from the band structure in Figure 5.24b, the band gap of the ph-7-13-AGNR amounts to 0.73 eV, essentially the same value as for the 7-13-AGNR ribbon. From the band structure it is also clear, that

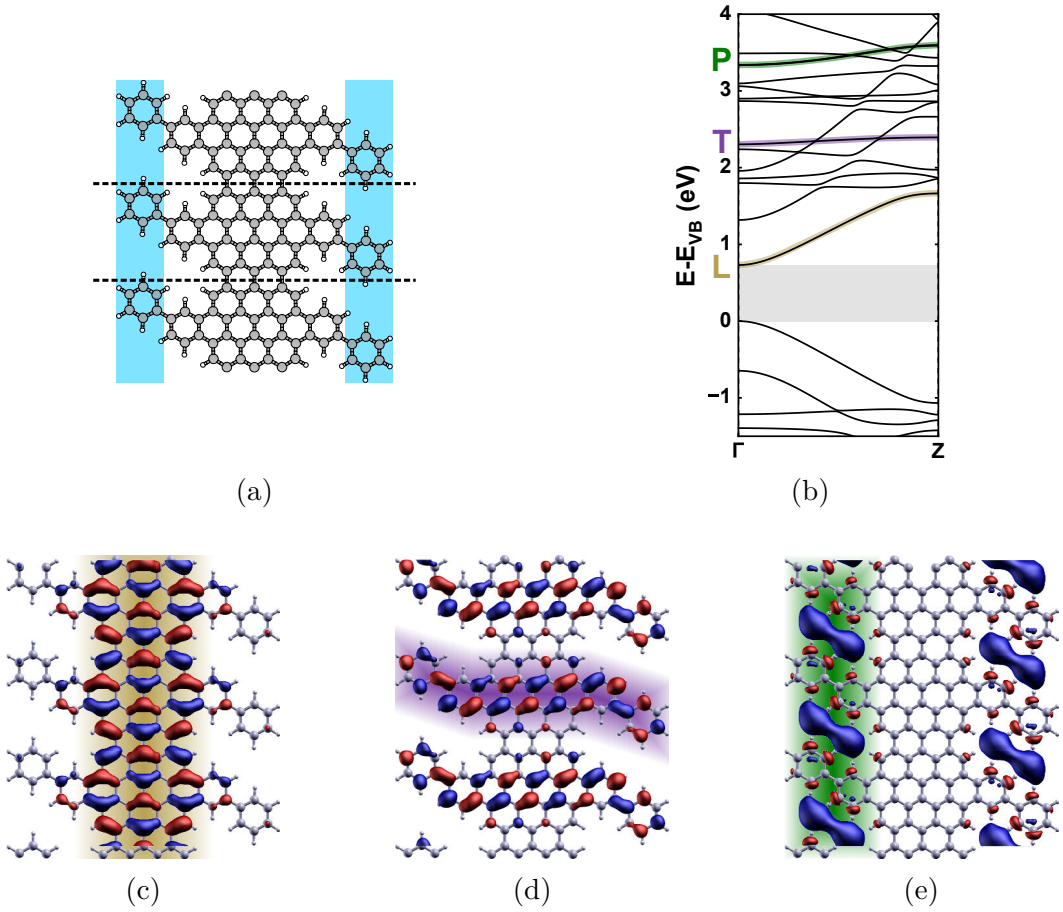

Figure 5.24: (a) Structure of the ph-7-13-AGNR. The blue stripes indicate the additional phenyl-rings compared to the default 7-13-AGNR. The dashed lines indicate the unit cell in the periodic direction used in the calculations. (b) Band structure of the ph-7-13-AGNR. Wave-function of (c) a longitudinally and (d) a transversally dispersing band and (e) a the cove state.

the character of the bands for the ph-7-13-AGNR is very similar to the 7-13-AGNR. In the ph-7-13-AGNR, VB and CB are dispersing in longitudinal direction (Figure 5.24c), as in the 7-13-AGNR. The transversal band (Figure 5.24d) extends onto the attached rings.

The cove state (Figure 5.24e) extends over the whole cove, which is twice the size for the ph-7-13-AGNR as compared to the cove region of the 7-13-AGNR. Interestingly, with a value of 3.34 eV with respect to the VBM, the energy of the cove state has decreased as compared to the non-phenylated 7-13-AGNR. This is

advantageous, because it might make these states accessible in transport experiments.

Hence, as just demonstrated, by just attaching phenyl-rings to the 13-part of the ribbon preserves the band gap in a range suitable for electronic applications, while decreasing the cove state energies. This highlights the great tunability of these nanoribbons. It is also conceivable to replace the phenyl-rings by pyrimidine, thus, introducing a dipole moment. This would give rise to electrostatic shifts of orbital energies, as has been demonstrated effectively, for example, in self-assembled monolayers[197] and graphene[198].

Of course, interconnecting these new ribbons will lead to NPG with a larger pore size. However, there is not a unique way to link these ribbons. In this work, we considered conformations with both phenyl-rings in meta or para configuration, denoted as meta-meta (MM) and para-para (PP), respectively, as well as a structure with one ring in meta and the other one in para configuration, from here on called para-meta (PM). Here, we do not study the 2D structure, but rather focus on how electronic properties change upon connecting two ph-7-13-AGNRs in different bond conformations.

In a first step, we systematically varied the dihedral (or twist) angles of the two rings connecting the ribbons with respect to the ribbon backbones. The atoms involved in the calculation of dihedral angles are indicated by colored rings in Figure 5.25. After calculating the energy as a function of the dihedral angles, we selected different structures with low energies to perform full structural relaxations. Figure 5.25 shows the energetically most favorable optimized structure for each phenyl-ring conformation. In all three cases, the rings connecting the ribbons are twisted significantly. Additionally, the outer rings of the MM and PM conformation get twisted as well, while they stay planar for the PP conformation. Generally, the twist of the rings leads to structural distortions in all three conformations, and they are strongest in the PM configuration. On the other hand, in the PP configuration the ribbons stay almost planar.

The band structures for the optimized geometries are shown in Figure 5.26 on page 94, along with the band structure of covalently linked 7-13-AGNRs. For the latter one (panel a), CB and CB+1 can be clearly distinguished in the band structure, and the same holds for VB and VB-1. These bands disperse in longitu-

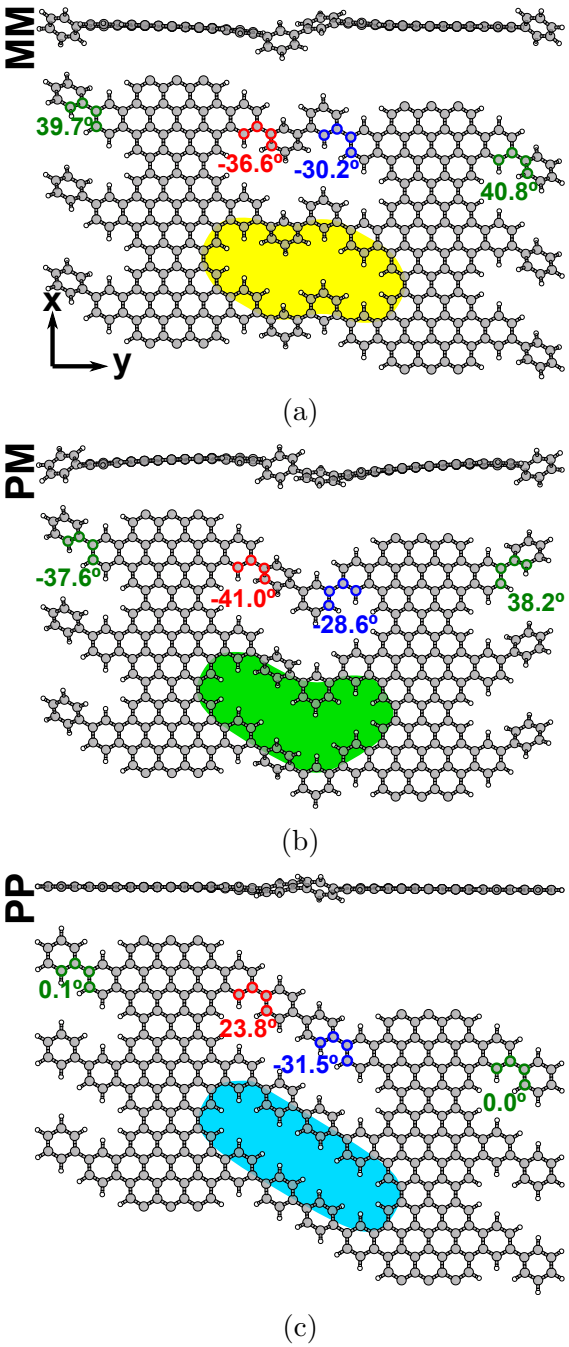

Figure 5.25: Side and top views of the relaxed structures of connected phenylated-7-13-AGNRs with different pore shapes (highlighted with different colors) as a consequence of different phenyl-configuration patterns: (a) meta-meta (MM), (b) para-meta (PM), and (c) para-para (PP). The atoms with colored frame indicate the atoms used to measure the twist angles of the phenyl-rings with respect to the 7-13-AGNR backbone and the numbers give the values of these angles.

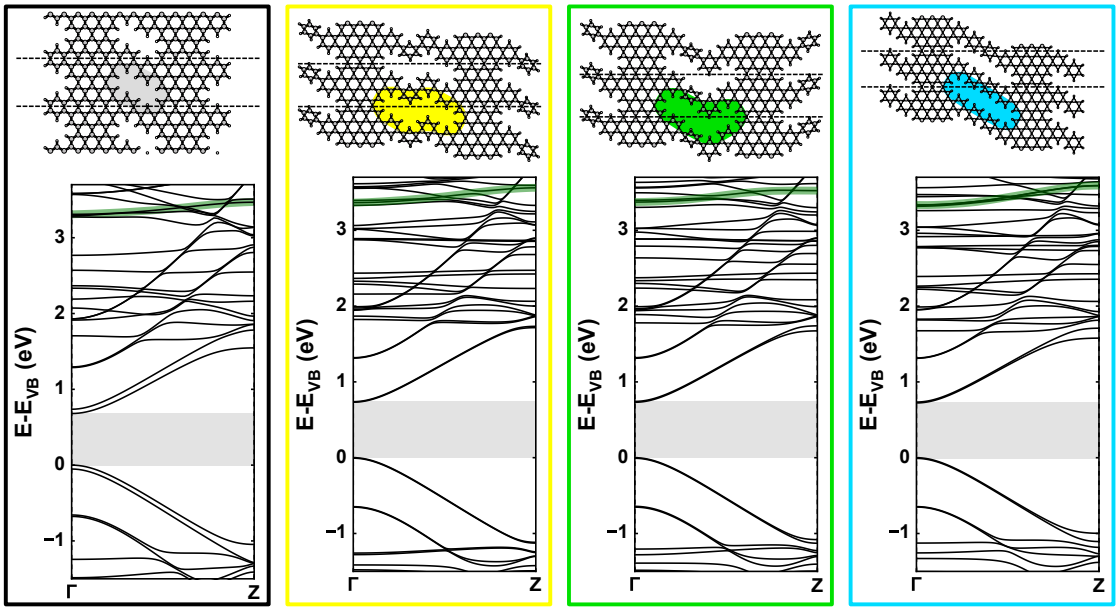

(a) 7-13-AGNRs (b) MM (c) PM (d) PP

Figure 5.26: Band structures of (a) two covalently linked 7-13-AGNRs and of the connected ph-7-13-AGNRs in (b) MM, (c) PM, and (d) PP configuration.

dinal direction on the backbones of both ribbons, and, as for a single 7-13-AGNR, they are localized on the 7-segment. The corresponding bands in the PP conformation show the same longitudinal dispersion behavior, but here CB and CB+1 are almost degenerate and only close to the Z-point they can be distinguished (Figure 5.26d). As an example for systems where the CB is localized on the backbones of both ribbons, the wave-function of the CB for the PP conformation is shown in Figure 5.27a. In contrast, for the MM and PM conformations CB and CB+1 are almost indistinguishable from the band structures (Figure 5.26b,c). Furthermore, while still dispersing in longitudinal direction, in these two configurations the CB is localized on the 7-segment of only one of the two ribbons, as can be seen from the wave-function of the MM's CB depicted in Figure 5.27b. Here, the CB is localized on the right ribbon, while the CB+1 is localized on the left ribbon (not shown here). The highest two valence bands exhibit the same localization pattern.

Figure 5.28 shows the lowest lying pore states for the phenylated double ribbon systems. Here, the pore states are confined in a similar way as for the NPG

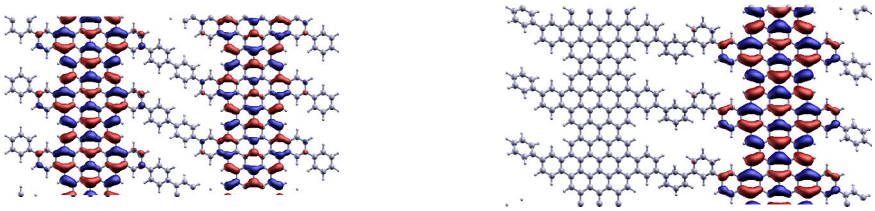

(a) PP, CB (b) MM, CB

Figure 5.27: Iso-surface plots of wave-functions at Γ-point for the conduction bands of (a) the PP and (b) the MM conformation. The iso-value for these plots is 0.05 $Å^{-3}$.

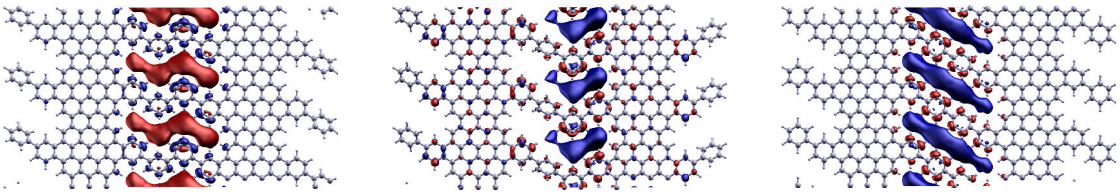

(a) MM, E-E_{VB}=3.36 eV (b) PM, E-E_{VB}=3.37 eV (c) PP, E-E_{VB}=3.32 eV

Figure 5.28: Iso-surface plots of wave-functions at Γ-point of the bonding pore states of (a) the hydrogen bond 7-13-AGNR double ribbon, and the phenylated 7-13-AGNR double ribbons in (b) MM, (c) PM and (d) PP bonding configuration. The iso-value for these plots is 0.05.

discussed above, except for the PM bond configuration (see Figure 5.28b). Here, it fills only half the pore. This could either be an artifact of the iso-surface plot or be related to a small shift in the energy of the pore state in each of the subregions. For the double ribbons based on the ph-7-13-AGNR the pore states have all more or less the same energy, namely 3.36 eV (MM), 3.37 eV (PM), and 3.32 eV (PP), all measured with respect to the VBM. Thus, energies of the pore states of these ribbons do not change much compared to a single ph-7-13-AGNR.

Summarizing, while further studies of the ribbons shown in this section are necessary, our preliminary results indicate how the ribbon's edge morphology can influence the electronic properties and the energies of cove and pore states. Our results suggest that the energy of the cove state is lower for the ph-7-13-AGNR than for the 7-13-AGNR, and that connecting two ph-7-13-AGNRs does not lead to a further decrease of the cove state energy.

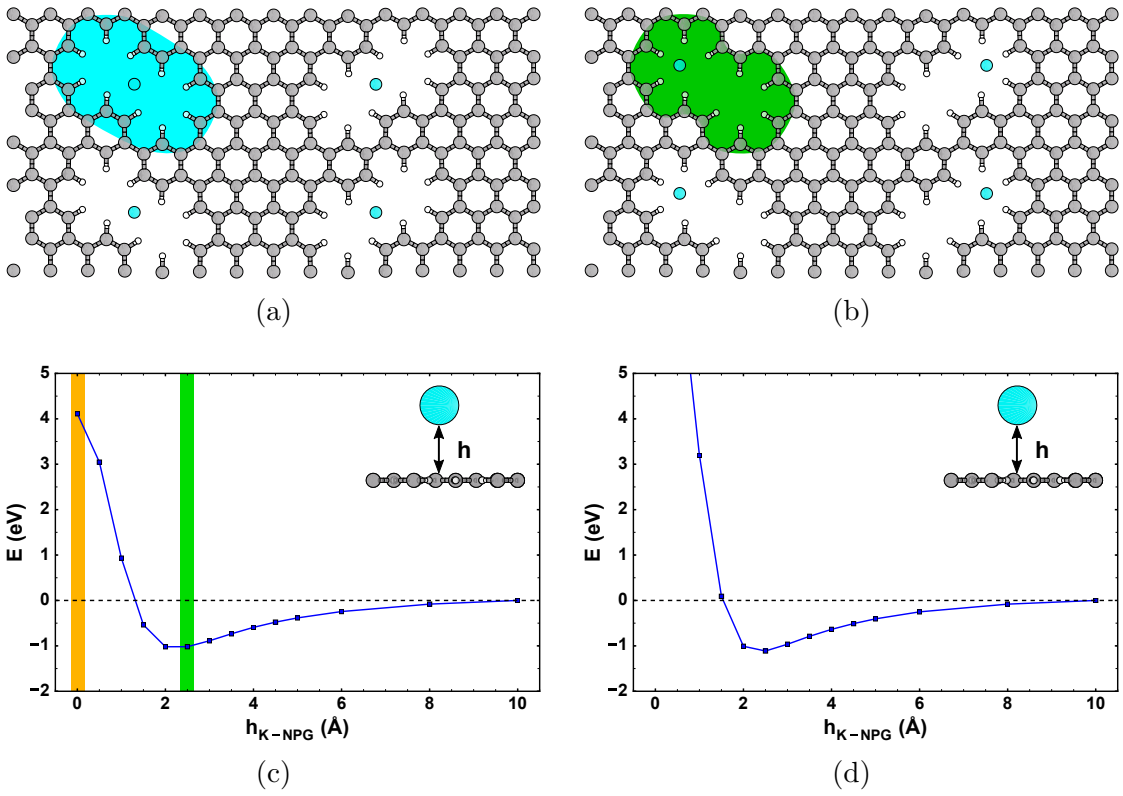

Figure 5.29: Adsorption positions of the K atom in the (a) center and (b) cove region of the pore. (c) and (d) show the energy as a function of the K height above the NPG for the adsorption positions in (a) and (b), respectively. Insets show the definition of the height h_{K-NPG}. Red and blue areas in (c) indicate the heights for which the system was analyzed in more detail.

5.5 Influence of potassium adatoms

An alternative route to make the cove or pore states accessible in transport measurements is by the influence of external perturbations, like atoms or ions. Such external species can strongly modify the electronic structure of carbon based materials via doping mechanisms[192, 199]. Here, we study the influence of potassium atoms on the pore states of the NPG.

We have studied the adsorption of K atoms at the center of the pores and at a lower symmetry position away from the pore center, as depicted in Figure 5.29a,b. For these two positions, we calculated the total energy as a function of the height of the K atom above the NPG (see Figure 5.29c,d). At both sites, the minimum

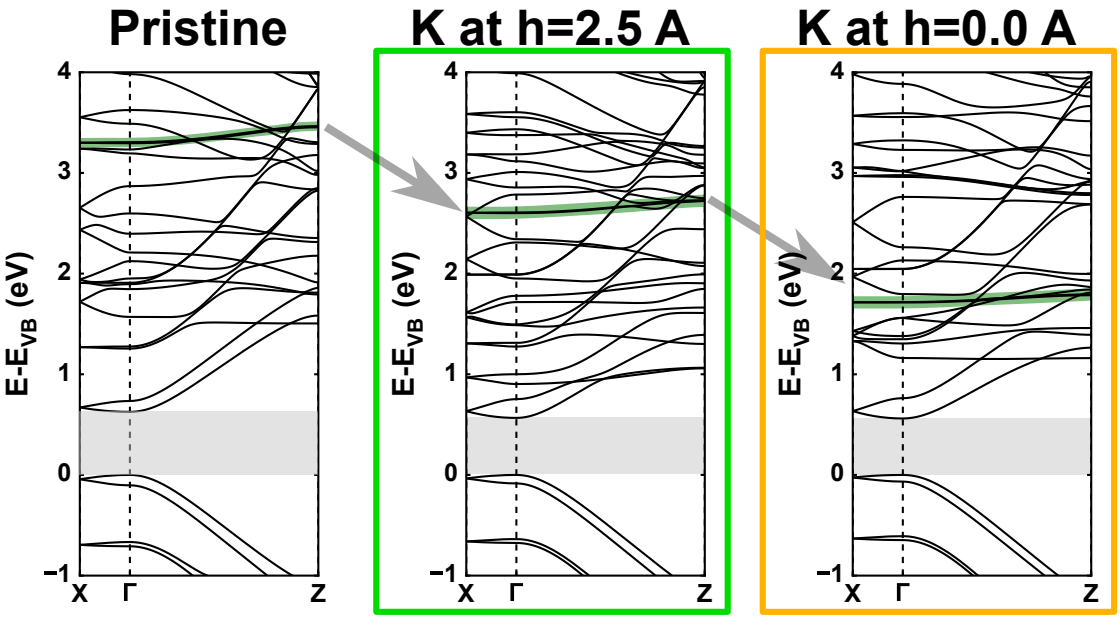

(a) (b) (c)

Figure 5.30: Band structures for the NPG (a) without K atom, and with the K atom at the center position at heights of (b) 2.5 Å and (c) 0.0 Å. Green lines indicate the lowest lying pore states.

energy occurs at a height of the K atom of ∼2.5 Å above the NPG. Thus, we decided to do a more detailed analysis for the systems with the K atom adsorbed at 2.5 Å and 0.0 Å. The height of 2.5 Å also corresponds to a distance a bit further away from the NPG than the pore state wave-function maximum. Qualitatively the differences in the electronic properties between the two adsorption sites are rather small, so we will only present the results for the center position here. By comparing the clean NPG (0% K adsorption) with one where we put K atoms in both pores of the unit cell (100% K adsorption), we can study the extreme adsorption cases.

Figure 5.30 shows the band structures for the pristine NPG, and for NPG with the K atom at the center position at heights of 2.5 Å and 0.0 Å. The green lines indicate the bands corresponding to the pore states. Clearly, the pore state gets significantly shifted down in energy when the distance between K and NPG is reduced. Apart from shifting down the energy of the pore state with respect to the

valence band maximum (VBM), K adsorption also slightly decreases the band gap to values of 0.57 eV and 0.56 eV for K at heights of 2.5 Å and 0.0 Å, respectively. Figure 5.31 shows the LDOS maps for the clean NPG (top panel) as well as NPG with K at a height of 2.5 Å (middle panel) and 0.0 Å (bottom panel). Here, the pore states can be clearly identified. As already seen in the band structures, it is clear that the pore state energy gets smaller the closer the K atom is to the NPG. At a height of 2.5 Å the 4s states of the K atoms can also be clearly identified, but are not visible anymore for K at 0.0 Å.

From these result it is clear that the pore state can be shifted down in energy by bringing K atoms close to the NPG. When the K atom is adsorbed in the plane of the NPG (h=0.0 Å), the pore state energy is already quite close to the CB energy. But, from the energy curves as a function of the K height (Figure 5.29c), we deduce that this is not an energetically stable adsorption position and, therefore, it is unlikely to occur in experiments. On the other hand, in the experiments the K atoms will most likely lose their 4s electron and get ionized, which is expected to induce significant variation in the chemical and electronic properties of the system. This potentially changes the adsorption chemistry completely. Further investigation is required to get a clearer picture on the influence of K atoms and ion on the properties of the NPG, but our calculations indicate that the energy of pore states can be tuned by the interaction with the external species.

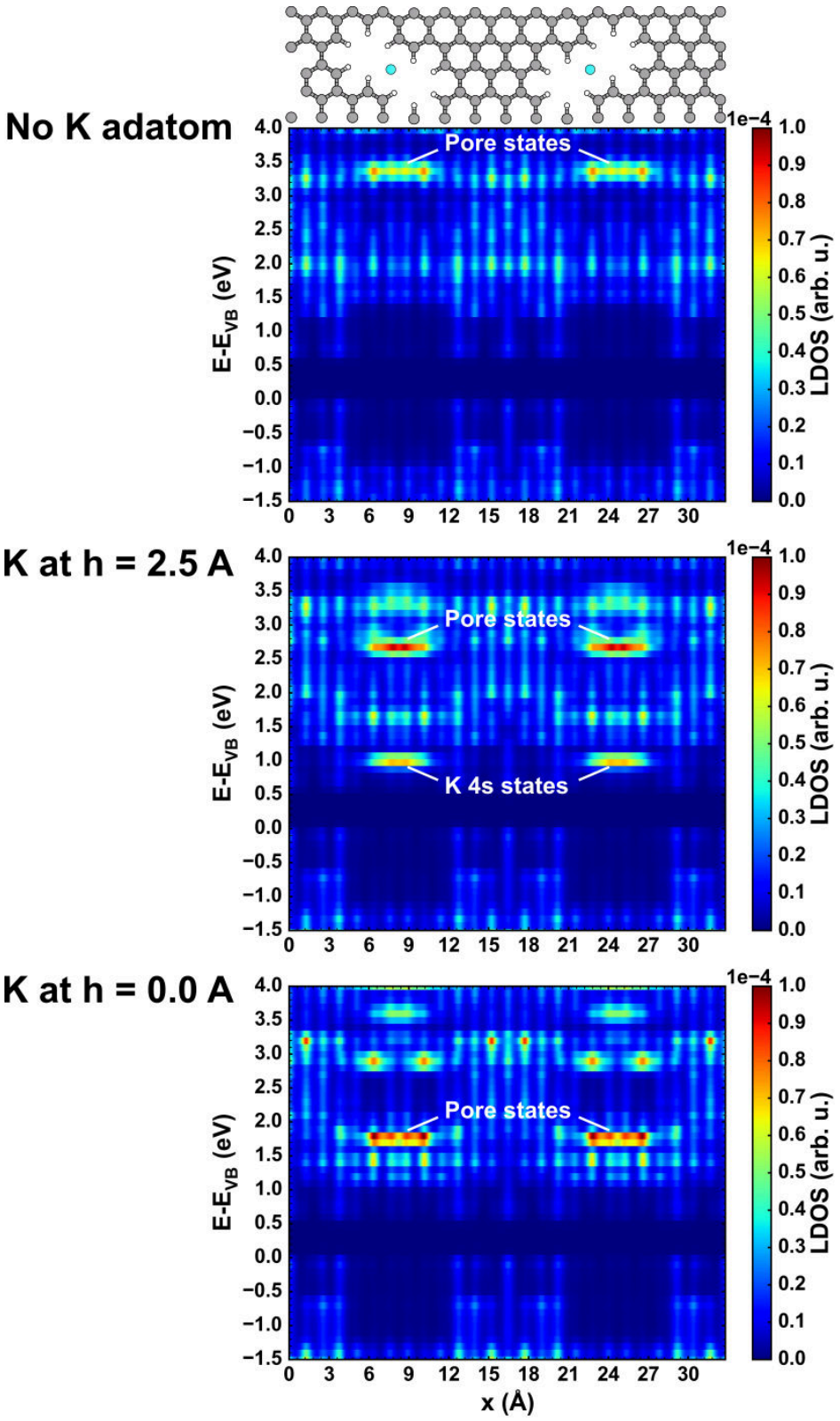

Figure 5.31: LDOS maps for NPG without and with K adsorbed at 2.5 Å and 0.0 Å. The structure above indicates the position of the C (gray) and K (cyan) atoms.

Chapter 6

Topological Insulator Bi_2Se_2Te: influence of chemical disorder

The combination of a topologically non-trivial electronic bulk structure and a strong spin-orbit coupling (SOC) gives rise to a 2D topological surface state (TSS) in 3D topological insulators (TIs)[26, 200, 201]. This linearly dispersing surface state is protected by time-reversal symmetry (TRS)[28–30], which also prevents backscattering[4]. The strong SOC is also responsible for the spin-momentum locking[202–204] which, together with a high electron mobility[205], makes TIs promising candidates for spintronics applications.

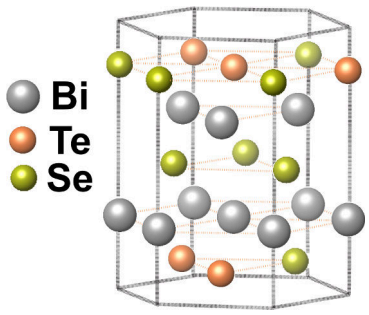

Figure 6.1: Bulk unit cell structure of the members of the $Bi_2(Se_\delta Te_{1-\delta})_3$ $(0 \leq \delta \leq 1)$ family.

Contacting TIs to magnetic materials or deposition of magnetic adatoms on the surface of a topological insulator could lead to breaking of TRS and, thus, destroy the TSS[206–208]. The challenge, aimed at the implementation of spintronic applications, is to find a topological insulator such that its surface state that is robust against magnetic distortions. One family of TIs which contains some candidates for such systems is $Bi_2(Se_\delta Te_{1-\delta})_3$, with δ assuming values between 0 and 1. The atomic structure of

this family consists of quintuple layers (QLs) which are bound by vdW forces. The structure and the unit cell of such a QL are shown in Figure 6.1. These QLs consist of 5 atomic layers, where the outermost and middle layers are made up by Te and Se atoms, in a ratio defined by δ, and the two layers in between them are comprised of Bi.

The end-compounds of this family, namely Bi_2Se_3 (δ=1) and Bi_2Te_3 (δ=0) have a bulk band gap of approximately 0.3 eV. Therefore, even at room temperature the TSS of these materials can be accessed[209, 210]. For the intermediate compounds ($0 < \delta < 1$), mainly structural and electronic properties have been studied so far[204, 211], but not the influence of magnetic adatoms on its TSS. In this work, by means of DFT calculations in combination with STM experiments, we study the structural and magnetic properties of clean and Co adsorbed Bi_2Se_2Te (δ=2/3) and compare its properties to the end-compound Bi_2Te_3.

6.1 Computational details

All calculations presented in this chapter were done using the VASP[76–79] code. We applied the projector augmented wave (PAW)[212, 213] method, and the PBE[53] flavor of GGA for the approximation of the exchange-correlation potential. Spin-orbit coupling (SOC) was included using a second variation method[214] as implemented in VASP[76–79]. To include vdW interactions, we applied the DFT-D2 method of Grimme[65]. We sampled the Brillouin zone using a Γ-centered 9x9x1 Monkhorst-Pack[144] k-point grid. For the plane wave cut-off energy we used 300 eV and we relaxed the forces down to 0.01 eV/Å.

Regarding structural parameters, we used a hexagonal 2x2 surface unit cell and a stack of 3 quintuple layers, as illustrated, e.g., in Figure 6.2a,b for Bi_2Te_3. Due to the high computational cost of these simulations, we checked structural and magnetic properties using a larger 3x3 unit cell only for a few selected systems. These two different cell sizes correspond to a Co coverage of 0.25 and 0.11 monolayers, respectively.

Besides, in order to account for the strong on-site Coulomb interactions of the localized electrons in Co adatoms, we applied a simplified model[90] of on-site Coulomb corrections for the d-orbitals of Co. Finding a reasonable value for U is

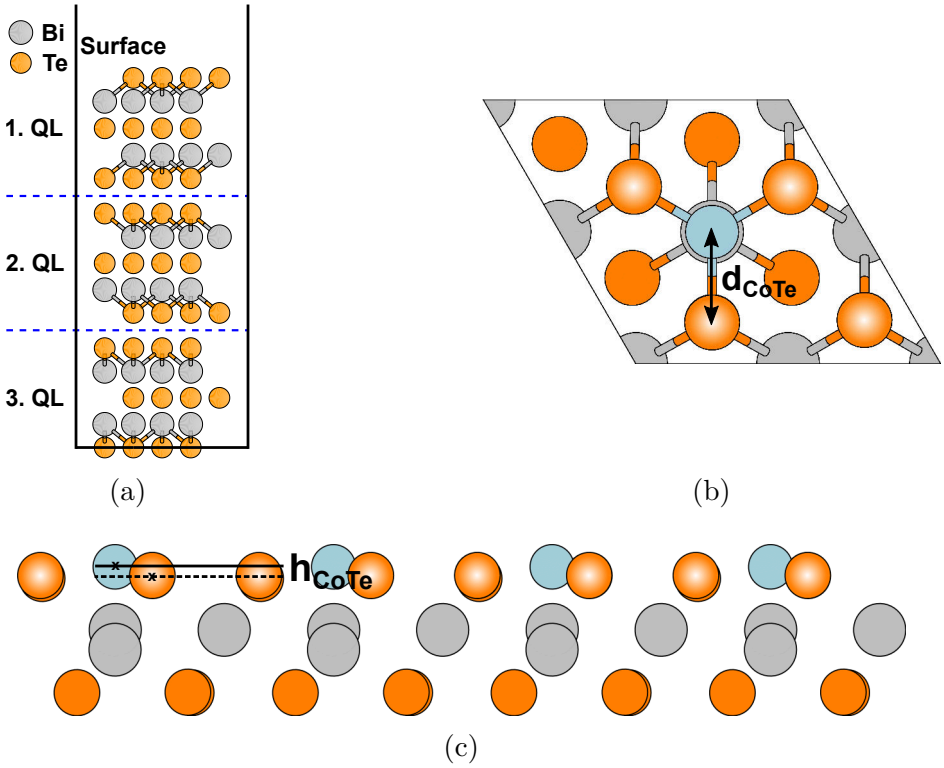

Figure 6.2: (a) Side view of the optimized DFT geometry of Bi_2Te_3. (b) Top view of the hexagonal 2x2 unit cell of Bi_2Te_3 with Co adsorbed at hcp site. The line with the arrow-heads at its ends defines the measurement of the distance between Co and Te (d_{CoTe}). (c) Side view of the three topmost atomic layers for Bi_2Te_3 with Co adsorbed. The lines define the height difference between Co and Te (h_{CoTe}).

not a simple task. Several ways of calculating the U parameter from first principles have been proposed[85, 215, 216]. We decided to estimate the value for U in a more empirical way. For this purpose we used Bi_2Te_3 with Co adsorbed on the fcc and hcp sites as a reference material. After relaxing these materials with different U values, we evaluated the distances and heights of the Co atom with respect to the topmost Te layer, as they are defined in Figure 6.2b,c.

For Co adsorbed on the hcp site and U values of 0 eV and 1 eV the calculations yield non-magnetic solutions, i.e., the total magnetic moment of Co is virtually zero. Such a strong quenching of the Co magnetic moment is unexpected in view of previous experimental and theoretical reports in the literature[217, 218]. The results of structural optimizations for U=2 eV are listed in Table 6.1. For this

Table 6.1: Co heights (h_{CoTe}), Co-Te distances (d_{CoTe}), and Co total magnetic moments (μ_{tot}) after structural relaxations with U=2 eV for different Co adsorption sites. The arrow (↑) indicates that the magnetic moment is pointing primarily out-of-plane.

U (eV)	Co site	h_{CoTe} (Å)	d_{CoTe} (Å)	μ_{tot} (μ_{Borh})
2	fcc	−0.83	2.63	1.39↑
2	hcp	0.10	2.57	1.88↑

U value, the magnetic moments of the Co adatom is not quenched and out-of-plane. Furthermore, our relaxed geometries are very similar to structures with Fe adsorbed on Bi_2Te_3 and obtained with a U value of 2.2 eV[219]. Thus, we applied this U value in all of our following calculations.

6.2 Structural properties of clean Bi_2Se_2Te

First, we studied the structural properties of clean Bi_2Se_2Te. Figure 6.3a shows a high-resolution scanning transmission electron microscopy (STEM) image of Bi_2Se_2Te. Here, the atomic layers and the vdW gaps between the quintuple layers are clearly visible. From the STEM measurements it is possible to extract the Z-contrast profiles for different regions, where Z denotes the atomic number. The contrast profiles for the areas indicated by dashed lines in Figure 6.3a are shown from Figure 6.3b to 6.3f. From these profiles, the Se/Te ratio in the outermost and middle atomic layer of each quintuple layer can be estimated. This analysis reveals that the middle layer consists solely of Se atoms, while in the outer atomic layers the ratio between Se and Te is 50% to 50% and no long range order is found. Earlier measurements of this material arrived at the same conclusion regarding its structural composition[211].

In the light of these experimental results, we decided to model this material based on a Bi_2Se_3 crystal, which is one of the end-compounds of this TI family. Besides, since the magnetic and structural properties of the Co adatom are mainly influenced by its local chemical environment, we simulated the Bi_2Se_2Te surface by substituting Se atoms surrounding the Co atom by Te. Simulations with 1, 2, and 3 Te atoms in the surface layer were carried out. A schematic depiction of

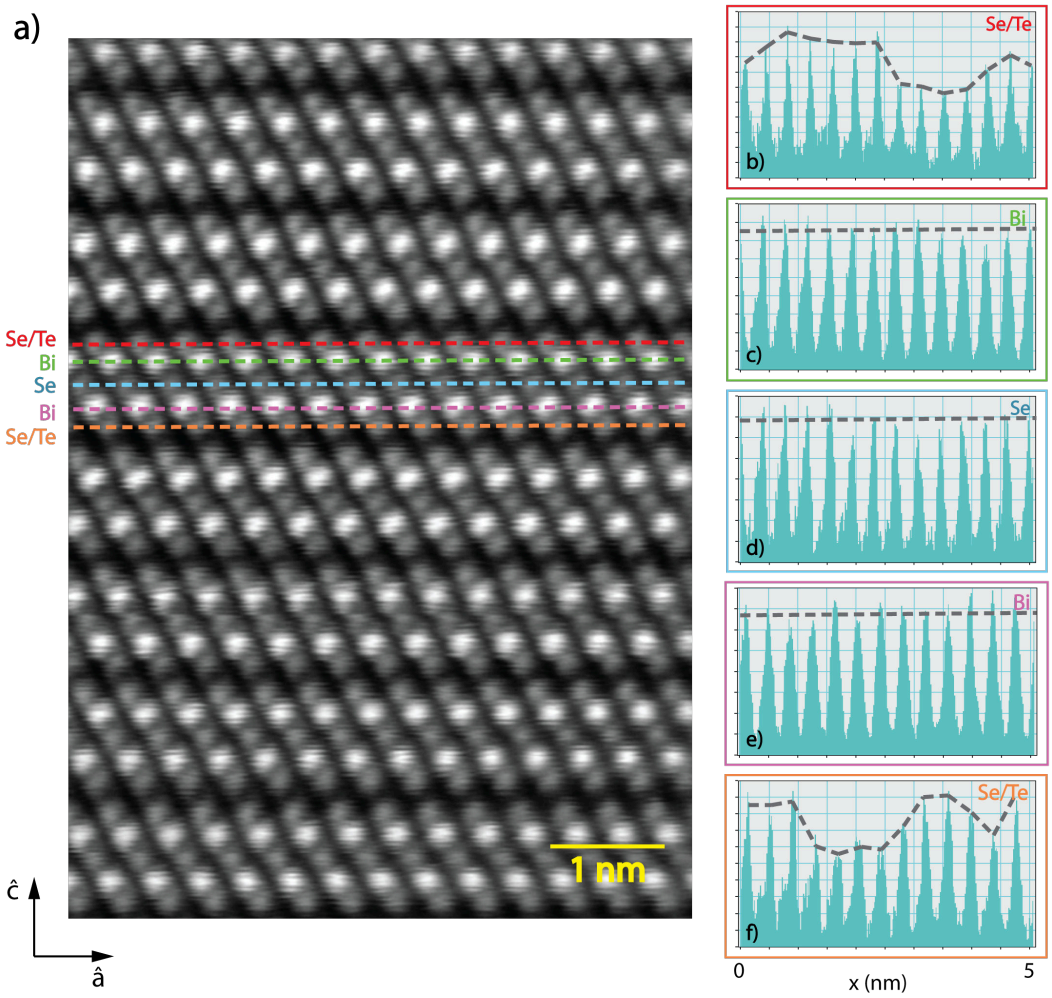

Figure 6.3: (a) STEM image of the Bi_2Se_2Te structure. (b) to (f) show contrast profiles of different regions. Reprinted with permission from M. Carmen Martínez-Velarte et al., Nano Lett. 2017, 17, 4047-4054. Copyright 2017 American Chemical Society.

our setup for these DFT calculations is shown in Figure 6.4. With this strategy on how to simulate Bi_2Se_2Te surface, we investigated the structural and magnetic properties of this material upon Co adsorption.

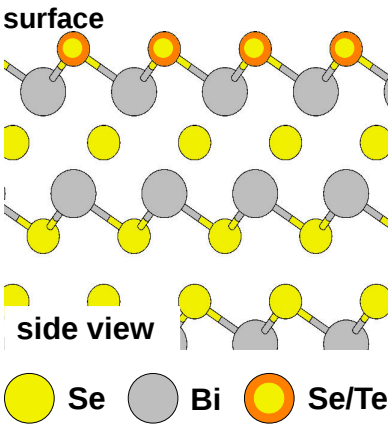

Figure 6.4: Structural setup for the computational treatment of the Bi_2Se_2Te surface.

6.3 Cobalt atoms adsorbed on Bi_2Se_2Te surface

Next, we studied the structural evolution of the Bi_2Se_2Te surface upon Co adsorption as well as the magnetic properties of the adatom. In our STM images we can distinguish three apparent shapes for Co atoms adsorbed on Bi_2Se_2Te with a coverage of 0.015 monolayers (see Figure 6.5a). A statistical analysis of such STM topographies has been performed, including approximately 1000 Co atoms. This analysis shows, that 99% of the Co atoms on Bi_2Se_2Te fall into one of two categories (see Figure 6.5b). The atoms of the first category, termed Co_b, show big round protrusions in the STM image and have apparent heights between 40 pm and 90 pm. Co atoms of the second category appear smaller in the STM topography and with apparent heights between 20 pm and 30 pm. These atoms are denoted as Co_s. Both types of atoms are found in non-equivalent distorted adsorption sites and appear with almost the same frequency in the STM images. Co_α atoms only appear with a probability of 1%.

We employed the model structure of Bi_2Se_2Te, outlined in the previous section, to obtain the structural properties of Co adsorbed on its surface. Initially, we positioned the Co adatom at the high symmetry sites fcc and hcp of the surface. The results of the relaxations are shown in Figure 6.6 (page 108) and Table 6.2 (page 108). When substituting one of the Se atoms surrounding the Co atom by Te, there are three equivalent possibilities to do so. The same holds for replacing

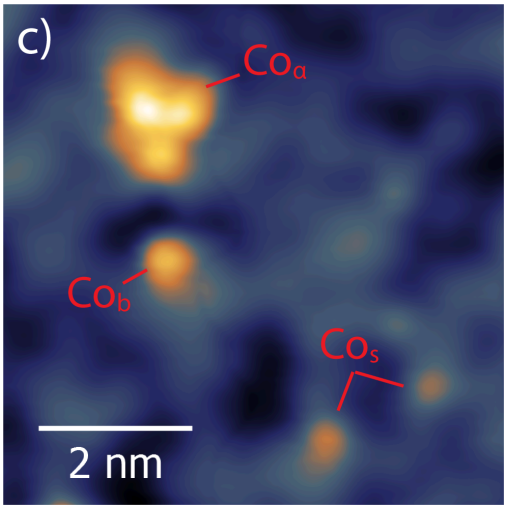

(a)

Adatom	Appearance probability	Apparent height (pm) at V_{bias} = −600 mV	
Co_α	1%	70	
Co_b	43%	40-90	
Co_s	56%	20-30	

(b)

Figure 6.5: (a) STM image of Co in Bi_2Se_2Te at V_{bias}=−0.65 eV. (b) Appearance probabilities, apparent heights, and schematic illustration of corresponding adsorption sites for Co on Bi_2Se_2Te. In the last column, purple circles depict Se and Te surface atoms, red circles indicate Co atoms, and black arrows means that these Co atoms were moving away from the high-symmetry adsorption position. Adapted with permission from M. Carmen Martínez-Velarte et al., Nano Lett. 2017, 17, 4047-4054. Copyright 2017 American Chemical Society.

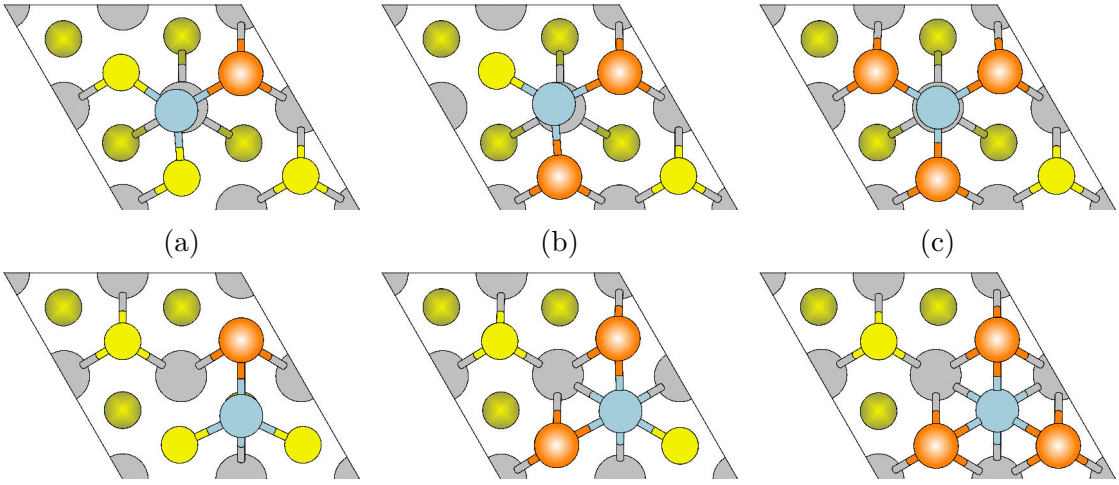

Figure 6.6: Relaxed geometries of the Bi_2Se_2Te surface with (a) 1 Te, (b) 2 Te, and (c) 3 Te surrounding the Co atom adsorbed at the hcp site. (d), (e), and (f) show the corresponding geometries for Co adsorbed at the fcc site.

Table 6.2: Co heights (h_{CoTe}), Co-Te distances (d_{CoTe}), and Co total magnetic moments (μ_{tot}) after structural relaxations for different numbers of Te and different Co adsorption sites. The arrows indicate that the magnetic moment is pointing primarily out-of-plane (↑) or in-plane (→).

# of Te	Co site	h_{CoTe} (Å)	d_{CoTe} (Å)	d_{CoSe} (Å)	μ_{tot} (μ_{Borh})
1	hcp	0.10	2.61	2.38	1.89↑
2	hcp	0.14	2.57	2.35	1.87↑
3	hcp	0.19	2.52		1.80↑
1	fcc	−0.01	2.63	2.40	1.92↑
2	fcc	−0.35	2.64	2.41	1.80→
3	fcc	−0.71	2.57		1.42→

two of the Se atoms, while there is only one way to replace all three Se atoms around a Co adsorption site. Thus, the results shown in Figure 6.6 and Table 6.2 correspond to 14 different adsorption scenarios (7 per adsorption site).

From Figure 6.6 it is clear, at least for the hcp adsorption site, that for 1 Te and 2 Te the Co atom moves away from the high symmetry position, while it is not displaced when surrounded by 3 Te atom. This is also the case for the fcc adsorption site. While this is difficult to see from Figure 6.6, it becomes evident

when comparing the Co-Te and Co-Se distances for these systems in Table 6.2. Besides, from these results, it is clear that in all cases the Co-Te distance is significantly larger than the Co-Se distance. This can be attributed to Te having a larger ionic radius than Se, which generally results in larger bond lengths. Hence, if a Co atom is surrounded by atoms of both species, one would certainly expect it move away from the high-symmetry position. Our DFT calculations confirm the STM measurements described above. Furthermore, our combined experimental and theoretical results suggest that Co_s is pushed away from one Te atom towards two Se atoms and Co_b is surrounded by two Te atoms and shifted closer to one Se atom.

Table 6.2 also lists the values and directions (out-of-plane $\uparrow$ or in-plane $\rightarrow$) of the magnetic moments of the Co atoms upon adsorption. In none of the cases the magnetic moment is significantly quenched, and only in four out of 14 adsorption scenarios its main contribution is in-plane. Additionally, we performed preliminary calculations of the magnetic anisotropy for these systems and found its value to be of the order of 1 meV/atom. Nevertheless, in the experiments a 3 T magnetic field perpendicular to the TI surface is applied, which ensures that in all cases the adatom will have a magnetic moment perpendicular to the surface. The direction of the magnetic moment is insofar of importance as an in-plane magnetic moment might mask backscattering due to breaking of TRS[206].

We cross-checked the structural and magnetic properties for the systems with 1 Te for a larger 3x3 unit cell, which corresponds to a coverage of 0.11 monolayers Co (while the coverage in the 2x2 unit cell is 0.25 monolayers). Apart from a small reinforcement of the out-of-plane component of the magnetic moments, the results for the larger unit cell are essentially the same as for the smaller one. This means that, further extending the calculation unit cell will not lead to qualitatively different magnetic anisotropy and, that no reorientation of the magnetic moment is to be expected for low coverages as in the experiments (about 0.015 monolayers).

An interesting experimental way to get information about backscattering is to extract so-called quasi-particle interference (QPI) patterns from STM measurements[220]. This works as follows[220]: when the surface state of a TI gets scattered at a defect, for example a impurity or adatom, it interferes with itself, producing a standing wave pattern in the LDOS at the surface. These oscillations

in the LDOS can be measured and analyzed via STM. From the STM images the wave length of the standing waves can be calculated and transformed from real space to momentum space via a fast Fourier transform. The resulting patterns directly represent the scattering intensity as a function of momentum.

In the case of TI surfaces, due to TRS, the most important direction for backscattering is the ΓK-direction[202, 221]. Scattering in ΓM-direction on the other hand is mainly ascribed to scattering processes originating from the warping of the Dirac cone[202, 222]. This warping of the Dirac cone can be seen from the band structure of Bi_2Te_3 in Figure 6.7. From this figure it is evident, that the warping of the Dirac cone occurs at lower energies in the ΓM-direction (∼0.2 eV) compared to the ΓK-direction (∼0.6 eV).

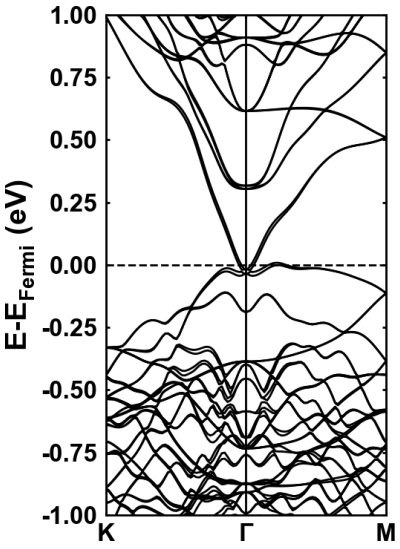

Figure 6.7: Surface band structure of Bi_2Te_3 calculated in a 2x2 unit cell.

The QPI patterns for the clean and Co adsorbed Bi_2Te_3 and Bi_2Se_2Te surfaces are depicted in Figure 6.8 (Co coverages were 0.012 monolayers for Bi_2Te_3 and 0.015 monolayers for Bi_2Se_2Te). While all QPI patterns show the sixfold symmetry, only in the image for the clean Bi_2Te_3 no warping of the Dirac cone is observed. That is, only for the clean Bi_2Te_3 surface the QPI pattern has a circular shape. For the pristine surfaces of both materials we observe that the scattering intensity in ΓK-direction is very low, indicating the absence of backscattering in this surface. The observation of warping of the Dirac cone in QPI patterns, of course, strongly depends on the position of the Dirac point and the bias applied in the experiments. When Co adatoms are adsorbed on Bi_2Te_3, a high scattering intensity emerges in ΓK-direction, demonstrating the opening of channels for backscattering. Remarkably, for the Bi_2Se_2Te surface, even upon adsorption of Co backscattering cannot be observed, as is evident from the QPI pattern in the right lower panel of Figure 6.8. The lack of backscattering can be ascribed to a weakened hybridization between the Co adatom and the TSS, caused by the Co's movement away from the high

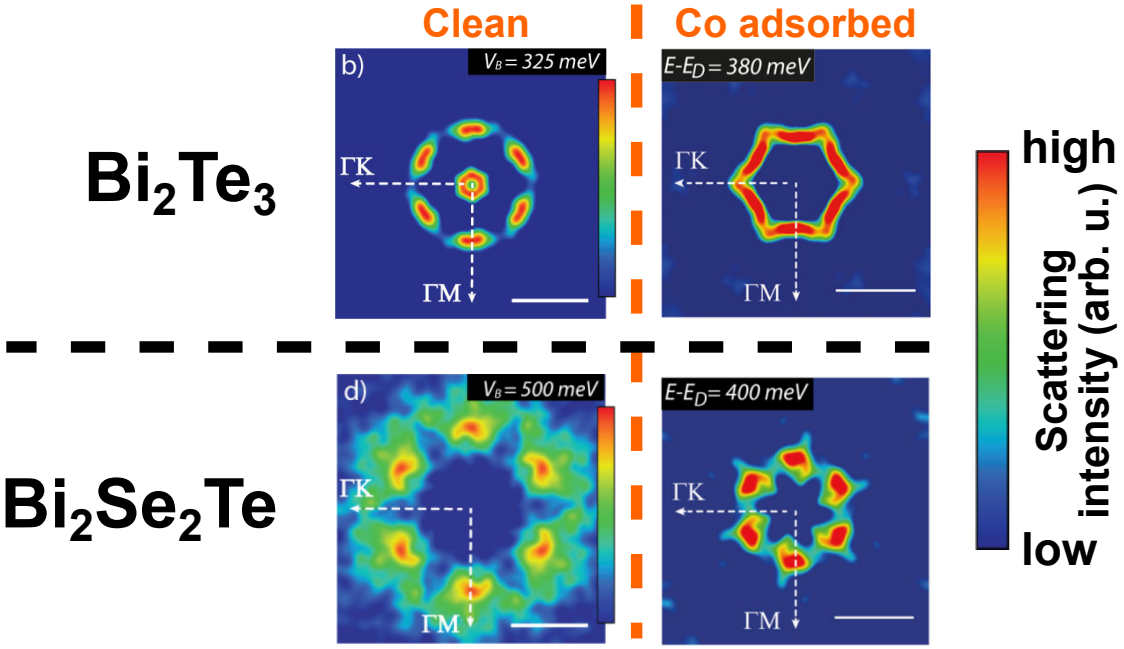

Figure 6.8: QPI patterns for clean (left panels) and Co adsorbed (right panels) Bi_2Te_3 (upper panels) and Bi_2Se_2Te (lower panels) surface. The Dirac point energies for the clean surfaces were: -131±14 meV in Bi_2Te_3 and -154±11 meV in Bi_2Se_2Te. Co adsorption shifted the Dirac cones down by about 100 meV for both surfaces. Adapted with permission from M. Carmen Martínez-Velarte et al., Nano Lett. 2017, 17, 4047-4054. Copyright 2017 American Chemical Society.

symmetry adsorption position in most surface configurations.

In conclusion, the results of the combined computational and experimental investigation demonstrate the stability of the Bi_2Se_2Te surface state against magnetic impurities. We have shown, that the TSS of Bi_2Se_2Te is robust against the same perturbations that lead to TRS breaking and backscattering in Bi_2Te_3. The disordered adsorption geometry of the Bi_2Se_2Te surface prevents the magnetic states of Co from hybridizing with the TSS, and, this way, preserving TRS. This is expected to hold as well for other ternary TIs with chemical disorder on the surface.

Chapter 7

Conclusions

This thesis presents a set of contributions to the field of 2D Dirac materials, which have emerged as promising candidates for future nanoelectronics. The electronic and transport properties of various graphene-based nanostructures and surfaces of topological insulators reported in this work, provide further insight into the functionalities of this class of materials.

The first two chapters are focused on the description of the theoretical methodology. For the electronic structure simulation, DFT is the method of choice. To calculate the transport properties, we employ an extension to DFT based on NEGF. Within this approach, we report on a tool for the calculation of multi-terminal eigenchannels, which has been implemented within the frame of this thesis.

Chapter 4 was dedicated to computational studies of graphene metal contacts. In the first part of this chapter, we studied the influence of graphene edge passivation on the transport properties of metal-graphene side contacts, considering Ni and Au as metal electrodes. We found that the resistance of the unpassivated contacts is of the same order of magnitude regardless of the metal type. On the contrary, the passivation of the graphene edge affects the electrical characteristics of the contacts differently depending on the metal. As such, while for Ni-based interfaces the contamination of the graphene edge has rather little influence on the contact resistance, it drastically increases the contact resistance for these interfaces

The second part of **chapter 4** was dedicated to an extensive study of metal graphene edge contacts. For this purpose, we used Ni, Cr, Ti, and Au as metal

electrodes, and F, F2 and O as possible contaminants. To gain understanding on the evolution of these interfaces, a detailed analysis of the the forces induced by the metal on the atoms of the graphene was carried out, which allowed us to conclude that the contact reactivity depends in an intricate way on both metal and graphene edge contamination. We further showed that, as for the lateral contacts, all clean metal-graphene side contacts exhibit resistance values of the same order of magnitude. On the other hand, contamination of the graphene edges leads to a significant, strongly metal dependent increase of the contact resistance. Interestingly, the Cr-based contacts are found to display the best contact properties, as found experimentally. Altogether, our results provide useful insight into the mechanisms leading to device-to-device variations and might be of relevance for the design of improved contacts.

In chapter 5, we characterized 7-13-AGNRs and the nanoporous graphene (NPG) derived from them, experimentally and computationally. Regarding 7-13-AGNRs, our DFT calculations showed that they possess three types of bands. On one hand, we found longitudinal bands dispersing along the periodical direction of the ribbon, and transversal bands localized within the 13-carbon atom-wide stripes. Besides, we report on the emergence of some novel states localized in the vacuum region within the cove. These states have been also observed experimentally by STM, and are related with the image potential at the graphene edge.

Moreover, our calculations in combination with high-resolution STM images confirmed that the ribbons can be linked covalently to each other, forming NPG. This new graphene based material has a semiconducting gap of about 1eV, and its electronic characteristics are closely related to the parent 7-13-AGNRs. In particular, the longitudinal bands remain unperturbed in the NPG, while the transversal bands disperse across neighboring ribbons and give rise to a 1D band. This in-plane anisotropy of the bands has a clear impact on the conductance properties of the material, as shown by our conductance calculations, and might be exploited in different applications, e.g. in FETs. Moreover, when the nanoribbons are connected, the cove states of the 7-13-AGNR interact giving rise to pore states in the NPG. The presence of these confined states makes NPG very attractive for its use in molecular sensors.

Finally, **chapter 6** summarizes a combined DFT and STM study about the in-

fluence of chemical disorder on the properties of the topological insulator Bi_2Se_2Te, aimed at determining the robustness of its TSS against magnetic perturbations. Studying the structural evolution of these surfaces upon Co adsorption allowed us to confirm the analysis of STM topographies, which indicated that the majority of Co adatoms are displaced from the high-symmetry positions. Besides, our calculations show that the magnetic moments of the Co atoms on Bi2Se2Te are not quenched and point out-of-plane for most of the adsorption conformations. These results suggest a weak hybridization between the Co adatoms and the surface state of this material and, as a result, the survival of its TSS.

Appendix A

Metal-graphene 2D contacts: k-resolved transmissions

Here, the spin- and k-resolved transmissions for the functionalized Ni (Figure A.1) and all the Au (Figure A.2) contacts are shown.

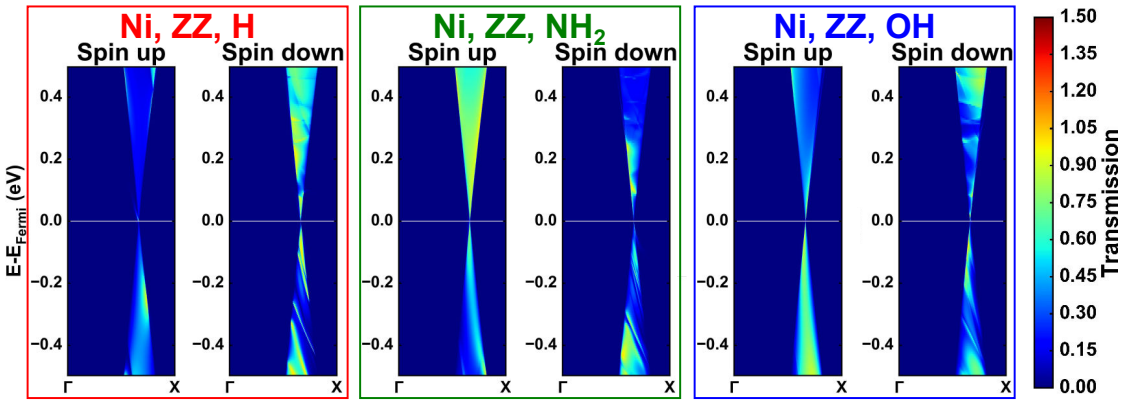

Figure A.1: Spin-resolved transmission as function of energy and k_x for the Ni contacts with unreconstructed graphene edge and H (red frame), NH_2 (green frame), and OH (blue frame) passivation.

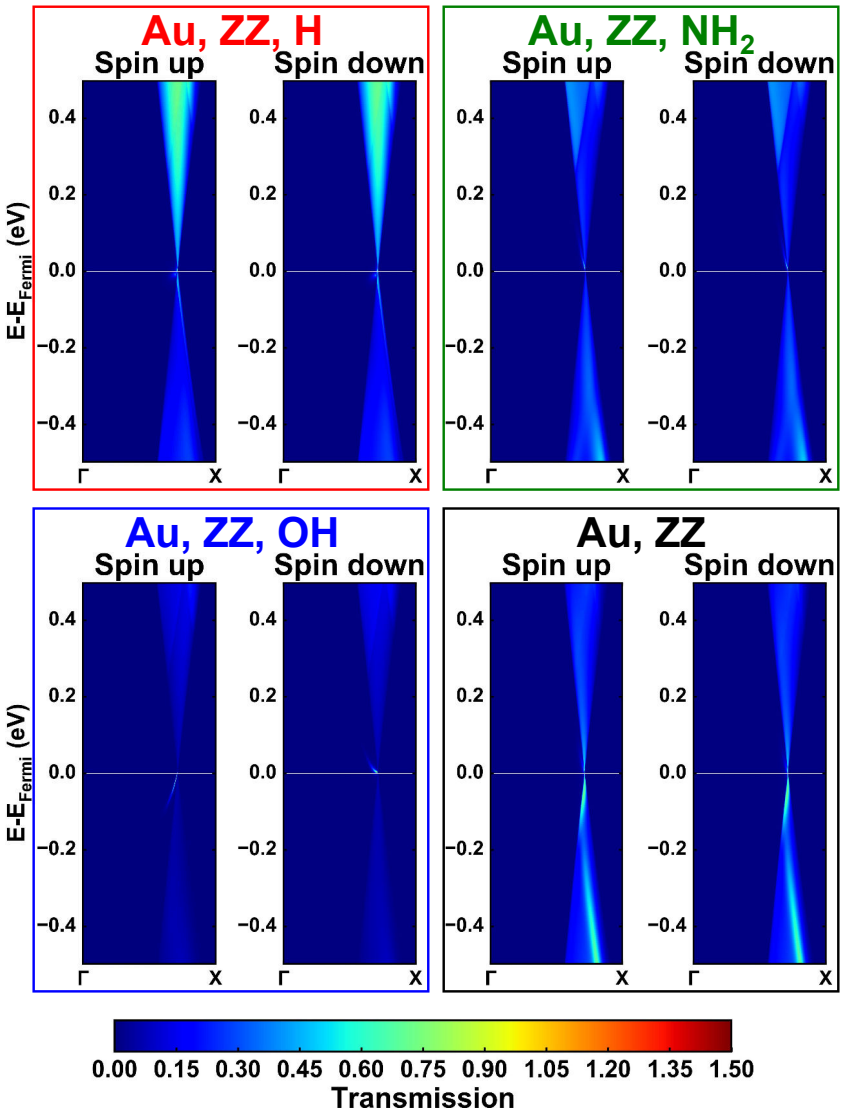

Figure A.2: Spin-resolved transmission as function of energy and k_x for the Au contacts with unreconstructed graphene edge and H (red frame), NH_2 (green frame), and OH (blue frame) passivation.

Appendix B

Scanning tunneling microscopy (STM)

In the early 80s, Binning and Rohrer presented a new type of microscope relying on the strong distance dependence of a tunnel current of electrons, which they named scanning tunneling microsopy (STM)[39]. The tunnel current between a tip and a surface (both metallic) can be approximated by[39],

$$I(z) \propto \frac{V}{z} e^{-A\sqrt{\phi}z}, \tag{B.1}$$

where A is a constant ($\approx$1.025 $\mathrm{eV}^{-1/2}\mathrm{\AA}^{-1}$ for vacuum[39]), ϕ and V are the average of the work functions of the surface and the tip and the voltage applied between the two, respectively, and z is the distance of the tip to the surface.

The STM can be operated either in constant current or constant height mode, schematically illustrated in Figure B.1. In both modes, the tip is moved over the surface, making one measurement at every point in space, i.e., the surface is scanned. In constant current mode, the current is kept constant by varying the distance between the tip and the surface while scanning the surface. The change in the distance is recorded for each point in space and gives a topography map of the surface. On the other hand, in constant height mode, the tip is kept fixed at a certain height and the current is measured. Then, by applying Equation B.1 or more advanced models, like the Tersoff-Hamann approach[223, 224], the topology map can be constructed.

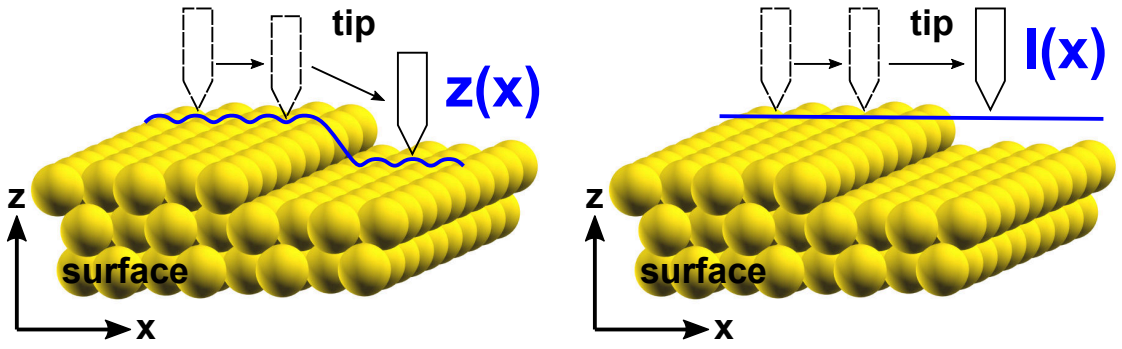

(a) (b)

Figure B.1: Schematic illustration of (a) constant current and (b) constant height operation modes of the STM.

It has been demonstrated experimentally, that functionalization of the STM tip with molecules can significantly enhance the resolution of the topography maps[225–229]. It has been suggested that the enhancement of the resolution has to do with the states involved in the tunneling process[229]. The Tersoff-Hamann approach works reasonably well for metallic tips, where the tip wave-function is dominated by s-states[223, 224]. For such tips, an STM image resembles the local density of states[229, 230]. On the other hand, in tips functionalized with molecules, the p-states are dominant. Here, STM images are expected to represent the spatial derivatives of the sample wave-functions[229–231].

An STM can also be used for probing the local density of states (LDOS) at a given point of a sample. This is done in constant height mode by varying the tip-sample voltage and recording the current. In this type of measurement the tip is not moved at all, and it is called scanning tunneling spectroscopy (STS).

Appendix C

7-13-AGNR: Extended SIESTA basis set

Listing C.1 shows how to define the extended basis set in SIESTA[81] (a more detailed description can be found in the SIESTA[81] manual). As cut-off radii for the additional basis functions we used 10 Bohr.

Listing C.1: Definition of extended basis set in SIESTA

```
%block PAO.basis
C 4
n=2 0 2
0.000    0.000
n=2 1 2 P
0.000    0.000
n=3 0 1
10.000
n=3 1 1
10.000
%block PAO.basis
```

Resumen

El gran avance en los métodos de producción acaecido en las últimas décadas, ha permitido la minituarización de los dispositivos electrónicos hasta alcanzar tamaños de transistores de silicio de unos poco nanometros. Sin embargo, algunos procesos físicos que emergen a la nanoescala, e.g. el efecto cuántico de túnel, dan lugar al incremento de las corrientes de fuga y corrientes en modo "off" y, por tanto, hacen que sea muy difícil reducir aún más su tamaño. De hecho, es muy probable que pronto se alcance el límite de miniaturización de los dispositivos basados en silicio. Por este motivo, la busqueda de materiales alternativos con alto rendimiento electrónico se ha intensificado de forma espectacular durante los últimos años. En particular, el descubrimiento y desarrollo de nuevos materiales de Dirac bideminsionales (2D) ha inspirado una gran actividad investigadora en este campo. Estos materiales, siendo los más representativos el grafeno y los aislantes topológicos, poseen propiedades únicas y extraordinarias que los hacen candidatos idóneos para su aplicación en nanoelectrónica y ámbitos afines[1, 2].

La principal característica de los materiales de Dirac deriva de su peculiar estructura de bandas electrónica cerca del nivel de Fermi, que presenta una dispersión lineal. Es por ello que los electrones de estas bandas se comportan como fermiones sin masa. Además, el acoplamiento del momento y el (pseudo)-espín de los electrones suprime la retrodispersión (en inglés, "backscattering") y da lugar a propiedades de transporte dependientes del espín[1, 3, 4]. Las posibles aplicaciones de estos materiales incluyen, por ejemplo, transistores de efecto de campo (FET, del inglés field effect transistor), dispositivos espintrónicos, fotovoltaica, almacenamiento de energía o computación cuántica (ver e.g. [5, 9, 11-13]).

En particular, el grafeno exhibe propiedades excepcionales que derivan de la hibridización sp^2 de los orbitales s, p_x, and p_y orbitals. De hecho, esta hibridización

es también responsable de la estructura de panal característica de este material: los orbitales hibridizados de cada átomo de carbono forman enlaces tipo σ con sus átomos vecinos, con una distancia de enlace de 1.42 Å y ángulos de 120 grados entre los enlaces. Estos enlaces tipo σ confieren al grafeno sus extraordinarias propiedades mecánicas, mientras que los orbitales p_z, que son perpendiculares al grafeno, forman enlaces tipo π y son responsables de sus formidables características electrónicas.

Los aislantes topológicos (TI, del inglés topological insulator) tridimensionales, por otro lado, poseen un "gap" de energía en volumen y un estado de superficie 2D que está protegido por simetría de inversión temporal (TRS, del inglés time reversal symmetry). Los aislantes topológicos investigados en esta tesis pertencen a la familia $Bi_2(Se_\delta Te_{1-\delta})_3$, donde δ varía de 0 a 1. La estructura atómica de esta familia de materiales presenta capas quintuples formadas por cinco capas atómicas unidas mediante enlaces covalentes, y enlazadas entre ellas por fuerzas débiles de tipo van der Waals.

Para el diseño de nuevos dispositivos electrónicos basados en materiales de Dirac 2D, es crucial entender y ser capaces de controlar sus propiedades estructurales, químicas y electrónicas. Esto ha motivado que, durante las últimas décadas, la actividad investigadora en el campo del estudio teórico y computacional de dichos materiales a la nanoescala haya crecido notoriamente[31]. En gran medida, esto ha sido posible al desarrollo de métodos de basados en primeros principios (*ab initio*). En particular, la teoría del funcional de la densidada (DFT, del inglés density functional theory) es actualmente la herramienta más ampliamente empleada para la simulación de propiedades estructurales y electrónicas de sistemas nanométricos complejos de gran interés tecnológico, tales como el grafeno y los aislantes topológicos. Además, en el contexto de la nanoelectrónica, es de particular interés la simulación de propiedades de transporte electrónico a través de materiales 2D conectados a conductores macroscópicos o electrodos. Al contrario que las simulaciones DFT estándar, los cálculos de transporte implican sistemas abiertos que son infinitos, no periódicos y fuera del equilibrio. Aún así, se ha demostrado la validez de los métodos de transporte basados en DFT para describir un gran número de experimentos de conductancia en sistemas nanométricos. En particular, el método más comunmente empleado combina la estructura electrónica DFT con las

funciones de Green fuera de equilibrio (NEGF, del inglés non-equilibrium Green's function). Precisamente, la tesis doctoral aquí resumida se centra en la aplicación de estas herramientas de cálculo para el estudio de las propiedades estructurales, electrónicas y de transporte de sistemas de grafeno y aislantes topológicos.

En el capítulo 2, describimos los métodos basados en DFT que se emplean a lo largo de la tesis. Fundamentalmente, la teoría del funcional de la densidad, que se basa en los trabajos seminales de Hohenberg, Kohn, y Sham[32, 33], es un procedimiento variacional alternativo para resolver la ecuación de Schrödinger de un sistema de muchos cuerpos, donde el funcional de la energía electrónica es minimizado con respecto a la densidad electrónica. Además de exponer los fundamentos más generales de este método, daremos detalles más técnicos sobre su aplicación práctica.

A continuación, en el capítulo 3, presentamos la extensión de los métodos DFT para el cálculo de transporte electrónico. En particular, nos centramos en la metodología basada en las funciones de Green fuera de equilibrio (NEGF) ya mencionadas. Trás presentar los conceptos fundamentales del método DFT-NEGF, se detalla una manera eficiente de calcular las funciones de Green, lo que tendrá importantes implicaciones en el estudio de sistemas realistas con un gran número de átomos. Además, describiremos una nueva herramienta desarrollada en el marco de esta tesis que permite visualizar los autocanales de transporte en sistemas de varios terminales.

El capítulo 4 está dedicado al estudio de diferentes configuraciones de contacto entre el grafeno y electrodos metálicos. La mayoría de dispositivos electrónicos basados en grafeno requieren la formación de este tipo de contactos. Sin embargo, esto puede alterar significativamente las excelentes características eléctricas del grafeno y, lo que es más importante, dar lugar a altas resistencias de contacto. Es por ello que en los últimos años se ha intensificado la investigación destinada a encontrar intercaras metal-grafeno con baja resistancia, con el fin de poder diseñar y fabricar contactos de mejor calidad[122, 126, 128, 130, 134, 137, 138]. En esta tesis se consideran dos tipos de contacto. Por un lado, el grafeno puede situarse sobre el metal, estableciendo un area de contacto bidimensional entre los dos componentes (contacto lateral). Alternativamente, el borde del grafeno se puede enlazar directamente con los electrodos metálicos, formando de esta manera un contacto

unidimensional entre el grafeno y el metal (contacto de borde). Así pues, en este capítulo se estudian tanto contactos laterales como de borde entre el grafeno y diferentes electrodos metálicos.

Cabe destacar que, debido a los métodos de fabricación actualmente empleados, los contactos metal-grafeno pueden sufrir modificaciones estructurales y químicas no deseadas. Esto hace que sea muy difícil controlar la resistencia y, en definitiva, el rendimiento de los dispositivos. De hecho, las características eléctricas de los dispositivos presentan a menudo diferencias significativas dependiendo de los detalles de fabricación de sus contactos. Motivados por la necesidad de entender mejor el origen de estas diferencias, en este capítulo se analiza en detalle y de manera sistemática la influencia que la contaminación de los bordes del grafeno tiene en la resistencia de los contactos, tanto laterales como de borde.

En la primera parte del capítulo, nos centramos en estudiar el efecto de la contaminación del borde de grafeno sobre las propiedades estructurales y de transporte de contactos laterales. Consideramos electrodos metálicos compuestos de oro (Au) o niquel (Ni), cuya interacción 2D con una capa de grafeno es muy débil y muy fuerte, respectivamente. Además, nos enfocamos en las terminaciones zz y Stone-Wales del grafeno. Los resultados indican que, cuando los bordes del grafeno no están pasivados, la estructura del metal en la zona de contacto sufre cambios significativos, sobre todo en el caso del Au. Aun así, en dichas intercaras (tanto Ni-grafeno como Au-grafeno) se forman enlaces fuertes con el metal y, por tanto, se obtienen buenas propiedades de transporte. Además, la resistencia de contacto en función del voltaje de compuerta (gate voltage) es del mismo orden de magnitud en ambos casos.

A continuación, investigamos los cambios que la pasivación de los bordes del grafeno induce en las propiedades de dichos contactos. En concreto, consideramos que el grafeno se pasiva con H, OH NH_2. La reconstrucción de las superficies metálicas es significativamente menor en el caso de los contactos pasivados, especialmente en el caso de las uniones Au-grafeno. En el caso de Ni, la contaminación del grafeno tiene una influencia débil sobre las propiedades de transporte de la intercara, y todos los contactos basados en dicho metal presentan resistencias del mismo orden de magnitud. Este comportamiento se puede atribuir a la fuerte a la fuerte hibridación entre los orbitales π del grafeno y los orbitales del Ni, siendo

este efecto dominante frente a la presencia de los contaminantes. Por el contrario, la interacción es mucho más débil entre el grafeno y Au, y los contaminantes adquieren un mayor protagonismo en la formación y las características del contacto. En consecuencia, la pasivación de los bordes del grafeno en el caso del Au da lugar a un aumento importante de la resistencia. También se han estudiado los efectos de filtro de espín en los contactos de borde. En el caso de los contactos basados en Ni, la eficiencia de filtro de espín (SFE, del inglés spin filter efficiency) presenta una gran variación de valores dependiendo de la terminación del grafeno. Por otro lado, en el caso del Au sólo la pasivación con OH produce una SFE significativa.

La segunda parte del capítulo 4 está dedicada al estudio exhaustivo de los contactos de borde metal-grafeno. En particular, consideramos grafeno con terminación zigzag (ZZ) y electros metálicos compuestos de niquel (Ni), cromio (Cr), titanio (Ti) u oro (Au). Además, dado que durante la fabricación de estos contactos se emplean comunmente compuestos reactivos que contienen flúor y/o oxigeno, estudiaremos la contaminación de los bordes del grafeno con F, F_2 y O. En primer lugar, y con el fin de entender la reactividad de estas intercaras, se han analizado las fuerzas que el metal induce en el grafeno, así como su dependencia con la contaminación. Nuestros resultados demuestran que las fuerzas en la intercara dependen en una manera compleja tanto del tipo del metal como de la contaminación del grafeno. A continuación, hemos estudiado la evolución estructural y química durante la formación del contacto. Los cálculos muestran que el tipo de metal empleado puede tener un papel crucial en la estabilidad del borde de grafeno contaminado. Por ejemplo, mientras que en el caso un borde de grafeno aislado la contaminación con un grupo F_2 es más estable que con un sólo átomo de flúor, la proximidad de un metal de transición hace que uno de los átomos del grupo F_2 sea "arrancado" del grafeno y se adsorba sobre la superficie metálica.

Respecto a las propiedades de transporte, encontramos que todos los contactos de borde no contaminados presentan resistencias del mismo orden de magnitud. Cuando el borde del grafeno está contaminado, la resistencia aumenta en todos los casos. Sin embargo, dicho aumento depende fuertemente del metal y, además, es menor cuando los contactos están pasivados con oxigeno en lugar de flúor. Debemos mencionar que estos resultados corresponden a contactos ideales, con bordes uniformes y superficies cristalinas perfectas. Por ello, con el objetivo de entender

mejor los mecanismos responsables de las varaciones entre diferentes dispositivos, también hemos llevado a cabo cálculos para un modelo de contacto más realista. En dicho modelo, se consideran diferentes contaminantes y varias distancias metal-grafeno, considerando geometrías congeladas. Estos cálculos muestran que el aumento relativo de las resistencias de contacto al alejar el grafeno del electrodo metálico es mucho menor en el caso de los contactos basados en Cr. Esto demuestra que este metal da lugar a contactos de borde de buena calidad, de acuerdo con lo observado experimentalmente. Al igual que en el caso de los contactos laterales, se ha analizado también la SFE de los contactos de borde. En general, al aumentar la separación entre el grafeno y el metal, la SFE aumenta. Aunque sólo en el caso de los contactos contaminados con flúor se recupera casi totalmente la polarización de espín de los bordes zz aislados.

En el capítulo 5, nos enfocamos en diversas nanoestructuras de grafeno. El confinamiento del grafeno en nanoestructuras puede da lugar a efectos como la apertura de un gap de energía [159, 160], y su potencial ha sido demostrado en diversas aplicaciones [196, 232, 233]. Sin embargo, sus propiedades dependen fuertemente de los detalles nanométricos, y es por ello crucial poder diseñar nanoestructuras de grafeno con precisión atómica. Esto es posible hoy en día gracias a los procesos de síntesis en superficie, que permiten crecer nanotiras (en inglés, "nanoribbons") u otras nanoestructuras de grafeno a partir de precursores moleculares. [164-169]. En este capítulo, estudiaremos un nuevo tipo de nanoribbons fabricados mediante este procedimiento. Estos nanoribbons, que denominamos 7-13-AGNR, tienen bordes tipo armchair y contiene segmentos con anchuras de 7 y 13 filas de carbono. Además, la unión de estos nanoribbons da lugar a un nuevo material 2D formado por grafeno nanoporoso, y que denotaremos NPG (del inglés, nanoporous graphene). Tantos los ribbons 7-13-AGNR como el NPG se han caracterizado teóricamente mediante simulaciones DFT y experimentalmente mediante medidas de microscopia de efecto túnel (del inglés, scanning tunneling microscoy, STM). En particular, las medidas de espectroscopía indican que tanto los nanoribbons como el NPG presentan gaps de energía del orden de 1eV. Esto ha sido confirmado por nuestros cálculos, y abre la puerta al uso de este material en aplicaciones que no son posibles mediante el grafeno estándar debido a su carácter semimetálico.

Además, nuestros cálculos DFT de estructura electrónica predicen que los rib-

bons 7-13-AGNR presentan diferentes tipos de bandas con propiedades interesantes. Por un lado, encontramos bandas electrónicas que sólo dispersan en la dirección periódica del ribbon (bandas longitudinales); por otro lado, las que denominamos bandas transversales están localizadas en los segmentos de 13 filas de átomos de C. Además, existen estados localizados en las zonas "vacías", que tienen su origen el potencial imagen del grafeno y que aparecen en las regiones confinadas entre los segmentos de 7 y 13 filas de carbono. Al formarse el NPG, su estructura electrónica hereda el carácter de las bandas del 7-13-AGNR, dando lugar a: i) bandas longitudinales que se extienden a lo largo del segmento de 7 filas de C en la dirección periódica, ii) bandas transversales que se extienden en la dirección perpéndicular a lo largo de la unión entre los segmentos de 13 filas de C, y iii) los estados de vació que forman lo que denominamos estados del poro. Destacar que los estados confinados en las regiones de vacío se observan experimentalmente en las imágenes STM, tanto en el nanoribbon como en el NPG. Mediante cálculos de transporte electrónico, hemos demostrado también que la existencia de bandas longitudinales y transversales dota a este material de propiedades de transporte anisotrópicas. Por tanto, queda demostrado que este material presenta propiedades realmente especiales e interesantes para su uso en diferentes aplicaciones de carácter tecnológico, por ejemplo, en transistores de efecto de campo (FET) o en sensores moleculares. Este trabajo abre la puerta a explorar diversas configuraciones estructurales (tamaño, forma) o químicas de los poros, con el fin de optimizar sus propiedades.

Por último, en el capítulo 6 estudiamos las propiedades del aislante topológico ternario Bi_2Se_2Te. La deposición de adátomos magnéticos en la superficie de un aislante topólogico puede romper la TRS y, por tanto, destruir el estado de superficie protegido topológicamente (TSS) [206-208]. Por lo tanto, supone un gran desafio para las aplicaciones basadas en la espintrónica el encontrar un material TI cuyo estado de superficie sea robusto ante distorsiones magnéticas. Motivados por esto, en este capítulo se estudia la robustez del estado de superficie de Bi_2Se_2Te frente a la adsorción de átomos de cobalto (Co). Experimentalmente se demuestra que este material presenta un alto desorden químico en su superficie, que esta compuesta de Se y Te con un ratio 1:1, y no muestra orden de largo alcance. Para estudiar las propiedades de este material, hemos considerado la estructura Bi_2Se_3 en volumen,

y hemos reemplazado 1, 2 o 3 átomos de Se de la superficie por átomos de Te. Mediante el estudio de la evolución de estas superficies al adsorber átomos de Co, se han podido confirmar las observaciones de STM: los átomos de Co no se adsorben en posiciones de alta simetría. Además, su momento magnético no desaparece por su interacción con el TI y, en la mayoria de los casos, apunta fuera del plano (out-of-plane). Todo esto parece indicar una interacción débil con los electrones de la superficie, y sugiere que este material ternario podría no perder su estado de superficie por efecto de los adsorbatos magnéticos. La confirmación experimental se ha logrado mediante la medida de patrones de interferencia de quasi-partículas (del inglés, quasi-particle interference (QPI) patterns) que se observan con STM. Los patrones QPI han permitido demostrar la ausencia de retro-dispersión cuando se adsorben átomos de Co sobre Bi_2Se_2Te, lo que significa que el TSS no se destruye.

En resumen, el trabajo de investigación recogido en esta tesis doctoral se ha centrado en la caracterización, mediante herramientas de simulación *ab initio*, de las propiedades electrónicas y de transporte de diversos nanosistemas basados en materiales de Dirac bidimensionales. Nuestros resultados han permitido interpretar medidas experimentales de STM y, aun más, han servido para predecir interesantes características noveles en nanoestructuras de grafeno y superficies de aislantes topológicos. Estos materiales presentan un extraordinario interés tecnológico y, por tanto, las conclusiones extraídas en esta tesis pueden ser de gran utilidad para el diseño futuro de aplicaciones basados en dichos materiales de Dirac 2D.

Bibliography

[1] T. Wehling, A. Black-Schaffer, and A. Balatsky. "Dirac materials". In: *Advances in Physics* 63 (Jan. 2, 2014), 1–76 (Cited on pages 9, 10, 123).

[2] J. Cayssol. "Introduction to Dirac materials and topological insulators". In: *Comptes Rendus Physique* 14 (2013), 760–778 (Cited on pages 9, 123).

[3] M. Katsnelson, K. Novoselov, and A. Geim. "Chiral tunnelling and the Klein paradox in graphene". In: *Nature physics* 2 (2006), 620–625 (Cited on pages 10, 123).

[4] P. Roushan, J. Seo, C. V. Parker, Y. S. Hor, D. Hsieh, D. Qian, A. Richardella, M. Z. Hasan, R. J. Cava, and A. Yazdani. "Topological surface states protected from backscattering by chiral spin texture". In: *Nature* 460 (Aug. 9, 2009), 1106 (Cited on pages 10, 11, 101, 123).

[5] F. Giubileo and A. D. Bartolomeo. "The role of contact resistance in graphene field-effect devices". In: *Progress in Surface Science* 92 (2017), 143–175 (Cited on pages 10, 37, 123).

[6] S. Ishida, Y. Anno, M. Takeuchi, M. Matsuoka, K. Takei, T. Arie, and S. Akita. "Highly photosensitive graphene field-effect transistor with optical memory function". In: *Scientific Reports* 5 (2015) (Cited on page 10).

[7] T. Georgiou, R. Jalil, B. D. Belle, L. Britnell, R. V. Gorbachev, S. V. Morozov, Y.-J. Kim, A. Gholinia, S. J. Haigh, O. Makarovsky, L. Eaves, L. A. Ponomarenko, A. K. Geim, K. S. Novoselov, and A. Mishchenko. "Vertical field-effect transistor based on graphene-WS2 heterostructures for flexible and transparent electronics". In: *Nat Nano* 8 (Feb. 2013), 100–103 (Cited on pages 10, 37).

[8] Q.-K. Xue. “A topological twist for transistors”. In: *Nature Nanotechnology* 6 (Apr. 6, 2011), 197 (Cited on page 10).

[9] S. Das, P. Sudhagar, Y. S. Kang, and W. Choi. “Graphene synthesis and application for solar cells”. In: *Journal of Materials Research* 29 (2014), 299–319 (Cited on pages 10, 123).

[10] Z. Liu, J. Li, and F. Yan. “Package-Free Flexible Organic Solar Cells with Graphene top Electrodes”. In: *Advanced Materials* 25 (2013), 4296–4301 (Cited on page 10).

[11] H. Peng, W. Dang, J. Cao, Y. Chen, D. Wu, W. Zheng, H. Li, Z.-X. Shen, and Z. Liu. “Topological insulator nanostructures for near-infrared transparent flexible electrodes”. In: *Nature Chemistry* 4 (Feb. 26, 2012), 281 (Cited on pages 10, 123).

[12] M. R. Rezapour, C. W. Myung, J. Yun, A. Ghassami, N. Li, S. U. Yu, A. Hajibabaei, Y. Park, and K. S. Kim. “Graphene and Graphene Analogs toward Optical, Electronic, Spintronic, Green-Chemical, Energy-Material, Sensing, and Medical Applications”. In: *ACS Applied Materials & Interfaces* (July 5, 2017) (Cited on pages 10, 123).

[13] S. S. Hong, D. Kong, and Y. Cui. “Topological insulator nanostructures”. In: *MRS Bulletin* 39 (2014), 873–879 (Cited on pages 10, 123).

[14] K. S. Novoselov, V. I. Fal’ko, L. Colombo, P. R. Gellert, M. G. Schwab, and K. Kim. “A roadmap for graphene”. In: *Nature* 490 (Oct. 11, 2012), 192–200 (Cited on page 10).

[15] F. Leonard and A. A. Talin. “Electrical contacts to one- and two-dimensional nanomaterials”. In: *Nat Nano* 6 (Dec. 2011), 773–783 (Cited on page 10).

[16] K. R. Amin and A. Bid. “High-Performance Sensors Based on Resistance Fluctuations of Single-Layer-Graphene Transistors”. In: *ACS Applied Materials & Interfaces* (Aug. 24, 2015) (Cited on page 10).

[17] D. Jariwala, V. K. Sangwan, L. J. Lauhon, T. J. Marks, and M. C. Hersam. “Carbon nanomaterials for electronics, optoelectronics, photovoltaics, and sensing”. In: *Chemical Society Reviews* 42 (2013), 2824–2860 (Cited on page 10).

[18] P. R. Wallace. “The Band Theory of Graphite”. In: *Phys. Rev.* 71 (May 1947), 622–634 (Cited on page 10).

[19] D. P. DiVincenzo and E. J. Mele. “Self-consistent effective-mass theory for intralayer screening in graphite intercalation compounds”. In: *Phys. Rev. B* 29 (Feb. 1984), 1685–1694 (Cited on page 10).

[20] G. W. Semenoff. “Condensed-Matter Simulation of a Three-Dimensional Anomaly”. In: *Phys. Rev. Lett.* 53 (Dec. 1984), 2449–2452 (Cited on page 10).

[21] F. D. M. Haldane. “Model for a Quantum Hall Effect without Landau Levels: Condensed-Matter Realization of the ”Parity Anomaly””. In: *Phys. Rev. Lett.* 61 (Oct. 1988), 2015–2018 (Cited on page 10).

[22] K. S. Novoselov, A. K. Geim, S. V. Morozov, D. Jiang, Y. Zhang, S. V. Dubonos, I. V. Grigorieva, and A. A. Firsov. “Electric Field Effect in Atomically Thin Carbon Films”. In: *Science* 306 (2004), 666–669 (Cited on page 10).

[23] L. Fu and C. L. Kane. “Topological insulators with inversion symmetry”. In: *Phys. Rev. B* 76 (July 2007), 045302 (Cited on page 11).

[24] L. Fu, C. L. Kane, and E. J. Mele. “Topological Insulators in Three Dimensions”. In: *Phys. Rev. Lett.* 98 (Mar. 2007), 106803 (Cited on page 11).

[25] D. J. Thouless, M. Kohmoto, M. P. Nightingale, and M. den Nijs. “Quantized Hall Conductance in a Two-Dimensional Periodic Potential”. In: *Phys. Rev. Lett.* 49 (Aug. 1982), 405–408 (Cited on page 11).

[26] C. L. Kane and E. J. Mele. “Z_2 Topological Order and the Quantum Spin Hall Effect”. In: *Phys. Rev. Lett.* 95 (Sept. 2005), 146802 (Cited on pages 11, 101).

[27] D. Hsieh, D. Qian, L. Wray, Y. Xia, Y. S. Hor, R. J. Cava, and M. Z. Hasan. “A topological Dirac insulator in a quantum spin Hall phase”. In: *Nature* 452 (Apr. 24, 2008), 970 (Cited on page 11).

[28] C. Felser and X.-L. Qi. “Topological insulators”. In: *MRS Bulletin* 39 (2014), 843–846 (Cited on pages 11, 101).

[29] X.-L. Qi and S.-C. Zhang. “Topological insulators and superconductors”. In: *Rev. Mod. Phys.* 83 (Oct. 2011), 1057–1110 (Cited on pages 11, 101).

[30] M. Z. Hasan and C. L. Kane. “*Colloquium* : Topological insulators”. In: *Rev. Mod. Phys.* 82 (Nov. 2010), 3045–3067 (Cited on pages 11, 101).

[31] A. V. Akimov and O. V. Prezhdo. “Large-Scale Computations in Chemistry: A Bird’s Eye View of a Vibrant Field”. In: *Chemical Reviews* (Apr. 8, 2015) (Cited on pages 11, 124).

[32] P. Hohenberg and W. Kohn. “Inhomogeneous Electron Gas”. In: *Phys. Rev.* 136 (Nov. 1964), B864–B871 (Cited on pages 11, 15–18, 125).

[33] W. Kohn and L. J. Sham. “Self-Consistent Equations Including Exchange and Correlation Effects”. In: *Phys. Rev.* 140 (Nov. 1965), A1133–A1138 (Cited on pages 11, 15, 18, 19, 125).

[34] R. O. Jones. “Density functional theory: Its origins, rise to prominence, and future”. In: *Rev. Mod. Phys.* 87 (Aug. 2015), 897–923 (Cited on pages 11, 15).

[35] K. Burke. “Perspective on density functional theory”. In: *The Journal of Chemical Physics* 136 (2012), 150901 (Cited on pages 11, 15, 20).

[36] M. Brandbyge, J.-L. Mozos, P. Ordejón, J. Taylor, and K. Stokbro. “Density-functional method for nonequilibrium electron transport”. In: *Phys. Rev. B* 65 (Mar. 2002), 165401 (Cited on pages 11, 22, 27–30, 39, 49, 70).

[37] N. Papior, N. Lorente, T. Frederiksen, A. García, and M. Brandbyge. “Improvements on non-equilibrium and transport Green function techniques: The next-generation transiesta”. In: *Computer Physics Communications* 212 (Mar. 2017), 8–24 (Cited on pages 11, 22, 27, 29–32, 39, 49, 70).

[38] R. A. Bell, S. M.-M. Dubois, M. C. Payne, and A. A. Mostofi. “Electronic transport calculations in the onetep code: Implementation and applications”. In: *Computer Physics Communications* 193 (Aug. 1, 2015), 78–88 (Cited on pages 11, 27).

[39] G. Binnig and H. Rohrer. “Scanning tunneling microscopy”. In: *Helv. Phys. Acta* 55 (1982), 128 (Cited on pages 11, 119).

[40] G. Binnig and H. Rohrer. "Scanning tunneling microscopy - from birth to adolescence". In: *Rev. Mod. Phys.* 59 (July 1987), 615–625 (Cited on page 11).

[41] W. Kohn. "Nobel Lecture: Electronic structure of matter - wave functions and density functionals". In: *Rev. Mod. Phys.* 71 (Oct. 1999), 1253–1266 (Cited on pages 15–17).

[42] R. M. Martin. *Electronic structure: basic theory and practical methods*. Cambridge university press, 2004 (Cited on pages 15–20, 23–26).

[43] M. Born and R. Oppenheimer. "Zur Quantentheorie der Molekeln". In: *Annalen der Physik* 389 (1927), 457–484 (Cited on page 16).

[44] P. A. M. Dirac. "Note on Exchange Phenomena in the Thomas Atom". In: *Mathematical Proceedings of the Cambridge Philosophical Society* 26 (1930), 376–385 (Cited on page 16).

[45] L. H. Thomas. "The calculation of atomic fields". In: *Mathematical Proceedings of the Cambridge Philosophical Society* 23 (1927), 542–548 (Cited on page 16).

[46] E. Fermi. "Un metodo statistico per la determinazione di alcune priorieta dell'atome". In: *Rend. Accad. Naz. Lincei* 6 (1927), 32 (Cited on page 16).

[47] N. D. Mermin. "Thermal Properties of the Inhomogeneous Electron Gas". In: *Phys. Rev.* 137 (Mar. 1965), A1441–A1443 (Cited on page 18).

[48] J. P. Perdew and M. R. Norman. "Electron removal energies in Kohn-Sham density-functional theory". In: *Phys. Rev. B* 26 (Nov. 1982), 5445–5450 (Cited on page 18).

[49] M. Levy, J. P. Perdew, and V. Sahni. "Exact differential equation for the density and ionization energy of a many-particle system". In: *Phys. Rev. A* 30 (Nov. 1984), 2745–2748 (Cited on page 18).

[50] J. Klimeš, D. R. Bowler, and A. Michaelides. "Chemical accuracy for the van der Waals density functional". In: *Journal of Physics: Condensed Matter* 22 (2010), 022201 (Cited on pages 19, 21, 39).

[51] G. Román-Pérez and J. M. Soler. "Efficient Implementation of a van der Waals Density Functional: Application to Double-Wall Carbon Nanotubes". In: *Phys. Rev. Lett.* 103 (Aug. 2009), 096102 (Cited on page 19).

[52] M. Dion, H. Rydberg, E. Schröder, D. C. Langreth, and B. I. Lundqvist. "Van der Waals Density Functional for General Geometries". In: *Phys. Rev. Lett.* 92 (June 2004), 246401 (Cited on page 19).

[53] J. P. Perdew, K. Burke, and M. Ernzerhof. "Generalized Gradient Approximation Made Simple". In: *Phys. Rev. Lett.* 77 (Oct. 1996), 3865–3868 (Cited on pages 19, 20, 49, 70, 102).

[54] J. P. Perdew, K. Burke, and Y. Wang. "Generalized gradient approximation for the exchange-correlation hole of a many-electron system". In: *Phys. Rev. B* 54 (Dec. 1996), 16533–16539 (Cited on pages 19, 20).

[55] J. P. Perdew and Y. Wang. "Accurate and simple analytic representation of the electron-gas correlation energy". In: *Phys. Rev. B* 45 (June 1992), 13244–13249 (Cited on page 19).

[56] J. P. Perdew and A. Zunger. "Self-interaction correction to density-functional approximations for many-electron systems". In: *Phys. Rev. B* 23 (May 1981), 5048–5079 (Cited on page 19).

[57] D. M. Ceperley and B. J. Alder. "Ground State of the Electron Gas by a Stochastic Method". In: *Phys. Rev. Lett.* 45 (Aug. 1980), 566–569 (Cited on page 19).

[58] R. O. Jones and O. Gunnarsson. "The density functional formalism, its applications and prospects". In: *Rev. Mod. Phys.* 61 (July 1989), 689–746 (Cited on page 20).

[59] J. P. Perdew and K. Burke. "Comparison shopping for a gradient-corrected density functional". In: *International Journal of Quantum Chemistry* 57 (1996), 309–319 (Cited on page 20).

[60] M. Ernzerhof and G. E. Scuseria. "Assessment of the Perdew–Burke–Ernzerhof exchange-correlation functional". In: *The Journal of Chemical Physics* 110 (1999), 5029–5036 (Cited on page 20).

[61] D. C. Patton, D. V. Porezag, and M. R. Pederson. "Simplified generalized-gradient approximation and anharmonicity: Benchmark calculations on molecules". In: *Phys. Rev. B* 55 (Mar. 1997), 7454–7459 (Cited on page 20).

[62] D. C. Patton, D. V. Porezag, and M. R. Pederson. "Erratum: Simplified generalized-gradient approximation and anharmonicity: Benchmark calculations on molecules [Phys. Rev. B 55, 7454 (1997)]". In: *Phys. Rev. B* 57 (Jan. 1998), 1995–1995 (Cited on page 20).

[63] A. Zupan, P. Blaha, K. Schwarz, and J. P. Perdew. "Pressure-induced phase transitions in solid Si, SiO_2, and Fe: Performance of local-spin-density and generalized-gradient-approximation density functionals". In: *Phys. Rev. B* 58 (Nov. 1998), 11266–11272 (Cited on page 20).

[64] D. R. Hamann. "H_2O hydrogen bonding in density-functional theory". In: *Phys. Rev. B* 55 (Apr. 1997), R10157–R10160 (Cited on page 20).

[65] S. Grimme. "Semiempirical GGA-type density functional constructed with a long-range dispersion correction". In: *Journal of Computational Chemistry* 27 (Sept. 5, 2006), 1787–1799 (Cited on pages 20, 21, 102).

[66] F. Bloch. "Über die Quantenmechanik der Elektronen in Kristallgittern". In: *Zeitschrift für Physik* 52 (July 1, 1929), 555–600 (Cited on page 21).

[67] D. R. Hamann, M. Schlüter, and C. Chiang. "Norm-Conserving Pseudopotentials". In: *Phys. Rev. Lett.* 43 (Nov. 1979), 1494–1497 (Cited on page 22).

[68] N. Troullier and J. L. Martins. "Efficient pseudopotentials for plane-wave calculations". In: *Phys. Rev. B* 43 (Jan. 1991), 1993–2006 (Cited on page 22).

[69] D. Vanderbilt. "Soft self-consistent pseudopotentials in a generalized eigenvalue formalism". In: *Phys. Rev. B* 41 (Apr. 1990), 7892–7895 (Cited on page 22).

[70] N. S. Ostlund and A. Szabo. *Modern quantum chemistry: introduction to advanced electronic structure theory*. Dover Publications Inc, 1996 (Cited on pages 22, 24).

[71] S. R. Jensen, S. Saha, J. A. Flores-Livas, W. Huhn, V. Blum, S. Goedecker, and L. Frediani. "The Elephant in the Room of Density Functional Theory Calculations". In: *The Journal of Physical Chemistry Letters* (Mar. 14, 2017), 1449–1457 (Cited on page 22).

[72] A. E. A. Fouda and N. A. Besley. "Assessment of basis sets for density functional theory-based calculations of core-electron spectroscopies". In: *Theoretical Chemistry Accounts* 137 (Dec. 15, 2017), 6 (Cited on page 22).

[73] J. Kreutzer, P. Blaha, and U. Schubert. "Assessment of different basis sets and DFT functionals for the calculation of structural parameters, vibrational modes and ligand binding energies of Zr_4O_2(carboxylate)$_{12}$ clusters". In: *Computational and Theoretical Chemistry* 1084 (May 15, 2016), 162–168 (Cited on page 22).

[74] B. Temelso, E. F. Valeev, and C. D. Sherrill. "A Comparison of One-Particle Basis Set Completeness, Higher-Order Electron Correlation, Relativistic Effects, and Adiabatic Corrections for Spectroscopic Constants of BH, CH^+, and NH". In: *The Journal of Physical Chemistry A* 108 (Apr. 1, 2004), 3068–3075 (Cited on page 22).

[75] J. M. L. Martin, J. El-Yazal, and J.-P. François. "Basis set convergence and performance of density functional theory including exact exchange contributions for geometries and harmonic frequencies". In: *Molecular Physics* 86 (1995), 1437–1450 (Cited on page 22).

[76] G. Kresse and J. Furthmüller. "Efficient iterative schemes for ab initio total-energy calculations using a plane-wave basis set". In: *Phys. Rev. B* 54 (Oct. 1996), 11169–11186 (Cited on pages 22, 50, 71, 102).

[77] G. Kresse and J. Furthmüller. "Efficiency of ab-initio total energy calculations for metals and semiconductors using a plane-wave basis set". In: *Computational Materials Science* 6 (July 1, 1996), 15–50 (Cited on pages 22, 50, 71, 102).

[78] G. Kresse and J. Hafner. "Ab initio molecular-dynamics simulation of the liquid-metal-amorphous-semiconductor transition in germanium". In: *Phys. Rev. B* 49 (May 1994), 14251–14269 (Cited on pages 22, 50, 71, 102).

[79] G. Kresse and J. Hafner. "Ab initio molecular dynamics for liquid metals". In: *Phys. Rev. B* 47 (Jan. 1993), 558–561 (Cited on pages 22, 50, 71, 102).

[80] P. Giannozzi, S. Baroni, N. Bonini, M. Calandra, R. Car, C. Cavazzoni, D. Ceresoli, G. L. Chiarotti, M. Cococcioni, I. Dabo, A. Dal Corso, S. de Gironcoli, S. Fabris, G. Fratesi, R. Gebauer, U. Gerstmann, C. Gougoussis, A. Kokalj, M. Lazzeri, L. Martin-Samos, N. Marzari, F. Mauri, R. Mazzarello, S. Paolini, A. Pasquarello, L. Paulatto, C. Sbraccia, S. Scandolo, G. Sclauzero, A. P. Seitsonen, A. Smogunov, P. Umari, and R. M. Wentzcovitch. "QUANTUM ESPRESSO: a modular and open-source software project for quantum simulations of materials". In: *Journal of physics: Condensed matter* 21 (2009), 395502 (Cited on page 22).

[81] J. M. Soler, E. Artacho, J. D. Gale, A. García, J. Junquera, P. Ordejón, and Daniel Sánchez-Portal. "The SIESTA method for ab initio order-N materials simulation". In: *Journal of Physics: Condensed Matter* 14 (2002), 2745 (Cited on pages 22, 24, 33, 39, 49, 50, 70, 71, 121).

[82] P. A. M. Dirac. "The quantum theory of the electron". In: *Proceedings of the Royal Society of London. Series A* 117 (Feb. 1, 1928), 610 (Cited on page 25).

[83] P. A. M. Dirac. "The quantum theory of the Electron. Part II". In: *Proceedings of the Royal Society of London A: Mathematical, Physical and Engineering Sciences* 118 (1928), 351–361 (Cited on page 25).

[84] U. v. Barth and L. Hedin. "A local exchange-correlation potential for the spin polarized case. i". In: *Journal of Physics C: Solid State Physics* 5 (1972), 1629 (Cited on page 26).

[85] V. I. Anisimov and O. Gunnarsson. "Density-functional calculation of effective Coulomb interactions in metals". In: *Phys. Rev. B* 43 (Apr. 1991), 7570–7574 (Cited on pages 26, 103).

[86] V. I. Anisimov, J. Zaanen, and O. K. Andersen. "Band theory and Mott insulators: Hubbard U instead of Stoner I". In: *Phys. Rev. B* 44 (July 1991), 943–954 (Cited on page 26).

[87] J. Hubbard. “Electron correlations in narrow energy bands”. In: *Proceedings of the Royal Society of London. Series A. Mathematical and Physical Sciences* 276 (Nov. 26, 1963), 238 (Cited on page 26).

[88] J. Hubbard. “Electron correlations in narrow energy bands III. An improved solution”. In: *Proceedings of the Royal Society of London. Series A. Mathematical and Physical Sciences* 281 (Sept. 22, 1964), 401 (Cited on page 26).

[89] J. Hubbard. “Electron correlations in narrow energy bands. II. The degenerate band case”. In: *Proceedings of the Royal Society of London. Series A. Mathematical and Physical Sciences* 277 (Jan. 21, 1964), 237 (Cited on page 26).

[90] S. L. Dudarev, G. A. Botton, S. Y. Savrasov, C. J. Humphreys, and A. P. Sutton. “Electron-energy-loss spectra and the structural stability of nickel oxide: An LSDA+U study”. In: *Phys. Rev. B* 57 (Jan. 1998), 1505–1509 (Cited on pages 26, 102).

[91] V. I. Anisimov, F. Aryasetiawan, and A. I. Lichtenstein. “First-principles calculations of the electronic structure and spectra of strongly correlated systems: the LDA + U method”. In: *Journal of Physics: Condensed Matter* 9 (1997), 767 (Cited on page 26).

[92] A. I. Liechtenstein, V. I. Anisimov, and J. Zaanen. “Density-functional theory and strong interactions: Orbital ordering in Mott-Hubbard insulators”. In: *Phys. Rev. B* 52 (Aug. 1995), R5467–R5470 (Cited on page 26).

[93] I. V. Solovyev, P. H. Dederichs, and V. I. Anisimov. “Corrected atomic limit in the local-density approximation and the electronic structure of d impurities in Rb”. In: *Phys. Rev. B* 50 (Dec. 1994), 16861–16871 (Cited on page 26).

[94] V. I. Anisimov, I. V. Solovyev, M. A. Korotin, M. T. Czyżyk, and G. A. Sawatzky. “Density-functional theory and NiO photoemission spectra”. In: *Phys. Rev. B* 48 (Dec. 1993), 16929–16934 (Cited on page 26).

[95] A. Garcia-Lekue, M. Vergniory, X. Jiang, and L. Wang. “Ab initio quantum transport calculations using plane waves”. In: *Progress in Surface Science* 90 (Aug. 1, 2015), 292–318 (Cited on pages 27, 32).

[96] L.-W. Wang. "Elastic quantum transport calculations using auxiliary periodic boundary conditions". In: *Phys. Rev. B* 72 (July 2005), 045417 (Cited on page 27).

[97] A. Garcia-Lekue and L.-W. Wang. "Elastic quantum transport calculations for molecular nanodevices using plane waves". In: *Phys. Rev. B* 74 (Dec. 2006), 245404 (Cited on page 27).

[98] J. Taylor, H. Guo, and J. Wang. "Ab initio modeling of quantum transport properties of molecular electronic devices". In: *Phys. Rev. B* 63 (June 2001), 245407 (Cited on page 27).

[99] Y. Xue, S. Datta, and M. A. Ratner. "First-principles based matrix Green's function approach to molecular electronic devices: general formalism". In: *Chemical Physics* 281 (Aug. 1, 2002), 151–170 (Cited on page 27).

[100] J. Zhang, S. Hou, R. Li, Z. Qian, R. Han, Z. Shen, X. Zhao, and Z. Xue. "An accurate and efficient self-consistent approach for calculating electron transport through molecular electronic devices: including the corrections of electrodes". In: *Nanotechnology* 16 (2005), 3057 (Cited on page 27).

[101] M. Paulsson. "Non Equilibrium Green's Functions for Dummies: Introduction to the One Particle NEGF equations". In: *eprint arXiv:cond-mat/0210519* (Oct. 2002) (Cited on pages 28–30).

[102] E. M. Godfrin. "A method to compute the inverse of an n-block tridiagonal quasi-Hermitian matrix". In: *Journal of Physics: Condensed Matter* 3 (1991), 7843 (Cited on page 30).

[103] O. Hod, J. E. Peralta, and G. E. Scuseria. "First-principles electronic transport calculations in finite elongated systems: A divide and conquer approach". In: *The Journal of Chemical Physics* 125 (Sept. 19, 2006), 114704 (Cited on page 30).

[104] M. G. Reuter and J. C. Hill. "An efficient, block-by-block algorithm for inverting a block tridiagonal, nearly block Toeplitz matrix". In: *Computational Science & Discovery* 5 (2012), 014009 (Cited on page 30).

[105] M. Paulsson and M. Brandbyge. "Transmission eigenchannels from nonequilibrium Green's functions". In: *Phys. Rev. B* 76 (Sept. 2007), 115117 (Cited on page 32).

[106] N. R. Papior. *sisl: v0.9.2*. Version 0.9.2 (Cited on pages 32, 33).

[107] T. Frederiksen, M. Paulsson, M. Brandbyge, and A.-P. Jauho. "Inelastic transport theory from first principles: Methodology and application to nanoscale devices". In: *Phys. Rev. B* 75 (May 2007), 205413 (Cited on page 32).

[108] E. Jones, T. Oliphant, and P. Peterson. *SciPy open source scientific tools for Python*. 2014. URL: `https://www.scipy.org/` (visited on 03/02/2018) (Cited on page 32).

[109] S. v. d. Walt, S. C. Colbert, and G. Varoquaux. "The NumPy Array: A Structure for Efficient Numerical Computation". In: *Computing in Science Engineering* 13 (Mar. 2011), 22–30 (Cited on page 32).

[110] A. H. Castro Neto, F. Guinea, N. M. R. Peres, K. S. Novoselov, and A. K. Geim. "The electronic properties of graphene". In: *Rev. Mod. Phys.* 81 (Jan. 2009), 109–162 (Cited on page 37).

[111] A. A. Balandin, S. Ghosh, W. Bao, I. Calizo, D. Teweldebrhan, F. Miao, and C. N. Lau. "Superior Thermal Conductivity of Single-Layer Graphene". In: *Nano Letters* 8 (2008), 902–907 (Cited on page 37).

[112] Y.-M. Lin, C. Dimitrakopoulos, K. A. Jenkins, D. B. Farmer, H.-Y. Chiu, A. Grill, and P. Avouris. "100-GHz Transistors from Wafer-Scale Epitaxial Graphene". In: *Science* 327 (Feb. 4, 2010), 662 (Cited on page 37).

[113] Y. Wu, K. A. Jenkins, A. Valdes-Garcia, D. B. Farmer, Y. Zhu, A. A. Bol, C. Dimitrakopoulos, W. Zhu, F. Xia, P. Avouris, and Y.-M. Lin. "State-of-the-Art Graphene High-Frequency Electronics". In: *Nano Letters* 12 (2012), 3062–3067 (Cited on page 37).

[114] "Ten years in two dimensions". In: *Nat Nano* 9 (Oct. 2014), 725–725 (Cited on page 37).

[115] L. Huang, H. Xu, Z. Zhang, C. Chen, J. Jiang, X. Ma, B. Chen, Z. Li, H. Zhong, and L.-M. Peng. "Graphene/Si CMOS Hybrid Hall Integrated Circuits". In: 4 (July 7, 2014), 5548 (Cited on page 37).

[116] G. Giovannetti, P. A. Khomyakov, G. Brocks, V. M. Karpan, J. van den Brink, and P. J. Kelly. "Doping Graphene with Metal Contacts". In: *Phys. Rev. Lett.* 101 (July 2008), 026803 (Cited on page 37).

[117] S. Barraza-Lopez, M. Vanević, M. Kindermann, and M. Y. Chou. "Effects of Metallic Contacts on Electron Transport through Graphene". In: *Phys. Rev. Lett.* 104 (Feb. 2010), 076807 (Cited on pages 37, 48, 65).

[118] A. D. Franklin, S. J. Han, A. A. Bol, and W. Haensch. "Effects of Nanoscale Contacts to Graphene". In: *IEEE Electron Device Letters* 32 (Aug. 2011), 1035–1037 (Cited on page 37).

[119] A. D. Franklin, S. J. Han, A. A. Bol, and V. Perebeinos. "Double Contacts for Improved Performance of Graphene Transistors". In: *IEEE Electron Device Letters* 33 (Jan. 2012), 17–19 (Cited on page 37).

[120] J. S. Moon, M. Antcliffe, H. C. Seo, D. Curtis, S. Lin, A. Schmitz, I. Milosavljevic, A. A. Kiselev, R. S. Ross, D. K. Gaskill, P. M. Campbell, R. C. Fitch, K.-M. Lee, and P. Asbeck. "Ultra-low resistance ohmic contacts in graphene field effect transistors". In: *Applied Physics Letters* 100 (2012), 203512 (Cited on page 37).

[121] S. M. Song, J. K. Park, O. J. Sul, and B. J. Cho. "Determination of Work Function of Graphene under a Metal Electrode and Its Role in Contact Resistance". In: *Nano Letters* 12 (Aug. 8, 2012), 3887–3892 (Cited on page 37).

[122] S. M. Song, T. Y. Kim, O. J. Sul, W. C. Shin, and B. J. Cho. "Improvement of graphene–metal contact resistance by introducing edge contacts at graphene under metal". In: *Applied Physics Letters* 104 (2014), 183506 (Cited on pages 37, 38, 125).

[123] H. Zhong, Z. Zhang, B. Chen, H. Xu, D. Yu, L. Huang, and L. Peng. "Realization of low contact resistance close to theoretical limit in graphene transistors". In: *Nano Research* 8 (2015), 1669–1679 (Cited on page 37).

[124] E. Voloshina and Y. Dedkov. "Graphene on metallic surfaces: problems and perspectives". In: *Physical Chemistry Chemical Physics* 14 (2012), 13502–13514 (Cited on page 37).

[125] E. N. Voloshina and Y. S. Dedkov. "General approach to understanding the electronic structure of graphene on metals". In: *Materials Research Express* 1 (2014), 035603 (Cited on pages 37, 39).

[126] F. Xia, V. Perebeinos, Y.-m. Lin, Y. Wu, and P. Avouris. "The origins and limits of metal-graphene junction resistance". In: *Nat Nano* 6 (Mar. 2011), 179–184 (Cited on pages 37, 38, 125).

[127] K. Stokbro, M. Engelund, and A. Blom. "Atomic-scale model for the contact resistance of the nickel-graphene interface". In: *Phys. Rev. B* 85 (Apr. 2012), 165442 (Cited on pages 37, 65).

[128] S. M. Song and B. J. Cho. "Contact resistance in graphene channel transistors". In: *Carbon letters* 3 (July 2013) (Cited on pages 37, 125).

[129] B. Ma, C. Gong, Y. Wen, R. Chen, K. Cho, and B. Shan. "Modulation of contact resistance between metal and graphene by controlling the graphene edge, contact area, and point defects: An ab initio study". In: *Journal of Applied Physics* 115 (2014), 183708 (Cited on pages 37, 65).

[130] L. Wang, I. Meric, P. Y. Huang, Q. Gao, Y. Gao, H. Tran, T. Taniguchi, K. Watanabe, L. M. Campos, D. A. Muller, J. Guo, P. Kim, J. Hone, K. L. Shepard, and C. R. Dean. "One-Dimensional Electrical Contact to a Two-Dimensional Material". In: *Science* 342 (Nov. 1, 2013), 614–617 (Cited on pages 38, 47, 50, 61, 64, 125).

[131] J. T. Smith, A. D. Franklin, D. B. Farmer, and C. D. Dimitrakopoulos. "Reducing Contact Resistance in Graphene Devices through Contact Area Patterning". In: *ACS Nano* 7 (Apr. 23, 2013), 3661–3667 (Cited on pages 38, 64).

[132] T. Chu and Z. Chen. "Understanding the Electrical Impact of Edge Contacts in Few-Layer Graphene". In: *ACS Nano* 8 (Apr. 22, 2014), 3584–3589 (Cited on pages 38, 64).

[133] D. W. Yue, C. H. Ra, X. C. Liu, D. Y. Lee, and W. J. Yoo. "Edge contacts of graphene formed by using a controlled plasma treatment". In: *Nanoscale* 7 (2015), 825–831 (Cited on pages 38, 64).

[134] K. H. Khoo, W. S. Leong, J. T. L. Thong, and S. Y. Quek. "Origin of Contact Resistance at Ferromagnetic Metal–Graphene Interfaces". In: *ACS Nano* 10 (Nov. 13, 2016), 11219–11227 (Cited on pages 38, 41, 47, 64, 125).

[135] H.-Y. Park, W.-S. Jung, D.-H. Kang, J. Jeon, G. Yoo, Y. Park, J. Lee, Y. H. Jang, J. Lee, S. Park, H.-Y. Yu, B. Shin, S. Lee, and J.-H. Park. "Extremely Low Contact Resistance on Graphene through n-Type Doping and Edge Contact Design". In: *Advanced Materials* 28 (2016), 864–870 (Cited on pages 38, 64).

[136] C. Gong, C. Zhang, Y. J. Oh, W. Wang, G. Lee, B. Shan, R. M. Wallace, and K. Cho. "Electronic transport across metal-graphene edge contact". In: *2D Materials* 4 (2017), 025033 (Cited on pages 38, 64).

[137] T. Cusati, G. Fiori, A. Gahoi, V. Passi, M. C. Lemme, A. Fortunelli, and G. Iannaccone. "Electrical properties of graphene-metal contacts". In: *Scientific Reports* 7 (July 11, 2017), 5109 (Cited on pages 38, 65, 125).

[138] J. A. Robinson, M. LaBella, M. Zhu, M. Hollander, R. Kasarda, Z. Hughes, K. Trumbull, R. Cavalero, and D. Snyder. "Contacting graphene". In: *Applied Physics Letters* 98 (Jan. 31, 2011), 053103 (Cited on pages 38, 125).

[139] K. Nagashio, T. Nishimura, K. Kita, and A. Toriumi. "Metal/graphene contact as a performance Killer of ultra-high mobility graphene analysis of intrinsic mobility and contact resistance". In: *Electron Devices Meeting (IEDM), 2009 IEEE International* (Dec. 7, 2009), 1–4 (Cited on page 38).

[140] A. Venugopal, L. Colombo, and E. M. Vogel. "Contact resistance in few and multilayer graphene devices". In: *Applied Physics Letters* 96 (2010), 013512 (Cited on page 38).

[141] M. S. Choi, S. H. Lee, and W. J. Yoo. "Plasma treatments to improve metal contacts in graphene field effect transistor". In: *Journal of Applied Physics* 110 (2011), 073305 (Cited on page 38).

[142] J. Sławińska, P. Dabrowski, and I. Zasada. "Doping of graphene by a Au(111) substrate: Calculation strategy within the local density approximation and a semiempirical van der Waals approach". In: *Phys. Rev. B* 83 (June 2011), 245429 (Cited on page 39).

[143] A. Garcia-Lekue, M. Ollé, D. Sanchez-Portal, J. J. Palacios, A. Mugarza, G. Ceballos, and P. Gambardella. "Substrate-Induced Stabilization and Reconstruction of Zigzag Edges in Graphene Nanoislands on Ni(111)". In: *The Journal of Physical Chemistry C* 119 (Feb. 26, 2015), 4072–4078 (Cited on page 39).

[144] H. J. Monkhorst and J. D. Pack. "Special points for Brillouin-zone integrations". In: *Phys. Rev. B* 13 (June 1976), 5188–5192 (Cited on pages 40, 49, 70, 102).

[145] O. Hod, V. Barone, J. E. Peralta, and G. E. Scuseria. "Enhanced Half-Metallicity in Edge-Oxidized Zigzag Graphene Nanoribbons". In: *Nano Letters* 7 (Aug. 8, 2007), 2295–2299 (Cited on page 43).

[146] Y. Li, Z. Zhou, P. Shen, and Z. Chen. "Spin Gapless Semiconductor-Metal-Half-Metal Properties in Nitrogen-Doped Zigzag Graphene Nanoribbons". In: *ACS Nano* 3 (July 28, 2009), 1952–1958 (Cited on page 43).

[147] G. Lee and K. Cho. "Electronic structures of zigzag graphene nanoribbons with edge hydrogenation and oxidation". In: *Phys. Rev. B* 79 (Apr. 2009), 165440 (Cited on page 43).

[148] F. Cervantes-Sodi, G. Csányi, S. Piscanec, and A. C. Ferrari. "Edge functionalized and substitutionally doped graphene nanoribbons: Electronic and spin properties". In: *Phys. Rev. B* 77 (Apr. 2008), 165427 (Cited on page 43).

[149] Q. Gao and J. Guo. "Role of chemical termination in edge contact to graphene". In: *APL Mater.* 2 (2014), 056105 (Cited on page 47).

[150] P. A. Khomyakov, G. Giovannetti, P. C. Rusu, G. Brocks, J. van den Brink, and P. J. Kelly. "First-principles study of the interaction and charge transfer between graphene and metals". In: *Phys. Rev. B* 79 (May 2009), 195425 (Cited on page 47).

[151] G. Schusteritsch and C. J. Pickard. "Predicting interface structures: From $SrTiO_3$ to graphene". In: *Phys. Rev. B* 90 (July 2014), 035424 (Cited on page 48).

[152] G. Schusteritsch, S. P. Hepplestone, and C. J. Pickard. "First-principles structure determination of interface materials: The Ni_xInAs nickelides". In: *Phys. Rev. B* 92 (Aug. 2015), 054105 (Cited on page 48).

[153] S. Bhandary, G. Penazzi, J. Fransson, T. Frauenheim, O. Eriksson, and B. Sanyal. "Controlling Electronic Structure and Transport Properties of Zigzag Graphene Nanoribbons by Edge Functionalization with Fluorine". In: *The Journal of Physical Chemistry C* (Aug. 18, 2015) (Cited on pages 51, 57).

[154] M. A. Kuroda, J. Tersoff, D. M. Newns, and G. J. Martyna. "Conductance through Multilayer Graphene Films". In: *Nano Letters* 11 (Aug. 11, 2011), 3629–3633 (Cited on page 58).

[155] M. Fujita, K. Wakabayashi, K. Nakada, and K. Kusakabe. "Peculiar Localized State at Zigzag Graphite Edge". In: *Journal of the Physical Society of Japan* 65 (1996), 1920–1923 (Cited on pages 62, 67).

[156] Y.-W. Son, M. L. Cohen, and S. G. Louie. "Half-metallic graphene nanoribbons". In: *Nature* 444 (Nov. 16, 2006), 347 (Cited on pages 62, 67).

[157] O. V. Yazyev and M. I. Katsnelson. "Magnetic Correlations at Graphene Edges: Basis for Novel Spintronics Devices". In: *Phys. Rev. Lett.* 100 (Jan. 2008), 047209 (Cited on pages 62, 67).

[158] M. X. Chen and M. Weinert. "Half-metallic Dirac cone in zigzag graphene nanoribbons on graphene". In: *Phys. Rev. B* 94 (July 2016), 035433 (Cited on pages 62, 67).

[159] Y.-W. Son, M. L. Cohen, and S. G. Louie. "Energy Gaps in Graphene Nanoribbons". In: *Phys. Rev. Lett.* 97 (Nov. 2006), 216803 (Cited on pages 67, 74, 128).

[160] L. Yang, C.-H. Park, Y.-W. Son, M. L. Cohen, and S. G. Louie. "Quasiparticle Energies and Band Gaps in Graphene Nanoribbons". In: *Phys. Rev. Lett.* 99 (Nov. 2007), 186801 (Cited on pages 67, 128).

[161] G. Liang, N. Neophytou, D. E. Nikonov, and M. S. Lundstrom. "Performance Projections for Ballistic Graphene Nanoribbon Field-Effect Transistors". In: *IEEE Transactions on Electron Devices* 54 (Apr. 2007), 677–682 (Cited on page 67).

[162] Z. Chen, Y.-M. Lin, M. J. Rooks, and P. Avouris. "Graphene nano-ribbon electronics". In: *Physica E: Low-dimensional Systems and Nanostructures* 40 (Dec. 1, 2007), 228–232 (Cited on page 67).

[163] B. Obradovic, R. Kotlyar, F. Heinz, P. Matagne, T. Rakshit, M. D. Giles, M. A. Stettler, and D. E. Nikonov. "Analysis of graphene nanoribbons as a channel material for field-effect transistors". In: *Applied Physics Letters* 88 (Apr. 3, 2006), 142102 (Cited on page 67).

[164] J. Cai, P. Ruffieux, R. Jaafar, M. Bieri, T. Braun, S. Blankenburg, M. Muoth, A. P. Seitsonen, M. Saleh, X. Feng, K. Müllen, and R. Fasel. "Atomically precise bottom-up fabrication of graphene nanoribbons". In: *Nature* 466 (July 22, 2010), 470 (Cited on pages 67, 128).

[165] H. Zhang, H. Lin, K. Sun, L. Chen, Y. Zagranyarski, N. Aghdassi, S. Duhm, Q. Li, D. Zhong, Y. Li, K. Müllen, H. Fuchs, and L. Chi. "On-Surface Synthesis of Rylene-Type Graphene Nanoribbons". In: *Journal of the American Chemical Society* 137 (2015), 4022–4025 (Cited on pages 67, 128).

[166] L. Talirz, P. Ruffieux, and R. Fasel. "On-Surface Synthesis of Atomically Precise Graphene Nanoribbons". In: *Advanced Materials* 28 (2016), 6222–6231 (Cited on pages 67, 128).

[167] P. Ruffieux, S. Wang, B. Yang, C. Sánchez-Sánchez, J. Liu, T. Dienel, L. Talirz, P. Shinde, C. A. Pignedoli, D. Passerone, T. Dumslaff, X. Feng, K. Müllen, and R. Fasel. "On-surface synthesis of graphene nanoribbons with zigzag edge topology". In: *Nature* 531 (Mar. 23, 2016), 489 (Cited on pages 67, 128).

[168] L. Talirz, H. Söde, T. Dumslaff, S. Wang, J. R. Sanchez-Valencia, J. Liu, P. Shinde, C. A. Pignedoli, L. Liang, V. Meunier, N. C. Plumb, M. Shi, X. Feng, A. Narita, K. Müllen, R. Fasel, and P. Ruffieux. "On-Surface Synthesis

and Characterization of 9-Atom Wide Armchair Graphene Nanoribbons". In: *ACS Nano* 11 (2017), 1380–1388 (Cited on pages 67, 128).

[169] C. Moreno, M. Vilas-Varela, B. Kretz, A. Garcia-Lekue, M. V. Costache, M. Paradinas, M. Panighel, G. Ceballos, S. O. Valenzuela, D. Peña, and A. Mugarza. "Bottom-up synthesis of multifunctional nanoporous graphene". In: *Science* 360 (Apr. 13, 2018), 199 (Cited on pages 67, 68, 73, 76, 88, 128).

[170] L. Grill, M. Dyer, L. Lafferentz, M. Persson, M. V. Peters, and S. Hecht. "Nano-architectures by covalent assembly of molecular building blocks". In: *Nature Nanotechnology* 2 (Oct. 28, 2007), 687 (Cited on page 67).

[171] J. P. Perdew. "Density functional theory and the band gap problem". In: *International Journal of Quantum Chemistry* 28 (S19 1985), 497–523 (Cited on pages 71, 75).

[172] L. Hedin. "New Method for Calculating the One-Particle Green's Function with Application to the Electron-Gas Problem". In: *Phys. Rev.* 139 (Aug. 1965), A796–A823 (Cited on page 71).

[173] L. Hedin and S. Lundqvist. "Effects of Electron-Electron and Electron-Phonon Interactions on the One-Electron States of Solids". In: *Solid State Physics*. Ed. by F. Seitz, D. Turnbull, and H. Ehrenreich. Vol. 23. Academic Press, Jan. 1, 1970, 1–181 (Cited on page 71).

[174] F. Aryasetiawan and O. Gunnarsson. "The GW method". In: *Reports on Progress in Physics* 61 (1998), 237 (Cited on page 71).

[175] M. Shishkin and G. Kresse. "Implementation and performance of the frequency-dependent *GW* method within the PAW framework". In: *Phys. Rev. B* 74 (July 2006), 035101 (Cited on page 71).

[176] F. Fuchs, J. Furthmüller, F. Bechstedt, M. Shishkin, and G. Kresse. "Quasiparticle band structure based on a generalized Kohn-Sham scheme". In: *Phys. Rev. B* 76 (Sept. 2007), 115109 (Cited on page 71).

[177] M. Shishkin, M. Marsman, and G. Kresse. "Accurate Quasiparticle Spectra from Self-Consistent GW Calculations with Vertex Corrections". In: *Phys. Rev. Lett.* 99 (Dec. 2007), 246403 (Cited on page 71).

[178] M. Shishkin and G. Kresse. "Self-consistent *GW* calculations for semiconductors and insulators". In: *Phys. Rev. B* 75 (June 2007), 235102 (Cited on page 71).

[179] Y.-C. Chen, T. Cao, C. Chen, Z. Pedramrazi, D. Haberer, D. G. de Oteyza, F. R. Fischer, S. G. Louie, and M. F. Crommie. "Molecular bandgap engineering of bottom-up synthesized graphene nanoribbon heterojunctions". In: *Nature Nanotechnology* 10 (Jan. 12, 2015), 156 (Cited on page 72).

[180] S. Wang, L. Talirz, C. A. Pignedoli, X. Feng, K. Müllen, R. Fasel, and P. Ruffieux. "Giant edge state splitting at atomically precise graphene zigzag edges". In: *Nature Communications* 7 (May 16, 2016), 11507 (Cited on page 72).

[181] G. Heimel, E. Zojer, L. Romaner, J.-L. Brédas, and F. Stellacci. "Doping Molecular Wires". In: *Nano Letters* 9 (July 8, 2009), 2559–2564 (Cited on page 73).

[182] Z. Ma, F. Rissner, L. Wang, G. Heimel, Q. Li, Z. Shuai, and E. Zojer. "Electronic structure of pyridine-based SAMs on flat Au(111) surfaces: extended charge rearrangements and Fermi level pinning". In: *Phys. Chem. Chem. Phys.* 13 (2011), 9747–9760 (Cited on page 73).

[183] W. T. Sommer. "Liquid Helium as a Barrier to Electrons". In: *Phys. Rev. Lett.* 12 (Mar. 1964), 271–273 (Cited on page 78).

[184] M. W. Cole and M. H. Cohen. "Image-Potential-Induced Surface Bands in Insulators". In: *Phys. Rev. Lett.* 23 (Nov. 1969), 1238–1241 (Cited on page 78).

[185] M. W. Cole. "Properties of Image-Potential-Induced Surface States of Insulators". In: *Phys. Rev. B* 2 (Nov. 1970), 4239–4252 (Cited on page 78).

[186] M. W. Cole. "Electronic surface states of liquid helium". In: *Rev. Mod. Phys.* 46 (July 1974), 451–464 (Cited on page 78).

[187] P. M. Echenique and J. B. Pendry. "The existence and detection of Rydberg states at surfaces". In: *Journal of Physics C: Solid State Physics* 11 (1978), 2065 (Cited on page 78).

[188] P. M. Echenique. "Image-potential-induced surface states, binding energies and lifetimes". In: *Journal of Physics C: Solid State Physics* 18 (1985), L1133 (Cited on page 78).

[189] V. M. Silkin, J. Zhao, F. Guinea, E. V. Chulkov, P. M. Echenique, and H. Petek. "Image potential states in graphene". In: *Phys. Rev. B* 80 (Sept. 2009), 121408 (Cited on page 78).

[190] K. Takahashi, M. Imamura, I. Yamamoto, J. Azuma, and M. Kamada. "Image potential states in monolayer, bilayer, and trilayer epitaxial graphene studied with time- and angle-resolved two-photon photoemission spectroscopy". In: *Phys. Rev. B* 89 (Apr. 2014), 155303 (Cited on page 78).

[191] M. Feng, J. Zhao, and H. Petek. "Atomlike, hollow-core-bound molecular orbitals of C60". In: *Science* 320 (2008), 359–362 (Cited on page 78).

[192] M. Feng, J. Zhao, T. Huang, X. Zhu, and H. Petek. "The Electronic Properties of Superatom States of Hollow Molecules". In: *Accounts of Chemical Research* 44 (May 17, 2011), 360–368 (Cited on pages 78, 82, 96).

[193] S. J. Jethwa, E. L. Kolsbjerg, S. R. Vadapoo, J. L. Cramer, L. Lammich, K. V. Gothelf, B. Hammer, and T. R. Linderoth. "Supramolecular Corrals on Surfaces Resulting from Aromatic Interactions of Nonplanar Triazoles". In: *ACS Nano* (Aug. 1, 2017) (Cited on page 78).

[194] J. Hieulle, E. Carbonell-Sanromà, M. Vilas-Varela, A. Garcia-Lekue, E. Guitián, D. Peña, and J. I. Pascual. "On-Surface Route for Producing Planar Nanographenes with Azulene Moieties". In: *Nano Letters* 18 (2018), 418–423 (Cited on page 78).

[195] W. Wang and Z. Li. "Potential barrier of graphene edges". In: *Journal of Applied Physics* 109 (June 1, 2011), 114308 (Cited on page 78).

[196] J. P. Llinas, A. Fairbrother, G. Borin Barin, W. Shi, K. Lee, S. Wu, B. Yong Choi, R. Braganza, J. Lear, N. Kau, W. Choi, C. Chen, Z. Pedramrazi, T. Dumslaff, A. Narita, X. Feng, K. Müllen, F. Fischer, A. Zettl, P. Ruffieux, E. Yablonovitch, M. Crommie, R. Fasel, and J. Bokor. "Short-channel field-effect transistors with 9-atom and 13-atom wide graphene nanoribbons". In: *Nature Communications* 8 (Sept. 21, 2017), 633 (Cited on pages 90, 128).

[197] B. Kretz, D. A. Egger, and E. Zojer. "A Toolbox for Controlling the Energetics and Localization of Electronic States in Self-Assembled Organic Monolayers". In: *Advanced Science* 2 (Feb. 1, 2015), 1400016 (Cited on page 92).

[198] G. J. Kraberger, D. A. Egger, and E. Zojer. "Tuning the Electronic Structure of Graphene through Collective Electrostatic Effects". In: *Advanced Materials Interfaces* 2 (Aug. 1, 2015), 1500323 (Cited on page 92).

[199] G. Csányi, P. B. Littlewood, A. H. Nevidomskyy, C. J. Pickard, and B. D. Simons. "The role of the interlayer state in the electronic structure of superconducting graphite intercalated compounds". In: *Nature Physics* 1 (Sept. 29, 2005), 42 (Cited on page 96).

[200] Y. Xia, D. Qian, D. Hsieh, L. Wray, A. Pal, H. Lin, A. Bansil, D. Grauer, Y. S. Hor, R. J. Cava, and M. Z. Hasan. "Observation of a large-gap topological-insulator class with a single Dirac cone on the surface". In: *Nature Physics* 5 (May 10, 2009), 398 (Cited on page 101).

[201] J. E. Moore. "The birth of topological insulators". In: *Nature* 464 (Mar. 10, 2010), 194 (Cited on page 101).

[202] T. Zhang, P. Cheng, X. Chen, J.-F. Jia, X. Ma, K. He, L. Wang, H. Zhang, X. Dai, Z. Fang, X. Xie, and Q.-K. Xue. "Experimental Demonstration of Topological Surface States Protected by Time-Reversal Symmetry". In: *Phys. Rev. Lett.* 103 (Dec. 2009), 266803 (Cited on pages 101, 110).

[203] D. Hsieh, Y. Xia, D. Qian, L. Wray, J. H. Dil, F. Meier, J. Osterwalder, L. Patthey, J. G. Checkelsky, N. P. Ong, A. V. Fedorov, H. Lin, A. Bansil, D. Grauer, Y. S. Hor, R. J. Cava, and M. Z. Hasan. "A tunable topological insulator in the spin helical Dirac transport regime". In: *Nature* 460 (July 20, 2009), 1101 (Cited on page 101).

[204] K. Miyamoto, A. Kimura, T. Okuda, H. Miyahara, K. Kuroda, H. Namatame, M. Taniguchi, S. V. Eremeev, T. V. Menshchikova, E. V. Chulkov, K. A. Kokh, and O. E. Tereshchenko. "Topological Surface States with Persistent High Spin Polarization across the Dirac Point in Bi_2Te_2Se and

Bi_2Se_2Te". In: *Phys. Rev. Lett.* 109 (Oct. 2012), 166802 (Cited on pages 101, 102).

[205] A. A. Taskin, S. Sasaki, K. Segawa, and Y. Ando. "Manifestation of Topological Protection in Transport Properties of Epitaxial Bi_2Se_3 Thin Films". In: *Phys. Rev. Lett.* 109 (Aug. 2012), 066803 (Cited on page 101).

[206] P. Sessi, F. Reis, T. Bathon, K. A. Kokh, O. E. Tereshchenko, and M. Bode. "Signatures of Dirac fermion-mediated magnetic order". In: *Nat Commun* 5 (Oct. 30, 2014) (Cited on pages 101, 109, 129).

[207] Y. L. Chen, J.-H. Chu, J. G. Analytis, Z. K. Liu, K. Igarashi, H.-H. Kuo, X. L. Qi, S. K. Mo, R. G. Moore, D. H. Lu, M. Hashimoto, T. Sasagawa, S. C. Zhang, I. R. Fisher, Z. Hussain, and Z. X. Shen. "Massive Dirac Fermion on the Surface of a Magnetically Doped Topological Insulator". In: *Science* 329 (Aug. 6, 2010), 659 (Cited on pages 101, 129).

[208] L. A. Wray, S.-Y. Xu, Y. Xia, D. Hsieh, A. V. Fedorov, Y. S. Hor, R. J. Cava, A. Bansil, H. Lin, and M. Z. Hasan. "A topological insulator surface under strong Coulomb, magnetic and disorder perturbations". In: *Nature Physics* 7 (Dec. 12, 2010), 32 (Cited on pages 101, 129).

[209] A. Dankert, J. Geurs, M. V. Kamalakar, S. Charpentier, and S. P. Dash. "Room Temperature Electrical Detection of Spin Polarized Currents in Topological Insulators". In: *Nano Letters* 15 (Dec. 9, 2015), 7976–7981 (Cited on page 102).

[210] X. Wang, Y. Du, S. Dou, and C. Zhang. "Room Temperature Giant and Linear Magnetoresistance in Topological Insulator Bi_2Te_3 Nanosheets". In: *Phys. Rev. Lett.* 108 (June 2012), 266806 (Cited on page 102).

[211] K. Park, Y. Nomura, R. Arita, A. Llobet, and D. Louca. "Local strain and anharmonicity in the bonding of $Bi_2Se_{3-x}T_x$ topological insulators". In: *Phys. Rev. B* 88 (Dec. 2013), 224108 (Cited on pages 102, 104).

[212] P. E. Blöchl. "Projector augmented-wave method". In: *Phys. Rev. B* 50 (Dec. 1994), 17953–17979 (Cited on page 102).

[213] G. Kresse and D. Joubert. “From ultrasoft pseudopotentials to the projector augmented-wave method”. In: *Phys. Rev. B* 59 (Jan. 1999), 1758–1775 (Cited on page 102).

[214] D. D. Koelling and B. N. Harmon. “A technique for relativistic spin-polarised calculations”. In: *Journal of Physics C: Solid State Physics* 10 (1977), 3107 (Cited on page 102).

[215] F. Aryasetiawan, M. Imada, A. Georges, G. Kotliar, S. Biermann, and A. I. Lichtenstein. “Frequency-dependent local interactions and low-energy effective models from electronic structure calculations”. In: *Phys. Rev. B* 70 (Nov. 2004), 195104 (Cited on page 103).

[216] M. Cococcioni and S. de Gironcoli. “Linear response approach to the calculation of the effective interaction parameters in the $LDA + U$ method”. In: *Phys. Rev. B* 71 (Jan. 2005), 035105 (Cited on page 103).

[217] K.-H. Jin and S.-H. Jhi. “Effect of atomic impurities on the helical surface states of the topological insulator Bi_2Te_3”. In: *Journal of Physics: Condensed Matter* 24 (2012), 175001 (Cited on page 103).

[218] L. R. Shelford, T. Hesjedal, L. Collins-McIntyre, S. S. Dhesi, F. Maccherozzi, and G. van der Laan. “Electronic structure of Fe and Co magnetic adatoms on Bi_2Te_3 surfaces”. In: *Phys. Rev. B* 86 (Aug. 2012), 081304 (Cited on page 103).

[219] T. Eelbo, M. Waśniowska, M. Sikora, M. Dobrzański, A. Kozłowski, A. Pulkin, G. Autès, I. Miotkowski, O. V. Yazyev, and R. Wiesendanger. “Strong out-of-plane magnetic anisotropy of Fe adatoms on Bi_2Te_3”. In: *Phys. Rev. B* 89 (Mar. 2014), 104424 (Cited on page 104).

[220] N. V. Khotkevych-Sanina, Y. A. Kolesnichenko, and J. M. v. Ruitenbeek. “Fermi surface contours obtained from scanning tunneling microscope images around surface point defects”. In: *New Journal of Physics* 15 (2013), 123013 (Cited on page 109).

[221] W.-C. Lee, C. Wu, D. P. Arovas, and S.-C. Zhang. “Quasiparticle interference on the surface of the topological insulator Bi_2Te_3”. In: *Phys. Rev. B* 80 (Dec. 2009), 245439 (Cited on page 110).

[222] M. C. Martínez-Velarte, B. Kretz, M. Moro-Lagares, M. H. Aguirre, T. M. Riedemann, T. A. Lograsso, L. Morellón, M. R. Ibarra, A. Garcia-Lekue, and D. Serrate. "Chemical Disorder in Topological Insulators: A Route to Magnetism Tolerant Topological Surface States". In: *Nano Letters* 17 (July 12, 2017), 4047–4054 (Cited on page 110).

[223] J. Tersoff and D. R. Hamann. "Theory and Application for the Scanning Tunneling Microscope". In: *Phys. Rev. Lett.* 50 (June 1983), 1998–2001 (Cited on pages 119, 120).

[224] J. Tersoff and D. R. Hamann. "Theory of the scanning tunneling microscope". In: *Phys. Rev. B* 31 (Jan. 1985), 805–813 (Cited on pages 119, 120).

[225] L. Bartels, G. Meyer, and K.-H. Rieder. "Controlled vertical manipulation of single CO molecules with the scanning tunneling microscope: A route to chemical contrast". In: *Applied Physics Letters* 71 (1997), 213–215 (Cited on page 120).

[226] H. J. Lee and W. Ho. "Single-Bond Formation and Characterization with a Scanning Tunneling Microscope". In: *Science* 286 (Nov. 26, 1999), 1719 (Cited on page 120).

[227] J. Repp, G. Meyer, S. M. Stojković, A. Gourdon, and C. Joachim. "Molecules on Insulating Films: Scanning-Tunneling Microscopy Imaging of Individual Molecular Orbitals". In: *Phys. Rev. Lett.* 94 (Jan. 2005), 026803 (Cited on page 120).

[228] J. Repp, G. Meyer, S. Paavilainen, F. E. Olsson, and M. Persson. "Imaging Bond Formation Between a Gold Atom and Pentacene on an Insulating Surface". In: *Science* 312 (May 26, 2006), 1196 (Cited on page 120).

[229] L. Gross, N. Moll, F. Mohn, A. Curioni, G. Meyer, F. Hanke, and M. Persson. "High-Resolution Molecular Orbital Imaging Using a *p*-Wave STM Tip". In: *Phys. Rev. Lett.* 107 (Aug. 2011), 086101 (Cited on page 120).

[230] C. J. Chen. "Theory of scanning tunneling spectroscopy". In: *Journal of Vacuum Science & Technology A* 6 (1988), 319–322 (Cited on page 120).

[231] C. J. Chen. “Tunneling matrix elements in three-dimensional space: The derivative rule and the sum rule”. In: *Phys. Rev. B* 42 (Nov. 1990), 8841–8857 (Cited on page 120).

[232] J. Wu, S. Feng, Z. Li, K. Tao, J. Chu, J. Miao, and L. K. Norford. “Boosted sensitivity of graphene gas sensor via nanoporous thin film structures”. In: *Sensors and Actuators B: Chemical* 255 (Feb. 1, 2018), 1805–1813 (Cited on page 128).

[233] D. Krepel, J. E. Peralta, G. E. Scuseria, and O. Hod. “Graphene Nanoribbons-Based Ultrasensitive Chemical Detectors”. In: *The Journal of Physical Chemistry C* (Jan. 25, 2016) (Cited on page 128).